Quantification of Mechanisms of Human Seated Balance using System Identification

by

Kshitij Agarwal

A thesis submitted in partial fulfillment of the requirements for the degree of

Master of Science

in

Biomedical Sciences

Department of Biomedical Engineering
University of Alberta

Abstract

Elderly individuals and those affected by neuromuscular disorders are frequently not able to independently maintain seated balance. As a result, these individuals are limited in performing activities of daily living, and are susceptible to an increased risk of falling and secondary health complications. To develop therapies and targeted interventions for seated instability, it is essential, however, to first quantify the mechanisms responsible for controlling seated balance. In this context, classical system identification techniques are a promising tool for obtaining a quantitative description of such mechanisms. Motivated by these considerations, the objective of this M.Sc. research project was to quantify, using advanced system identification techniques, the active and passive control mechanisms, the muscular dynamics, and the sensorimotor time delay in seated balance control of non-disabled individuals.

14 young, non-disabled individuals were perturbed while sitting using mild, mechanical surface perturbations. The body kinematics, muscle activity, and ground reaction forces were recorded during the perturbations. Neuromusculoskeletal time series, including the body sway, the joint torque using top-down and bottom-up inverse dynamics, and the weighted electromyography representing neural activation, were calculated. Using the joint input-output system identification technique, non-parametric estimates of the active control components (neural dynamics and sensorimotor time delay) and of the active-passive control components (neural dynamics, mechanical dynamics, sensorimotor time delay, and muscular dynamics) were obtained. Parametric estimates of these components were computed using model fitting. The parameters' accuracy was evaluated using goodness-of-fit (GOF), the Akaike information criteria (AIC), and variance-accounted-for (VAF). The stability of the identified models was then assessed via a pole-

zero analysis of the characteristic equation. Finally, the identified models were implemented in simulations to assess the robustness of the model parameters.

While the thesis presents results for both the top-down and bottom-up inverse dynamics, only the top-down results are described in this abstract unless stated otherwise. For both the active and active-passive controller components, the frequency response was approximately constant for lower frequencies (< 0.4 Hz) and then steadily rose as the frequency increased. The active control component's frequency response had a phase of 30 degrees for lower frequencies and steadily rose as the frequency increased; however, it saturated around 110 degrees as the frequency reached approximately 3 Hz. The active-passive control component's frequency response had a constant phase of approximately 180 degrees for the lower frequencies (< 1Hz) that gradually increased to approximately 185 degrees at 2.5 Hz and then settled at approximately 180 degrees for higher frequencies. The across-participant variability of the non-parametric estimates of the active and active-passive control components was small. The neural dynamics were identified as a proportional-derivative (PD) controller with acceleration feedback; the sensorimotor time delay as an exponential decay function; the mechanical dynamics as a PD controller; and the muscular dynamics as a second-order transfer function. The fitting of the active control components using the stated models provided GOF, AIC, and VAF ranges of 99.2–99.8%, 1.1–1.5, and 29.0–60.8%, respectively. Similarly, the fitting of the active-passive control components using the stated models provided GOF, AIC, and VAF ranges of 99.9–99.9%, 0.4–0.5, and 97.7–99.7%, respectively. The stability analysis identified the neural dynamics, the sensorimotor time delay, and the mechanical dynamics (using bottom-up inverse dynamics) to produce a stable characteristic equation. The difference between the experimental and simulated parameters was low in most cases.

In this study, the mechanisms of seated balance have been successfully quantified for non-disabled individuals. The gained insights support the notion that closed-loop feedback control contributes to stabilizing the upper body during sitting and that a velocity-acceleration-based strategy is utilized for active control. The identified parameters can furthermore be used as a normative benchmark for quantitatively and mechanistically assessing the severity of seated imbalance in affected individuals, with the goal of optimizing rehabilitation therapies and interventions.

Preface

The research in this thesis took place at the Glenrose Rehabilitation Hospital and the University of Alberta, both in Edmonton, Alberta, Canada. The experimental procedures were executed in collaboration with another graduate student, Alireza Noamani (supervised by Drs. Hossein Rouhani and Albert Vette), who simultaneously acquired data for his thesis project on fall risk assessment. While Alireza Noamani and I performed all experiments together, we were individually responsible for our separate experimental research components. Drs. Albert Vette and Hossein Rouhani were involved in formulating the research question for this thesis project. The experimental protocol (*see Chapter 4*) was developed by me, with the guidance of Drs. Albert Vette and Hossein Rouhani and the assistance of Andrew Williams. The customized stool for placing the force plate and for facilitating seated posture of the study participants (*see Chapter 4*) was designed and constructed by Quinn Boser and Andrew Williams. The literature reviews in Chapters 2 and 3, the data analysis in Chapter 4, the results reported in Chapter 5, and the interpretation of the findings in Chapter 6 are my original work. This research project received research ethics approval from the Health Research Ethics Board of the University of Alberta, under the project title "Assessment of Dynamic Balance and Fall Risk in Sitting", No. Pro00063998 (approved July 4, 2016).

पायल सेन अग्रवाल के नाम

Dedicated to Payel Sen Agarwal

পায়েল সেন আগারওয়াল কে নিবেদিত

Acknowledgments

My sincere gratitude to my supervisor, mentor, and friend, Dr. Albert H. Vette. He had constantly supported and motivated me throughout the tenure of the Master's program. He had helped me in the shaping of my research and constantly guided me whenever I got stuck. This research would not have been possible without his hard work and dedication towards me. I would also like to express my gratitude to my co-supervisor, Dr. Hossein Rouhani. He had always worked with me in developing this research. His constant moral boost had always kept me motivated during the tenure. I was also a fan of his creativity, which at several points in time had helped this research.

I would like to thank my lab mates and staff for their enormous effort to make this research happen. I would like to thank Andrew Williams for setting up the base for me. He had significantly contributed towards establishing the idea of the research, testing the preliminary methods of the research and providing a nice summary. Many thanks to Alireza Noamani for helping me in conducting the experiments of this research and answering all the questions I had. My sincere thanks to Aiden Kooyman for wonderfully reviewing my thesis and helping me complete on time. I am extremely grateful to Azhali Arellano López, Steven Phan, Adeolu Adeoye, Sofia Medina Pando, Jordan Arthur, and Zainab Azhar for helping me with the conduction of the experiments and data analysis. I would like to thank Jacques Bobet for helping me with learning new software that was an essential part of this research. I would like to acknowledge the support from Darrell Goertzen for assisting us in the conduction of the experiment at the Computer-Assisted Rehabilitation Environment. I could always count on Hossein Bahari, Milad Nazarahari, McNiel Keri, Aïda Valevicius, and Jeremy Hall for any assistance required.

I would like to thank my family and friends for providing me with constant moral support to accomplish this research. At last, I want to thank Payel Sen Agarwal for bringing immense happiness in my life. It was due to her support, encouragement and love that I was able to successfully complete this research.

This project was made possible through generous support from the Faculty of Graduate Studies and Research, University of Alberta; the Faculty of Engineering, University of Alberta; the

Table of Contents

List of Tables

List of Figures

Nomenclature

2D	Two-dimensional
3D	Three-dimensional
ADL	Activities of daily living
AIC	Akaike information criteria
A-P	Anterior-posterior
BF	Biceps femoris
COM	Center of mass
COP	Center of pressure
CNS	Central nervous system
CMRR	Common-mode rejection ratio
CAREN	Computer-assisted rehabilitation environment
EMG	Electromyography
ES	Erector spinae
ESL3	Erector spinae at third lumbar vertebra
EO	External obliques
FRF	Frequency response functions
FES	Functional electrical stimulation
GOF	Goodness-of-fit
HAT	Head-arms-and-trunk
IMUs	Inertial measurement units
LGTR	Left greater trochanter
LBFP	Left-backward force plate
LFFP	Left-forward force plate
LFHD	Left-forward head
MVC	Maximal voluntary contractions
M-L	Medio-lateral
PD	Proportional-derivative
PID	Proportional-integrative-derivative

RA	Rectus abdominis
RF	Rectus femoris
RGTR	Right greater trochanter
RBFP	Right-backward force plate
RFFP	Right-forward force plate
RFHD	Right-forward head
RMS	Root-mean-square
SCI	Spinal cord injury
SD	Standard deviation
sub-MVC	sub-Maximal voluntary contractions
VAF	Variance accounted for
XIP	Xiphoid

1 Introduction

1.1 Motivation

Seated balance is necessary for humans to maintain an upright position during many functional tasks. It is also essential for stabilizing the body against unpredictable internal and external disturbances [2]–[5]. The upper body, however, is inherently unstable [6], [7], such that any disturbance can lead the upper body to tip over. As a consequence, the body's neuromusculoskeletal system and in particular the central nervous system (CNS), sensory systems, muscles, and passive tissue properties, such as stiffness and damping, work together in an integrated fashion, with the goal of maintaining seated balance [8]. However, due to aging as well as stroke, spinal cord injury (SCI), and other neurological or musculoskeletal disorders (Figure 1-1), these systems can deteriorate [1], [9]–[11]. In particular, affected individuals experience loss of muscle control, insufficient muscle strength, and degraded sensory information, which can lead to an increase in the risk of falling [12], reduced functional independence [13], and secondary health complications such as kyphosis, pressure sores, or respiratory dysfunction [14], [15]. To develop therapies and targeted interventions for seated instability, it is essential, however, to first quantify the control mechanisms of seated balance [16]–[19]. Such knowledge is essential to define a baseline of seated balance; a baseline that can serve as a benchmark for quantitatively and mechanistically assessing the severity of seated imbalance in affected individuals, with the goal of identifying and prescribing optimal therapies and targeted interventions.

1.2 Mechanisms of Seated Balance

Seated balance is a complex task that requires the contributions from the CNS, sensory systems, muscles, and passive tissue properties such as stiffness and damping. Stiffness and damping due to muscles, ligaments, and surrounding tissue produce corrective joint torques (*passive control*) without the time delay that contribute to upper body stabilization (*Human body dynamics*) [20]. However, joint torques produced via such passive control are not sufficient to stabilize the upper body [17]. In addition, the human body senses the seated imbalance and generates additional joint torques via feedback control (*active control*) to complement the passive control and stabilize the

1

body. This active control component involves several steps: First, the body orientation in space is perceived by the sensory systems (*sensory dynamics*), such as the vestibular, proprioceptive, and visual systems [21]. The acquired information is then passed on to the brain, which converts the sensory information into a motor command (*neural dynamics*). Finally, this motor command activates relevant muscles (*muscular dynamics*) and generates the active joint torques contributing to body stabilization [22]. Note that the process of transferring information from the sensory systems to the brain, of integrating the sensory information, and of sending the motor command to the muscular system involves various time delays (overall summarized as *sensorimotor time delay*) [20]–[22].

In contrast to the described feedback control, also feed-forward control is active, where the brain attempts to anticipate the intended body displacement and issues the required motor commands for muscle activation [23], [24]. Feed-forward control relies on past-experience and complements feedback control to provide stability. However, feedforward control is not sufficient to provide stability during unpredictable external disturbances [25].
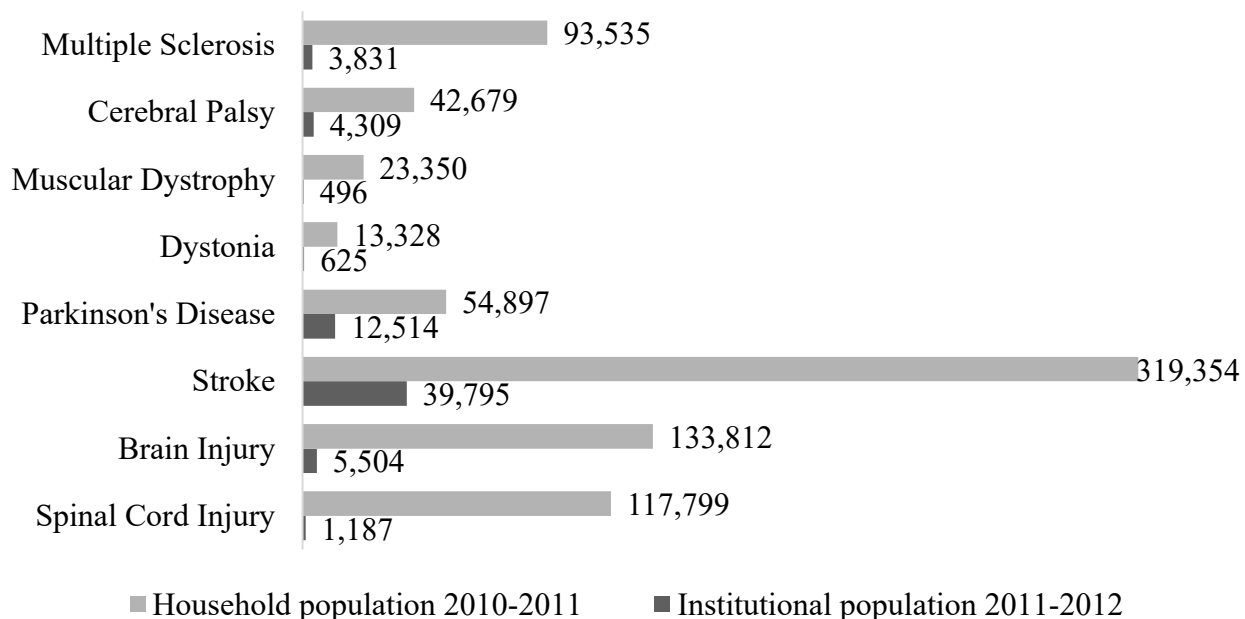
Figure 1-1: Prevalence of neuromuscular disorders in Canada that may impair seated balance (Statistics Canada. Table 13-10-0468-01 Neurological conditions in institution, and Table 13-10-0467-01 Neurological conditions in household population).

Two methods exist to identify the above-mentioned feedback mechanisms of seated balance: (1) descriptive measures, where the motion of the body's segments, the ground reaction forces, and/or muscle activity in quasi-static or voluntary movement conditions (also known as posturographic measures) are reduced to single-number measures to quantify balance proficiency [26]–[29]; and (2) classical *system identification*, where the body's response (movement of the body segments, ground reaction forces, and/or muscle activity) to an unpredictable external (physical or sensory) disturbance is used to quantify balance [20]. It has been shown that, between these two techniques, system identification provides the most accurate estimation of balance control as posturographic measures include both the dynamics associated with balance control and with the external process disturbing balance [20]. In the context of seated balance, the human upper body and its control can be represented by a closed-loop control model, with the upper body dynamics serving as the plant, the brain serving as the active controller, and the output of the sensory systems being used as feedback [16], [17]. Closed-loop control models are identified through closed-loop system identification techniques, including the *Direct Approach*, the *Indirect Approach*, and the *Joint Input-Output Approach* [20], [30].

Among the three approaches, the Direct Approach provides an erroneous identification of the closed-loop control model because it considers the closed-loop system as an open-loop system, where the output of the plant/controller is considered independent of the input; however, those two entities are clearly not independent [20], [31], [32]. The Indirect Approach calculates the sensitivities of the input/output of the plant/controller with respect to the applied external disturbance. Since this sensitivity includes both the plant and controller dynamics, the dynamics of one are needed to identify the other [31]. This is a significant limitation of the Indirect Approach for identifying human balance: to identify the neural dynamics; we require the knowledge of the human body dynamics, which are often approximated by a mathematical model that may significantly differ from the actual characteristics of the upper body. This difference is then often reflected in the identified controller, making its identification unreliable [20]. The Joint Input-Output Approach compares the sensitivity of the output of the plant and the applied external physical disturbance with the sensitivity of the input of the plant and the applied external physical disturbance to quantify the controller. Similarly, the sensitivity ratios of the controller input/output and the applied external sensory disturbance provide estimates of the plant [31]. On the contrary,

the Joint Input-Output Approach does not require prior knowledge of other components, providing more accurate estimations of each component of the closed-loop control system [20].

Several studies have applied closed-loop system identification techniques to assess the mechanisms of human balance. For standing balance in non-disabled individuals, researchers have attempted to quantify the human body dynamics [1], [8], [33], [34], passive and active control mechanisms [8], [22], the sensory dynamics [21], [35]–[37], muscular dynamics [8], [22], and the sensorimotor time delay [8], [22] through the Direct [38], Indirect [8], [21], [39]–[41] and Joint Input-Output Approaches [22], [34], [42]. For the upper body during seated balance, researchers have attempted to identify the passive and active control mechanisms [17] and the sensory dynamics [36] through the indirect approach in non-disabled individuals. However, these studies have not considered the muscular dynamics as part of the active control component; thus, the parameters for the neural dynamics are not an accurate representation of the neuromuscular control scheme in seated balance [8]. Moreover, these studies have applied the indirect approach that requires prior knowledge of at least one component; in this case, the human body dynamics were presumably known, which causes erroneous estimations of other components. Thus, to more accurately identify respective control components in seated balance, it is required to implement the Joint Input-Output Approach while also including the muscular dynamics in the closed-loop control model of human seated balance. As mentioned earlier, the obtained parameters and insights can ultimately be used as a benchmark for assessing balance proficiency and underlying mechanisms in clinical populations, with the goal of developing and prescribing targeted interventions.

1.3 Thesis Objectives

Based on the considerations above, the purpose of the proposed project is to quantify, using the Joint Input-Output Approach, the active (neural) control mechanisms, the passive (mechanical) control mechanisms, the muscular dynamics, and the sensorimotor time delay in seated balance control of non-disabled individuals.

1.4   Thesis Outline

This thesis will consist of the following additional chapters: Chapter 2 focuses on the theory of system identification techniques and its application to the identification of mechanisms of human balance control. Chapter 3 provides a review of the existing literature on seated balance, human body dynamics, the passive (mechanical dynamics) and active (neural dynamics) control, the sensory dynamics, the muscular dynamics, and the sensorimotor time delay during standing and sitting. Chapter 3 will also review features and the current state of using and processing electromyography, motion capture system, and force plate data in the neuromuscular control and biomechanics studies. The feedback control models of human balance in standing and sitting were also discussed in Chapter 3. Chapter 4 discusses the methods of the performed work, with a focus on the experimental setup and equipment used, participants studied, the protocol employed, and signal processing techniques and analyses applied. Chapter 5 presents the experimental results, with the overall goal of identifying the parameters of seated balance control. Chapter 6 provides a discussion of the obtained results and the limitations of the performed study. Chapter 7 offers a summary of the work and concludes the findings with recommendations for future work.

2 System Identification

2.1   Overview

This chapter describes the theory of system identification in the field of control systems and its application to quantitatively characterize, or identify, a closed-loop system. A particular focus of this chapter is on the different existing approaches for identifying a closed-loop system.

2.2   System Identification Theory

To derive a mathematical model from experimental data is a prevalent process in science and engineering. In the field of control systems, this process is called system identification, and its primary objective is to obtain dynamic models (differential or difference equations) of a system based on the observed data. These systems are natural or human-made, e.g., animals, plants, vehicles, or food processors. The system can be classified as open-loop or closed-loop systems. In open-loop systems, the output of the system does not affect the system behavior, whereas in the closed-loop system the output of the system affects the system behavior by feeding back the output to the system. Furthermore, systems can also be classified based on the number of inputs and outputs that it has. There is single input single output, single input multiple output, multiple input single output, and multiple input multiple output systems, depending on the number of independent inputs and outputs the system has. For this section, we will only focus on open-loop and closed-loop single input single output systems. However, the same techniques apply to systems that have multiple inputs, multiple outputs, or both.

System identification involves experimental design, data collection, selection of model set, fitting criteria, model estimation, and model validation based on some or no prior knowledge of the system in consideration (Figure 2-1).

The most critical requirement of system identification is the experimental design that involves the collection of meaningful data that can correctly describe the properties of the system based on some or no previous knowledge of the system. The experimental design involves the choice of an excitation signal that can excite the relevant characteristics of the system, which is reflected in the

system's output. The excitation signal should have the following characteristics to identify a system:

➢ The following limit should exist:

$$\gamma_u(\tau) = \lim_{N \to \infty} \frac{1}{N} \sum_{t=1}^{N} U_{t+\tau} U_t^T, \qquad\qquad \text{Eq. (1)}$$

where U is the excitation signal, γ_u is the autocorrelation function, τ is the time delay, t is the time, and T marks the matrix transpose.

➢ The matrix $R_u(n)$ should be positive definite for a particular value of n, where a matrix is positive definite if it is a symmetric matrix and has positive eigenvalues [43].

$$R_u(n) = \begin{bmatrix} \gamma_u(0) & \cdots & \gamma_u(n-1) \\ \vdots & \ddots & \vdots \\ \gamma_u(1-n) & \cdots & \gamma_u(0) \end{bmatrix} \qquad\qquad \text{Eq. (2)}$$
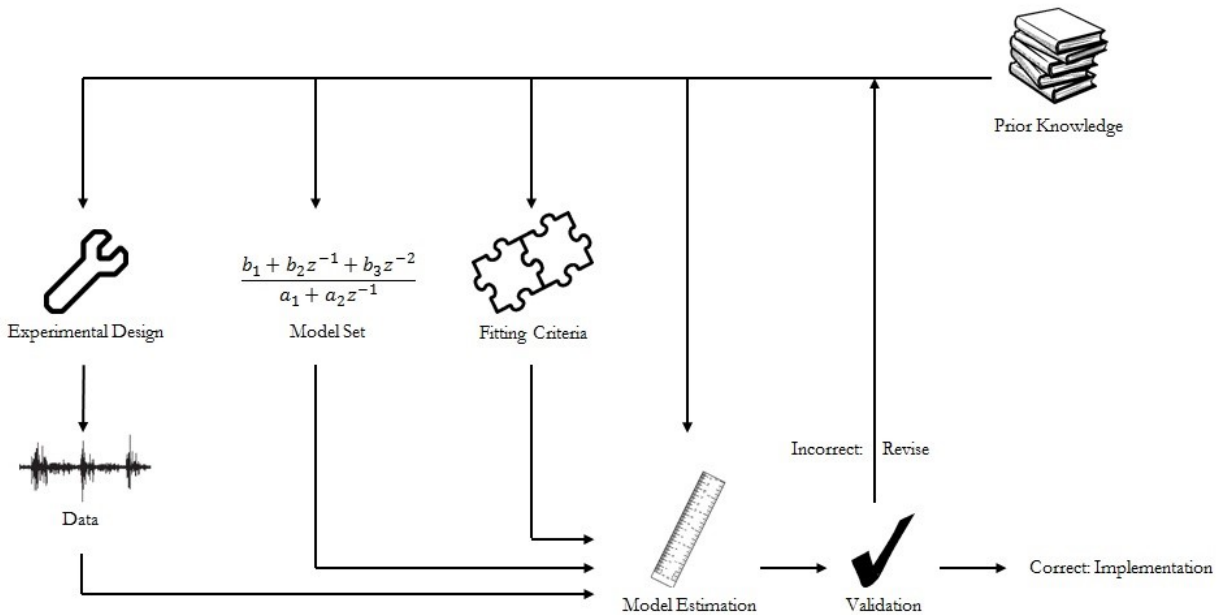
Figure 2-1: System identification loop, adapted from [44]. A typical system identification process requires some prior knowledge of the system. Based on that knowledge, the experimental design, model set, and fitting criteria are selected. After experimental data collection, models are estimated for that data set, and a validation study is performed. If the model passes the validation test, it is implemented for further use; otherwise, some or all of the above steps are repeated.

Signals that obey the above two rules are called persistent excitation signals. There are many types of persistent excitation signals; for example, an impulse, a step, a sinusoid, filtered white noise, multi-sinusoidal signals, and random binary sequences. The choice for the excitation signal is based on the order of the system into consideration. For example, if a system is an nth order linear system, the order of the persistent excitation signal should be at least $2 \times n$ to accurately identify it via system identification. The order of the signal is calculated as k if $R_u(n)$ is positive definite for n = k and not positive definite for n = k + 1. Thus, the order of an impulse response is 0, of a step response 1, and of white noise infinite. In general, the more complex and random an input signal is, the higher the order of that signal. While, white noise consequently is the ideal signal to identify any system, no physical system exists that can utilize white noise as an excitation signal. Therefore, researchers implement other signals, such as, multi-sinusoidal signals or filtered white noise that have the properties of white noise and can be utilized in combination with physical systems.

The next step in system identification is to collect experimental data of the excitation signal and the response signal. Several factors need to be considered during experimental data collection; for example, analog-to-digital conversion, sampling frequency, sampling bandwidth, analog filtering, full-scale range of the analog input, quantization error, dynamic range, bit rate and signal-to-noise ratio. These factors are selected based on the properties of the system being identified as informed by previous knowledge or preliminary testing.

Following data collection, a suitable model set for the system is selected. Several different model sets had developed and applied to previous studies. The choice of a model depends upon the model structure including black-box structures, physical modelling structures and semi-physical modelling structures. Black-box structures rely only on the data and no physical knowledge of the system. Black-box structures can be parametric- for example, Auto-Regressive with Exogenous input, Auto-Regressive Moving-Average with Exogenous input, Output-Error, Box-Jenkins and state-space; or non-parametric- for example, impulse response functions, step response functions, and frequency response functions (FRF). For physical modelling structures, we take advantage of the physical properties of the system and describe the system using physical laws and equations. However, both the black-box and physical modelling structures are too extreme for system identification as one ignores the physical properties of the system while the other is sometimes become too complicated or unrealistic to implement. Most commonly, people have implemented

semi-physical modelling structures, where they still consider the system to be a black box; however, the model equations and expressions are inspired by the physical properties of the system.

Non-probabilistic and probabilistic are the two criteria used for estimating the model's parameters. When using a non-probabilistic criterion, the "allowed" disturbance in the output of the model is constrained by a constant. When using a probabilistic criterion, the disturbance is defined as a random process with a known probability distribution function. Then, the best estimates of the model are identified using the prediction error method. Both probabilistic and non-probabilistic criteria sometimes identify more than one model of the system. Usually, the best model is selected based on the parsimony principle and Akaike's information criteria, which ensure a less complex model structure and better goodness-of-fit [44].

The model validation is performed by a cross-validation test, where the model output is compared to a new set of experimental output data, and the error between the model output and the new experimental data set is calculated. This error is used to calculate the goodness-of-fit of the model, which can be between 0 and 100%, with 0% corresponding to no fit and 100% corresponding to a perfect fit. If the model fails the validation test, some, or all, of the above steps need to be reiterated [45]–[47].

2.3 Closed-Loop System

Human balance control is often considered as a feedback system such that, in system identification approaches, it is treated as a closed-loop system. A closed-loop system consists of a plant (P), a controller (C) and a feedback branch (F) (Figure 2-2). The plant captures the process and actuator of the dynamic system. Any input (u) to the plant will cause physical changes in the system. Typical examples of a plant are motors, engines, the human musculoskeletal system, and the transformation of raw material (e.g., silicon into high-tech devices such as cell phones). A given dynamic system is monitored by a controller that alters its operating conditions. The controller compares the set point, known as a reference (r) to the output (y) of the plant to adjust the plant input, such that, ideally, the plant output matches the reference value. Typical examples of the controller are microcontrollers, remote controls, joysticks, or the human brain. The feedback

branch is used to monitor the output of the plant and send it back to the controller for further processing (e.g., error calculation between r and y – see below). The feedback can have linear, non-linear, time-varying and time-invariant structures. There are two major types of feedback: negative feedback and positive feedback. Negative feedback is used to reduce an error between the output of the plant and desired set point, whereas positive feedback increases the error. Negative feedback has been implemented in cruise control of vehicles where a set speed is maintained. Positive feedback is used to amplify the output; for example, the human population growth model describes population growth depending on the current population which keeps on increasing[20], [45], [47].
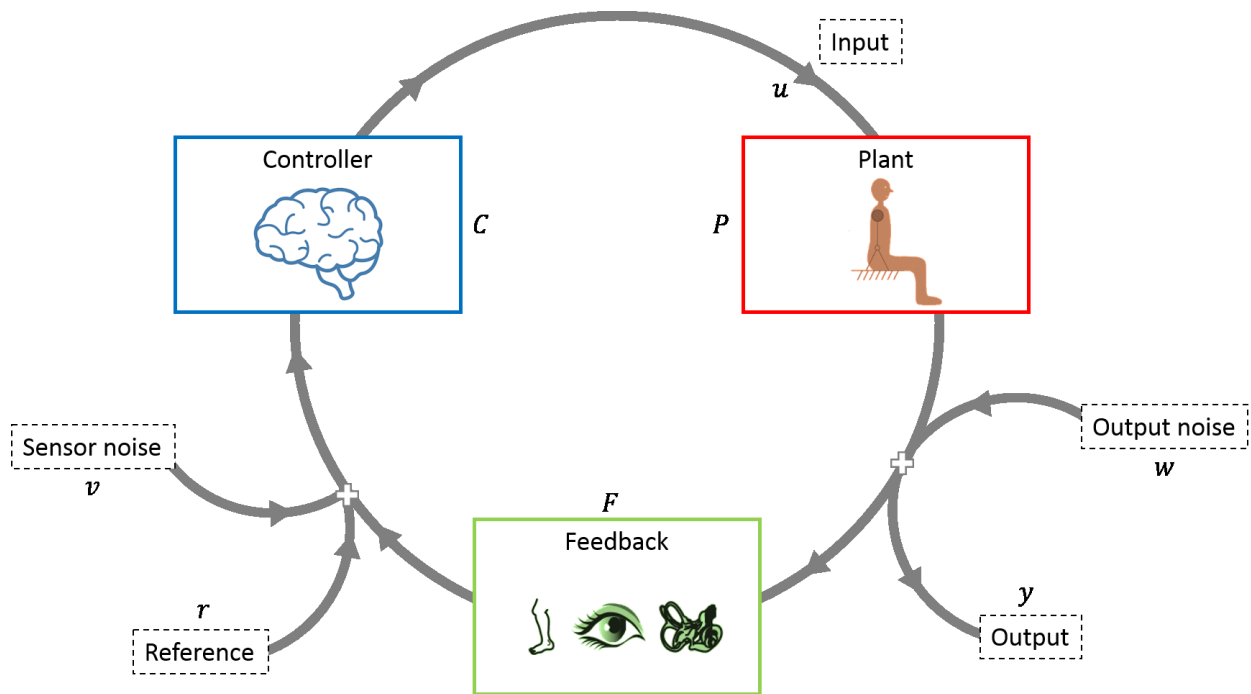
Figure 2-2: Block diagram of a closed-loop system, where the plant (P) receives the input (u), including the unpredictable sensor noise (v) and produces output (y). The feedback (F) measures this output, along with the unpredictable output noise (w) The feedback information is then compared with a reference (r) and sent to the controller (C). The controller then produces an adequate input to the plant to ideally match the plant output with the reference [20].

Several noise sources can affect the stability of the system and are often unpredictable. Noise can affect the stability of the plant, corrupt feedback information, and produce an undesirable controller output. In closed-loop system diagrams, noise sources are represented by adding a noise input to the output of the plant, labelled as output noise (w), or to the input of the controller, labelled as sensor noise (v) (Figure 2-2) [20], [45], [47].

A considerable literature has been developed to identify a closed-loop system using system identification [45], [47]. Three primary methods exist to identify the components of a closed-loop system using system identification: The Direct Approach, the Indirect Approach and the Joint Input-Output Approach [20]. In these approaches, FRF (Equation (3)) are computed, describing the characteristics of various components in the closed-loop system, where $\emptyset_{gf}(\omega)$ corresponds to a cross-spectral density between two generic functions $g(\omega)$ and $f(\omega)$, and $\emptyset_{gg}(\omega)$ corresponds to the power spectral density of the function $g(\omega)$.

$$FRF_{gf}(\omega) = \frac{\emptyset_{gf}(\omega)}{\emptyset_{gg}(\omega)} \qquad \text{Eq. (3)}$$

To evaluate the FRF using each method consider the closed-loop system in Figure 2-2 and the following series of equations. The input and output can be written as the following equations:

$$y(\omega) = P(\omega) \cdot u(\omega) + w(\omega) \qquad \text{Eq. (4)}$$

$$u(\omega) = C(\omega) \cdot [r(\omega) - F(\omega) \cdot y(\omega) + v(\omega)] \qquad \text{Eq. (5)}$$

Thus, substituting $u(\omega)$ from Equation (5) into Equation (4) would yield Equation (6), where I is the identity matrix of an appropriate order. Equation (7) is obtained by substituting y(ω) from Equation (6) into Equation (5).

$$y(\omega) = \frac{P(\omega) \cdot C(\omega)}{I + P(\omega) \cdot C(\omega) \cdot F(\omega)} \cdot r(\omega) + \frac{P(\omega) \cdot C(\omega)}{I + P(\omega) \cdot C(\omega) \cdot F(\omega)} \cdot v(\omega) + \frac{I}{I + P(\omega) \cdot C(\omega) \cdot F(\omega)} \cdot w(\omega) \quad \text{Eq. (6)}$$

$$u(\omega) = \frac{C(\omega)}{I + P(\omega) \cdot C(\omega) \cdot F(\omega)} \cdot r(\omega) - \frac{C(\omega) \cdot F(\omega)}{I + P(\omega) \cdot C(\omega) \cdot F(\omega)} \cdot w(\omega) + \frac{C(\omega)}{I + P(\omega) \cdot C(\omega) \cdot F(\omega)} \cdot v(\omega) \quad \text{Eq. (7)}$$

To simplify the analysis, let's take: $F(\omega) = I$, and $r(\omega) = 0$. A similar analysis can be performed for a non-zero reference and other feedback structures. We will also define $S(\omega) = \frac{I}{I + P(\omega) \cdot C(\omega)}$ as output sensitivity, $M(\omega) = C(\omega) \cdot S(\omega)$ as input sensitivity, and $Q(\omega) = P(\omega) \cdot M(\omega)$ as

complimentary sensitivity as described in [20]. Making these changes in the above equations will lead to the following equations:

$$y(\omega) = S(\omega) \cdot w(\omega) + Q(\omega) \cdot v(\omega) \qquad \text{Eq. (8)}$$

$$u(\omega) = -M(\omega) \cdot w(\omega) + M(\omega) \cdot v(\omega) \qquad \text{Eq. (9)}$$

To apply the different system identification approaches, we have to calculate the power spectral density of the input ($\emptyset_{uu}(\omega)$) and the output ($\emptyset_{yy}(\omega)$), and the cross-spectral density between the output noise and the input ($\emptyset_{wu}(\omega)$), the sensor noise and the input ($\emptyset_{vu}(\omega)$), the input and the output ($\emptyset_{uy}(\omega)$), the output noise and the output ($\emptyset_{wy}(\omega)$), and the sensor noise and the output ($\emptyset_{vy}(\omega)$). The power spectral density ($\emptyset_{gg}(\omega)$) and cross-spectral density ($\emptyset_{gf}(\omega)$) are defined as follow, where $g(\omega)$ and $f(\omega)$ are two different functions and E is the expected value:

$$\emptyset_{gg}(\omega) = E\{g(-\omega), g(\omega)^T\} \qquad \text{Eq. (10)}$$

$$\emptyset_{gf}(\omega) = E\{g(-\omega), f(\omega)^T\} \qquad \text{Eq. (11)}$$

Thus, the power spectral density of the input can be calculated via the following equation.

$$\emptyset_{uu}(\omega) = E\{[-M(-\omega) \cdot w(-\omega) + M(-\omega) \cdot v(-\omega)], [-w^T(\omega) \cdot M^T(\omega) + v^T(\omega) \cdot M^T(\omega)]\}$$
$$\text{Eq. (12)}$$

Since sensor noise and output noise are independent, all the cross terms ($\emptyset_{vw}(\omega)$ and $\emptyset_{wv}(\omega)$) are zero in the above equation, yielding a more compact form of the above equation, where $\emptyset_{ww}(\omega)$ and $\emptyset_{vv}(\omega)$ are the power spectral density of the output noise and the sensor noise, respectively:

$$\emptyset_{uu}(\omega) = M(-\omega) \cdot \emptyset_{ww}(\omega) \cdot M^T(\omega) + M(-\omega) \cdot \emptyset_{vv}(\omega) \cdot M^T(\omega) \quad \text{Eq. (13)}$$

Similarly, we can write the power spectral density of the output using the following equation:

$$\emptyset_{yy}(\omega) = S(-\omega) \cdot \emptyset_{ww}(\omega) \cdot S^T(\omega) + Q(-\omega) \cdot \emptyset_{vv}(\omega) \cdot Q^T(\omega) \quad \text{Eq. (14)}$$

In addition, all the cross-spectral densities between input, output, sensor noise and output noise can be written via the following equations:

$$\emptyset_{wu}(\omega) = -\emptyset_{ww}(\omega) \cdot M^T(\omega) \qquad \text{Eq. (15)}$$

$$\emptyset_{vu}(\omega) = \emptyset_{vv}(\omega) \cdot M^T(\omega) \qquad \text{Eq. (16)}$$

$$\emptyset_{wy}(\omega) = \emptyset_{ww}(\omega) \cdot S^T(\omega) \qquad \text{Eq. (17)}$$

$$\emptyset_{vy}(\omega) = \emptyset_{vv}(\omega) \cdot Q^T(\omega) \qquad \text{Eq. (18)}$$

$$\emptyset_{uy}(\omega) = -M(-\omega) \cdot \emptyset_{ww}(\omega) \cdot S^T(\omega) + M(-\omega) \cdot \emptyset_{vv}(\omega) \cdot Q^T(\omega) \qquad \text{Eq. (19)}$$

Utilizing the analysis based on the derived equations, we can now determine the FRFs for all three system identification approaches.

2.3.1 Direct Approach

In the Direct Approach, the FRF is estimated between the input and output of the system, yielding the following FRF:

$$FRF_{uy}(\omega) = \frac{\emptyset_{uy}(\omega)}{\emptyset_{uu}(\omega)} \qquad \text{Eq. (20)}$$

Substituting Equation (13) and Equation (19) in the above equation, we obtain the following equation:

$$FRF_{uy}(\omega) = \frac{-M(-\omega) \cdot \emptyset_{ww}(\omega) \cdot S^T(\omega) + M(-\omega) \cdot \emptyset_{vv}(\omega) \cdot Q^T(\omega)}{M(-\omega) \cdot \emptyset_{ww}(\omega) \cdot M^T(\omega) + M(-\omega) \cdot \emptyset_{vv}(\omega) \cdot M^T(\omega)} \qquad \text{Eq. (21)}$$

As we see from the above equation, $M(-\omega)$ is common in all the terms; therefore, multiplying the numerator and denominator by the inverse of $M(-\omega)$ will provide the following equation:

$$FRF_{uy}(\omega) = \frac{\emptyset_{ww}(\omega) \cdot S^T(\omega) + \emptyset_{vv}(\omega) \cdot Q^T(\omega)}{\emptyset_{ww}(\omega) \cdot M^T(\omega) + \emptyset_{vv}(\omega) \cdot M^T(\omega)} \qquad \text{Eq. (22)}$$

Substituting back $M(\omega) = C(\omega) \cdot S(\omega)$ and $Q(\omega) = P(\omega) \cdot C(\omega) \cdot S(\omega)$, we obtain the following FRF function:

$$FRF_{uy}(\omega) = \frac{-\emptyset_{ww}(\omega) \cdot S^T(\omega) + \emptyset_{vv}(\omega) \cdot S^T(\omega) \cdot C^T(\omega) \cdot P^T(\omega)}{\emptyset_{ww}(\omega) \cdot S^T(\omega) \cdot C^T(\omega) + \emptyset_{vv}(\omega) \cdot S^T(\omega) \cdot C^T(\omega)} \qquad \text{Eq. (23)}$$

Separating the two terms in the numerator of the above equation will yield the following equation:

$$FRF_{uy}(\omega) = \frac{-\emptyset_{ww}(\omega) \cdot S^T(\omega)}{\emptyset_{ww}(\omega) \cdot S^T(\omega) \cdot C^T(\omega) + \emptyset_{vv}(\omega) \cdot S^T(\omega) \cdot C^T(\omega)} + \frac{\emptyset_{vv}(\omega) \cdot S^T(\omega) \cdot C^T(\omega) \cdot P^T(\omega)}{\emptyset_{ww}(\omega) \cdot S^T(\omega) \cdot C^T(\omega) + \emptyset_{vv}(\omega) \cdot S^T(\omega) \cdot C^T(\omega)}$$

$$\text{Eq. (24)}$$

13

Now, we can multiply the numerator and denominator of the first term with $C^T(\omega)$ and extract $P^T(\omega)$ from the second term. This will yield the following FRF:

$$FRF_{uy}(\omega) = \left(\frac{\emptyset_{ww}(\omega)}{\emptyset_{ww}(\omega)+\emptyset_{vv}(\omega)}\right)\frac{-1}{C^T(\omega)} + \left(\frac{\emptyset_{vv}(\omega)}{\emptyset_{ww}(\omega)+\emptyset_{vv}(\omega)}\right)\frac{P^T(\omega)}{1} \qquad \text{Eq. (25)}$$

From the above equation, it can be seen that the Direct Approach in closed-loop system will lead to the identification of the plant and of the inverse of the controller. It can also be seen that this identification will depend on the power spectral densities of the output noise and the sensor noise, which, in this case, are unknown. Thus, it is challenging to identify the components of closed-loop system via the Direct Approach [20].

2.3.2 Indirect approach

In the *Indirect Approach*, the FRF is estimated between the sensor noise or output noise and the input or the output. To the intrinsic sensor noise or output noise of the system, we add a known noise. The known noise has to have a higher power as compared to intrinsic sensor noise or output noise, which leads to the domination of the known noise on the intrinsic sensor noise or output noise. Therefore, the known noise signal is treated as the sensor noise or output noise of the system. The following equation has the FRF between the output noise and the input:

$$FRF_{wu}(\omega) = \frac{\emptyset_{wu}(\omega)}{\emptyset_{ww}(\omega)} \qquad \text{Eq. (26)}$$

Substituting Equation (15) in the above equation will yield the following equation:

$$FRF_{wu}(\omega) = \frac{-\emptyset_{ww}(\omega) \cdot M^T(\omega)}{\emptyset_{ww}(\omega)} \qquad \text{Eq. (27)}$$

As $\emptyset_{ww}(\omega)$ appears in both numerator and denominator, we can remove the term:

$$FRF_{wu}(\omega) = -M^T(\omega) \qquad \text{Eq. (28)}$$

Similarly, other FRF can be computed as described below:

$$FRF_{vu}(\omega) = M^T(\omega) \qquad \text{Eq. (29)}$$

$$FRF_{wy}(\omega) = S^T(\omega) \qquad \text{Eq. (30)}$$

$$FRF_{vy}(\omega) = Q^T(\omega) \qquad \text{Eq. (31)}$$

14

By substituting back $M(\omega) = \frac{C(\omega)}{I + P(\omega) \cdot C(\omega)}$, $Q(\omega) = \frac{P(\omega) \cdot C(\omega)}{I + P(\omega) \cdot C(\omega)}$, and $S(\omega) = \frac{I}{I + P(\omega) \cdot C(\omega)}$ in the above equations, we will obtain the following FRFs:

$$FRF_{wu}(\omega) = -\left(\frac{C(\omega)}{I + P(\omega) \cdot C(\omega)}\right)^T \qquad \text{Eq. (32)}$$

$$FRF_{vu}(\omega) = \left(\frac{C(\omega)}{I + P(\omega) \cdot C(\omega)}\right)^T \qquad \text{Eq. (33)}$$

$$FRF_{wy}(\omega) = \left(\frac{I}{I + P(\omega) \cdot C(\omega)}\right)^T \qquad \text{Eq. (34)}$$

$$FRF_{vy}(\omega) = \left(\frac{P(\omega) \cdot C(\omega)}{I + P(\omega) \cdot C(\omega)}\right)^T \qquad \text{Eq. (35)}$$

The FRF calculated above provide the estimates of both the controller and the plant. Since these FRF do not contain terms for the sensor and output noise, the Indirect Approach provides consistent estimates of both the plant and the controller. For this technique, however, it is required to have a model of the plant to obtain an estimate of the controller or a model of the controller to obtain an estimate of the plant [20].

2.3.3 Joint input-output approach

In the Joint Input-Output Approach, the FRF are estimated from the ratios of the cross-spectral density between the sensor or output noise and the input, and the cross-spectral density between the sensor or output noise and the output. Similarly to Indirect Approach, we add known noise that dominates the intrinsic sensor noise or output noise. Thus, the known noise signal is considered as the sensor noise or output noise of the system. The two FRFs can be written as follows:

$$FRF_C(\omega) = \frac{\emptyset_{wu}(\omega)}{\emptyset_{wy}(\omega)} \qquad \text{Eq. (36)}$$

$$FRF_P(\omega) = \frac{\emptyset_{vy}(\omega)}{\emptyset_{vu}(\omega)} \qquad \text{Eq. (37)}$$

Using Equation (15-18) in the above equations will yield the following equations:

$$\frac{\emptyset_{wu}(\omega)}{\emptyset_{wy}(\omega)} = \frac{-\emptyset_{ww}(\omega) \cdot M^T(\omega)}{\emptyset_{ww}(\omega) \cdot S^T(\omega)} \qquad \text{Eq. (38)}$$

$$\frac{\emptyset_{vy}(\omega)}{\emptyset_{vu}(\omega)} = \frac{\emptyset_{vv}(\omega) \cdot Q^T(\omega)}{\emptyset_{vv}(\omega) \cdot M^T(\omega)} \qquad \text{Eq. (39)}$$

Substituting back $M(\omega) = \frac{C(\omega)}{I+P(\omega)\cdot C(\omega)}$, $Q(\omega) = \frac{P(\omega)\cdot C(\omega)}{I+P(\omega)\cdot C(\omega)}$, and $S(\omega) = \frac{I}{I+P(\omega)\cdot C(\omega)}$ in the above equations, we will obtain the estimates of the controller and plant as described below:

$$\frac{\emptyset_{wu}(\omega)}{\emptyset_{wy}(\omega)} = -C(\omega) \qquad \text{Eq. (40)}$$

$$\frac{\emptyset_{vy}(\omega)}{\emptyset_{vu}(\omega)} = P(\omega) \qquad \text{Eq. (41)}$$

From the above equations, we obtain estimates of the controller and the plant, respectively. Since the above equations do not contain the terms for the sensor and output noise; the *Joint Input-Output Approach* provides consistent estimates of both the plant and the controller. Thus, this analysis states that calculating the ratio of the cross-spectral density between the sensor noise and output, and the cross-spectral density between the sensor noise and input will allow us to estimate the plant in the frequency domain. Similarly, the ratio of the cross-spectral density between the output noise and input, and the cross-spectral density between the output noise and output will allow us to estimate the controller in the frequency domain. Therefore, even if we do not have any information about the plant or the controller, we can still obtain the estimate of the other [20].

3 Literature Review

3.1 Overview

This chapter reviews existing literature in the various domains of seated and standing balance. A particular focus will be on the domains of human body dynamics, sensory dynamics, neural dynamics, muscular dynamics, mechanical dynamics, and sensorimotor time delay, as well as on the domain of feedback control models in human balance.

3.2 Seated Balance

Seated balance is the ability of the upper body to stabilize itself against internal and external disturbances continuously. For example, these disturbances can occur in the form of breathing, supporting or carrying external loads, and experiencing a sudden or expected push (i.e., gravitational pull) [2]. The human body needs to detect these disturbances and respond to them appropriately. Aging individuals and those with various neurological or muscular impairments are often unable to maintain postural stability [1], [9]–[11]. As a consequence, such individuals have difficulties performing specific activities of daily living (ADL). Therefore, it is not surprising that 16.5% of individuals with paraplegia have considered seated balance and upper body strength as one of the most essential functions, even surpassing arm/hand (3.3%) and walking function (15.9%) [13]. Seated imbalance can also cause poor posture, which can potentially lead to secondary health complications such as kyphosis, pressures sores, or respiratory dysfunctions [14], [15]. Kyphosis is an excessive curvature of the spine in the outward direction that can lead to vertebral fractures and loss of musculoskeletal integrity [48], [49]. Pressure sores result from prolonged pressure on the skin surfacing a bony prominence and can lead to tissue loss and deep tissue injury [50]. Respiratory disfunction can lead to alveolar hypoventilation, diffusion problems and neuromuscular problems [51]. The severity and impact of seated imbalance have motivated further research on the quantification of the mechanisms of seated balance control and the development of more effective therapies and targeted interventions for affected individuals.

Seated balance in healthy individuals is generally achieved by a combination of two mechanisms: feed-forward and feedback control [17], [20], [26], [52]–[55]. In feed-forward control, the body anticipates an upcoming disturbance with the goal of counteracting the effect of the disturbance on the body's posture before or directly after the perturbation is experienced [56]–[59]. To maintain balance for such a scenario, the body executes a pre-programmed motor plan (often termed internal model) that has been developed through learning and previous experience [58]–[60]. In case of seated balance, for example, the body co-activates the antagonist muscles such that the overall stiffness of the trunk is increased [24], [61], [62]. Another example of feed-forward control is the immediate activation of the relevant muscles to prevent the body from tipping over in the event of an external push [63], [64]. However, feed-forward control alone is not sufficient to maintain dynamic seated balance, due to both unpredictable internal and external disturbances that cannot be anticipated, requiring fine adjustments to recover stability [25]. Therefore, the human body also relies on feedback control to stabilize itself against external disturbances. Feedback control often involves combination of active and passive control. In active control, the body's orientation in space is perceived by the sensory systems (*see Section 3.4: Sensory Dynamics*), such as the visual, proprioceptive, and vestibular systems. The acquired information is then passed on to the brain, which converts the sensory information into a motor command (*see Section 3.5: Neural Dynamics*). This motor command activates relevant muscles (*see Section 3.6: Muscular Dynamics*) and generates the active joint torques contributing to upper body stabilization (*see Section 3.3: Human Body Dynamics*). The process of transferring information from the sensory systems to the brain, integrating the sensory information, and sending the motor command to the muscular system involves various time delays (together known as sensorimotor time delay; *see Section 3.8: Sensorimotor Time Delay*). In passive control, stiffness and damping due to the mechanical properties of the involved muscles, ligaments, and surrounding tissue produce instantaneous, corrective joint torques (*see Section 3.7: Mechanical Dynamics*) that are not affected by time delays. These torques complement the active torques in stabilizing the upper body.

A significant body of literature has attempted to characterize and assess seated balance. Traditional methods to characterize seated balance are based on subjective and qualitative measurements [65]–[68]. These methods generally fail to identify the cause of impaired balance; therefore, recommended therapies and interventions based on such assessments may not be optimized for a given individual [69]–[71]. Therefore, it would be of clinical value to quantify the mechanisms

responsible for seated balance, such that the cause of a potential impairment can be identified. By gaining a better mechanistic understanding of seated balance control, targeted therapies and interventions can be developed and prescribed for affected individuals.

Two main methods exist for quantitatively identifying the mechanisms involved in seated balance: descriptive measures and system identification [20]. In descriptive measures, scientists and clinicians measure the biomechanical and electrophysiological features of balance. For example, a motion capture system tracks the body segments in three-dimensional (3D) space using markers placed on the body, with the goal of obtaining the body's center of mass (COM) fluctuations and the movement in the anterior-posterior (A-P) and the medio-lateral (M-L) direction during quasi-static sitting and standing [72]. In addition to the COM, also the center of pressure (COP) fluctuations are used to characterize balance for these tasks [29]. Metrics that use COM or COP fluctuations to characterize balance are known as posturographic measures. Some of the basic posturographic measures implemented in the literature are the displacement of the COP from the central point of the stabilogram, the total length of the COP path, the mean velocity of the COP, and the displacement of the COM from a stable position [73], [74]. Some of the more advanced posturographic measures involve divergence analysis, stabilogram diffusion analysis, and dimensionality analysis [74]–[76]. Many studies have assessed posturographic measures for standing balance [73], [77]–[79] and sitting balance [18], [27], [28], [80] after neurological impairments. One study also compared COP-based posturographic measures between standing and sitting and found specific commonalities and differences between the measures. The differences in posturographic measures were attributed to specific differences in seated and standing balance control strategies, and to other biomechanical factors [29].

Other devices can measure the kinematics and kinetics of the body or body segments, such as inertial measurement units (IMUs) [81], [82]. One study compared 38 different COM-based posturographic measures, which were calculated using IMUs, an optoelectronic system, and a force plate during unstable sitting. This study found that approximately half of the COM-based posturographic measures calculated from the IMUs were reliable against the same COM-based posturographic measures calculated from the optoelectronic system and force plate [83]. The same research suggested that implementing IMUs for obtaining COM-based posturographic measures of postural sway is valid.

Although descriptive measures prove to be effective in characterizing quasi-static balance or voluntary movements of the human body, they do not isolate the contributions of the different mechanisms involved in balance control [20]. To identify the various components of the seated balance, an external postural perturbation that triggers mechanical, sensory, or cognitive imbalances is required [20]. The technique by which the mechanisms of seated balance are identified using external postural perturbations is known as system identification (*see Section 1*). Researchers have obtained the sensitivity of the joint torque, the body sway, and the muscle activation with the external postural perturbations by applying the indirect approach to identify the frequency response functions (FRF) of various components involved in seated and standing balance [17], [20], [21], [36]. Some of the studies have identified the open-loop FRF by applying the joint input-output approach to identify various components in standing balance [22], [34], [42].

In the literature, many therapies and interventions have been described for individuals suffering under seated imbalance [84]–[90]. They include task-oriented training [91], [92]; treadmill training [93]; training using a balance board, a balance ball, or a gym ball [94]; and training in standing positions [95] to improve seated balance. Other methods used to enhance seated balance include dual-task training [96], trunk performance training [97], and visual feedback training [98]. To target a specific impairment in seated balance, a number of rehabilitation approaches have been used, including sensory rehabilitation (e.g., vestibular rehabilitation therapy [99], proprioceptive training programs [100], and visuomotor training programs [101]), muscle and movement rehabilitation [102], [103], and neural rehabilitation programs [104]. Despite these efforts, prescribing an optimal therapy remains a challenge to date. One approach to address this need is to quantify the mechanisms contributing to seated balance. For this purpose, the next sections will conceptually explore the various mechanisms involved in human balance control and the techniques to quantify them.

3.3   Human Body Dynamics

A human body is made of a unique physical structure, which enables it to perform many functional tasks. One of the essential tasks for the human body is to maintain a seated balance that further enables it to perform ADL such as sitting on a chair without falling or eating while sitting without problems. The human upper body accounts for more than half of the total body weight, with the

trunk weighing 43% of the total body weight, both the upper limbs weighing 13% of the total body weight and the neck and the head weighing 7% of the total body weight. The human skeleton is made up of bones that are connected to each other by ligaments. Bones provide rigidity to the body and help to protect soft tissues, e.g., the heart and lungs [105].

To facilitate the movement of different segments of the body and to maintain the skeletal structure, an extensive network of muscles is involved in this process. These muscles are known as skeletal muscles. Two other kinds of muscles are present in the body, i.e., cardiac (present in the heart) and smooth muscles (present in the organs, e.g., stomach, intestines, and bladder). The skeletal muscles are connected to the skeleton through tendons and are connected to other muscles through aponeuroses. The muscles produce the motion of a segment about a joint by pulling the bone of that segment in one direction. Two or more muscles are involved in producing motion in all possible directions about a joint. A pair of two muscles that produce contradictory motions are referred to as an agonist-antagonist pair. The agonist moves to its activation, and the antagonist opposes the movement produced by the agonist [105].

In similar studies, the human body has often been treated as a rigid body, i.e., the various segments of the human body have a constant mass, a constant geometry, and do not deform under the influence of external forces. The study of the motion of the body segments under the influence of external and internal forces is known as human body dynamics. It is difficult to directly measure the internal joint torques and the net muscle moment, as this requires force transducers that are directly inserted into the muscles, which is not deemed ethical in human studies. Thus, human body dynamics are primarily studied via indirect measures that include information about anthropometric measurements, body kinematics, and body kinetics [72], [105].

3.3.1 Anthropometric Measurements

The human body consists of various segments, such as the arms, legs, trunk, and head, which are linked together via biomechanical joints. These segments can be further divided into sub-segments. For example, each leg has two sub-segments (i.e., upper leg and lower leg). Each segment has its dynamics based on its mass, shape, and tissue distribution. Thus, it is essential first to identify the anthropometric parameters of different segments of the human body that can be used together with kinematic and kinetic data to obtain the dynamics of various segments.

In the literature, researchers have assessed the anthropometric measures of different segments of the body, such as the upper arm, the lower arm, individual digits, the upper leg, the lower leg, the foot, the trunk, the upper trunk, the lower trunk, several vertebral segments of the trunk, the neck, and the head in both living and non-living (cadaver) human beings [72], [106]–[117]. Several lumped anthropometric measures have also been obtained for specific research purposes, such as the head-arms-and-trunk (HAT) and lower body segments [72]. These parameters were obtained using mechanical torsion, photogrammetry [108], volumetric analyses [109]–[112], X-ray absorptiometry [115], [116], gamma-ray scanning [107], [114], [117], magnetic resonance imaging [106], and system identification techniques [20], [34].

3.3.2 Kinematics

The spatiotemporal movements of the body segments, termed kinematics, are needed to obtain human body dynamics.

3.3.2.1 Motion Tracking Devices

The body's kinematics can be obtained via motion tracking devices as summarized in Figure 3-1 [118]. Motion tracking devices can be divided into three categories: visual systems, non-visual systems, and robotic-aided systems.

Visual systems have the advantage of the ongoing advancement in optical sensor technology (e.g., cameras). Visual tracking can be performed by physically attaching markers to bony landmarks on the human body. This method is known as marker-based tracking. Visual tracking can be passive or active, depending on the marker-camera system being used [118]. In a passive system, the cameras emit infrared light that, upon reflection from infrared markers, is captured by the cameras [119]–[121]. In an active system, the marker itself emits light that can be detected by the camera system. Both the active and passive system then transforms the two-dimensional (2D) camera data into the 3D position of the markers using data from two or more cameras. Although active systems have the advantage of higher accuracy and sampling rate, passive systems can be wireless and less bulky [118]. Visual tracking systems with markers are considered as a "golden standard" in human motion tracking because the error in identifying the position of each marker is less than 1 mm [122], [123]. There are various types of marker-based visual tracking systems available on the market. Some of the leading passive tracking systems are VICON, Qualisys, and MacReflex motion capture systems. Among the active systems, Optotrack, CODA, and Polaris motion capture

systems have been extensively used in various areas of biomechanics research, particularly in seated balance, standing balance, and gait [118].
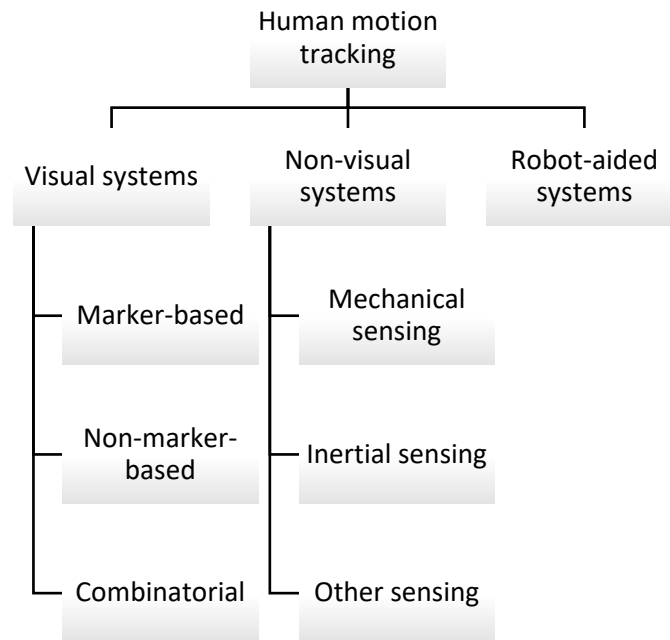
Figure 3-1: Summary of human motion tracking devices, adapted from [118]. Human motion tracking devices can be divided into visual systems, non-visual system and robot-aided system. Visual systems can be marker-based, non-marker-based, or a combination of both marker- and non-marker-based techniques. The non-visual system consists of mechanical sensing, inertial sensing and other sensing, e.g., acoustic and radio sensing.

Another type of visual tracking system does not use markers and is known as a non-marker-based visual tracking system [124]–[126]. Such visual tracking systems have gained popularity due to some of the limitations of the marker-based visual tracking systems. Marker-based visual tracking systems rely extensively on the accuracy of the placement of markers on the human body. The placement is subjected to human errors, as the identification of bony landmarks by an individual depends on their skills of precisely palpating the human body. Secondly, soft tissues artifacts that are caused by muscle contraction and sliding of skin underneath a given marker result in the undesired displacement of markers, resulting in noise-prone marker positions. Lastly, markers can

be occluded or fall off from the attached location during experimentation and produce missing data [118], [122], [123]. These limitations can be overcome with high speed and high pixel camera systems [118]. These high speed/high pixel camera systems record a video of the motion at a high sampling rate, which is post-processed to track the motion of the human body segments. Tracking can be done in 2D, where the 2D shape of individual segments are tracked, or in 3D, where model-based tracking and feature-based tracking are employed [118]. Non-marker-based systems, though accurate, are expensive and require extensive computational resources [127]. A third technique that possesses advantages of both marker- and non-marker-based systems is known as combinatorial tracking. In this tracking, both markers and high-resolution video cameras are used to track human movement, compensating for specific limitations [128].

Non-visual systems consist of sensing techniques that can capture human motion using non-visual-based sensing techniques. These can be divided into mechanical, inertial, acoustic, radio, magnetic, and microwave sensing [118]. Some of these technologies are still being developed, with the goal of reaching the performance of visual-based tracking systems. The most reliable and validated techniques in non-visual-based sensing are mechanical sensing and inertial measurement-based sensing. Other sensors (mentioned above) are sometimes added to these two sensing techniques for improving the overall sensing capabilities of the system. Mechanical sensing was one of the early techniques to track human motion quantitatively, and it involves the use of goniometers (essentially an electric potentiometer) to measure human body joint angles [72], [129]. Inertial sensing includes the use of accelerometers, gyroscopes, and magnetometers that provide information on linear acceleration, angular velocity, and magnetic field strength, respectively. Inertial sensing is performed through IMUs, where IMUs data could be used to derive the kinematics and kinetics of a rigid body [130]. Studies have compared the motion tracking capacity of IMUs and motion capture systems in seated balance, standing balance, and gait, and have found comparable IMUs performance [131]–[136]. IMUs provide a wireless and out-of-lab environment solution for human motion tracking [118].

Robot-aided systems are primarily implemented as therapeutic devices, where neuro-rehabilitation is provided for post-stroke human limbs. The robot-aided systems implement electro-mechanical or electromagnetic sensing technologies that can track human motion and provide feedback to the

affected individuals for rehabilitation. Some of these systems include Cozens, MIT-MANUS, MIME, and ARM Guide [118].

3.3.2.2 Marker-based Motion Capture Systems

The marker-based motion capture system's markers are either placed directly on anatomical landmarks of the body or a plate or cuff with three or more markers, which is then placed on a body segment. The movement of the markers is then recorded via the motion camera system [71], [137]–[142]. Marker type and placement vary from study to study [8], [17], [21], [22], [34], [42]. A marker's location in 3D space is obtained in a pre-defined frame of reference. A local coordinate system is defined to calculate the joint angles between two segments based on the markers attached to the segments being examined [72]. A local coordinate system (x, y, z) is defined in Figure 3-2 using the instantaneous position vectors (d_a, d_b, d_c) of three markers with respect to the global coordinate system (X, Y, Z). The local coordinate system can be defined using Equation (42), where (x, y, z) were used to define the local coordinate system; (d_a, d_b, d_c) were the position vectors of the markers with respect to the global coordinate system (X, Y, Z); and y' is the intermittent axis used to calculate the z-axis of the local coordinate system.

$$x = \frac{d_c - d_a}{\|d_c - d_a\|} \ , \ y' = \frac{d_b - d_a}{\|d_b - d_a\|} \ , \ z = \frac{x \times y'}{\|x \times y'\|}, \ y = z \times x \qquad \text{Eq. (42)}$$

To obtain the position of the origin and the orientation of the axes from one coordinate system to another, the transformation matrix (T) as mentioned in Equation (43) was applied, where p_{ij} are the rotation terms for i and j varying from 1 to 3; and a, b and c are the translation terms [119].

$$T = \begin{bmatrix} p_{11} & p_{12} & p_{13} & a \\ p_{21} & p_{22} & p_{23} & b \\ p_{31} & p_{32} & p_{33} & c \\ 0 & 0 & 0 & 1 \end{bmatrix} \qquad \text{Eq. (43)}$$

Obtaining the flexion-extension angle, the lateral bending angle, and the axial rotation angle is often of interest [143]. The rotation matrix obtained through a Cardan sequence of rotations is presented in Equation 44, where (α, β, γ) are the Euler angles [144].

$$R_{ZYX}(\gamma, \beta, \alpha) = \begin{bmatrix} cos\beta cos\gamma & -cos\beta sin\gamma & sin\beta \\ sin\alpha sin\beta cos\gamma + cos\alpha sin\gamma & -sin\alpha sin\beta sin\gamma + cos\alpha cos\gamma & -sin\alpha cos\beta \\ -cos\alpha sin\beta cos\gamma + sin\alpha sin\gamma & cos\alpha sin\beta sin\gamma + sin\alpha cos\gamma & cos\alpha cos\beta \end{bmatrix}$$

$$\text{Eq. (44)}$$

25

The rotation matrix obtained from Equation (44) was written as Equation (45). The angles (α, β, γ) were obtained through Equations (46-48), where $Atan2(y, x)$ computes the inverse tangent of $\frac{y}{x}$ by considering the sign of both x and y to determine the quadrant of the estimated angle [143].

$$R_{ZYX}(\gamma, \beta, \alpha) = \begin{bmatrix} p_{11} & p_{12} & p_{13} \\ p_{21} & p_{22} & p_{23} \\ p_{31} & p_{32} & p_{33} \end{bmatrix}$$

Eq. (45)

$$\beta = Atan2(p_{13}, \sqrt[2]{p_{23}^2 + p_{33}^2})$$

Eq. (46)

$$\alpha = Atand2(\frac{-p_{23}}{\cos\beta}, \frac{p_{33}}{\cos\beta})$$

Eq. (47)

$$\gamma = Atan2(\frac{-p_{12}}{\cos\beta}, \frac{p_{11}}{\cos\beta})$$

Eq. (48)
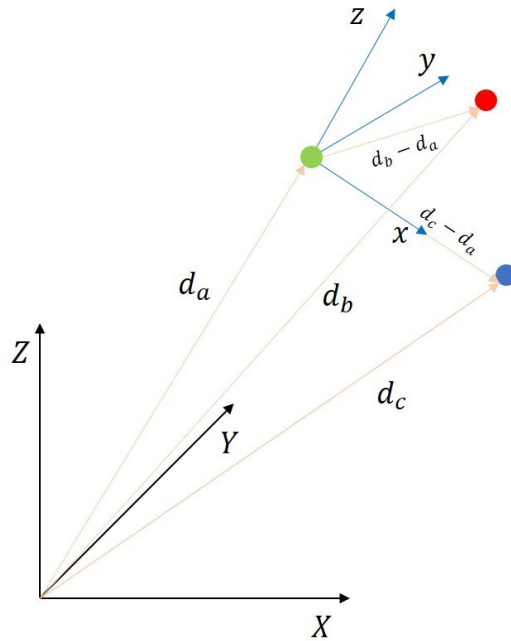
Figure 3-2: The local coordinate system (x, y, z) is defined by using the instantaneous position (d_a, d_b, d_c) of the markers with respect to the global coordinate system (X, Y, Z)

3.3.3 Kinetics

In the previous two sections, the segment's anthropometric measurements and the tracking of the motion of each segment in 3D space were discussed. The motion of a segment is the effect of the

26

forces acting on the segment. The type of forces acting on a segment includes the gravitational force, ground reaction forces, tensile forces, and muscle and ligament forces. The study of the forces acting on a mechanism is known as kinetics. We required an understanding of all the forces acting on a segment to have complete knowledge of human segment dynamics [72].

3.3.3.1 Link-segment Model

The human body consists of various segments. To evaluate the dynamics of each segment, human body segments can be represented via a link-segment model. In what follows, we describe the assumptions that are considered in the literature to develop such models [72].

- ➢ all segments have a constant mass, and the mass is located at the COM location of that segment;
- ➢ the location of the COM is fixed and should not change during the movement of the segment;
- ➢ the joints are approximated by a hinge or ball-and-socket joints depending on the degrees of freedom of the respective joints;
- ➢ the moment of inertia of the segment remains constant when calculated from a fixed axis. This axis could pass through the COM location, the distal joint, the proximal joint, or any user-defined axis of rotation on the segment; and
- ➢ the length of the segment is fixed during the movement of the segment. The length of a segment is defined as the distance between the proximal and distal joints of the segment.

An example of a link-segment model of the human upper body is presented in Figure 3-3. The model has two segments, including the HAT and legs segment, and one joint at the fifth lumbar vertebra. The mass of the HAT segment (m_{com}) is concentrated at the COM location of the HAT segment. The axis of rotation is passing through the fifth lumbar vertebra in the frontal plane. The length between the COM and axis of rotation is defined as l_{com}. The free body diagram of the single link-segment model is also shown in Figure 3-3, where $m_{com} \cdot g$ is the force due to gravity on the upper body, and F_y and F_z are the ground reaction forces in the anterior direction and the vertically upward direction, respectively. The ground reaction forces are assumed to be applicable at the COP location. The distance of the COP location from d_{L5} in the A-P direction is represented by d_{COP}, and the distance between the base of support and the fifth lumbar vertebra is represented by d_{L5} [72], [117].
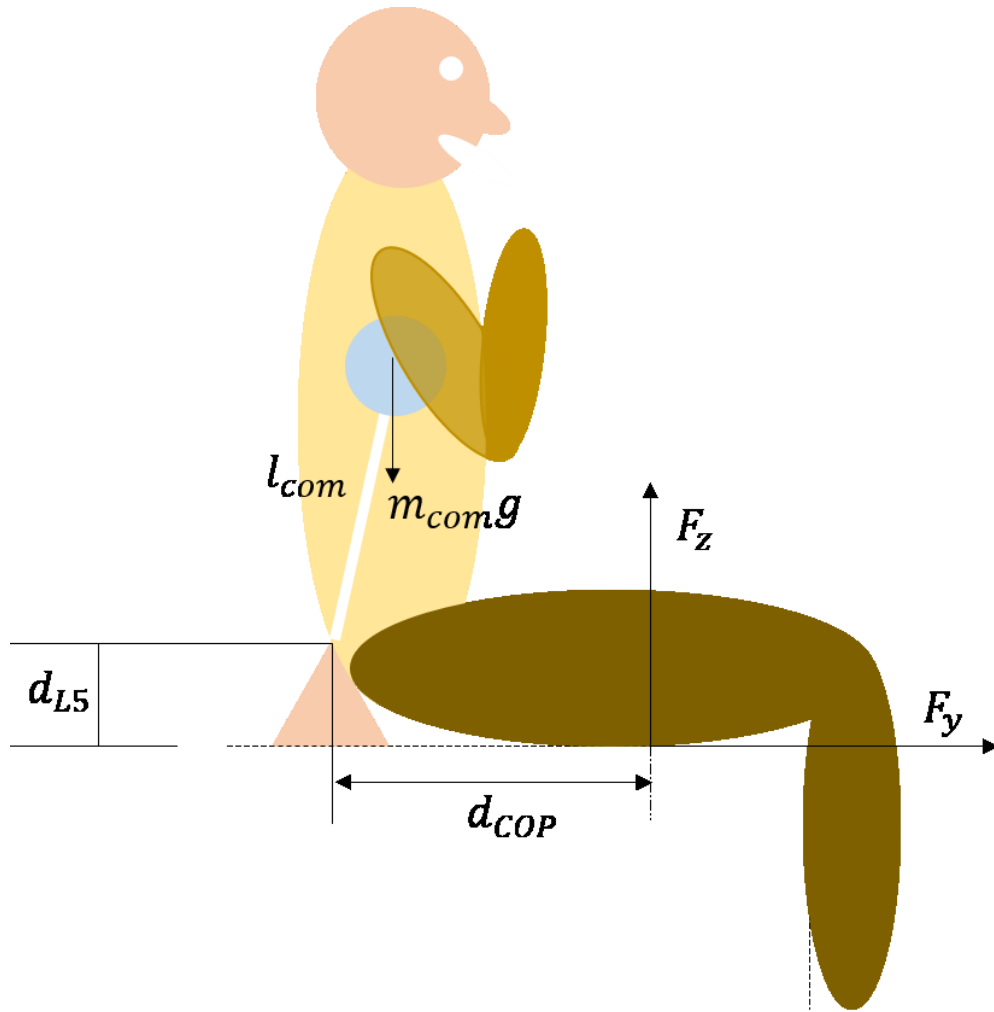
Figure 3-3: A link-segment model of the upper body, including two segments: the head-arms-trunk and leg segments, which are connected via a joint at the fifth lumbar vertebra. The upper body mass (m_{com}) is situated at the center of mass (COM) location of the upper body. l_{com} is the distance between the COM and the fifth lumbar vertebra. F_y and F_z are the ground reaction forces in the anterior direction and the vertically upward direction, respectively. d_{COP} is the distance of the center of pressure location from d_{L5} in the anterior-posterior direction. d_{L5} is the distance between the base of support and the fifth lumbar vertebra.

3.3.3.2 Force Plate

The force-sensing devices measure the forces exerted by the human body on another body. Force can be measured using a force transducer that will produce an electrical signal proportional to the applied force. Some of the available force transducers are piezoelectric transducers, strain gauges,

piezoresistive transducers, and capacitive force-sensing devices. The external force produces a small strain on the device that is measured by the force transducers and converted into a voltage output. To measure forces in multiple directions, bi-directional or tri-directional force transducers (that have two or three force transducers, respectively) are mounted orthogonally (X, Y, Z) to each other [72].

Among commercially available force-sensing devices, force plates are a frequent choice. They measure the ground reaction forces and moments for many activities [145], [146]. There are two types of force plates: the first type has four triaxial transducers supporting a flat plate, and the second type has a centrally instrumented pillar that supports a flat plate. Force plate data can be used to calculate the COP. The COP can be calculated as described in Equation (49-50), where a and b are the coordinates of the COP in the M-L and the A-P directions, respectively; M_y is the moment in the A-P direction; M_x is the moment in the M-L direction; F_x, F_y and F_z are the forces in the A-P, the M-L, and the vertically upwards directions, respectively; and d is the distance between the force plate transducer and the top of the plate.

$$a = \frac{M_y + F_x * d}{F_z} \qquad\qquad \text{Eq. (49)}$$

$$b = \frac{M_x + F_y * d}{F_z} \qquad\qquad \text{Eq. (50)}$$

Some devices can measure the distribution of a force on the base of support, e.g., pressure soles [147]. Such devices are useful when knowledge of the exact distribution of a force on the base of support is required. For example, during midstance in walking, the heel and the forefoot of the foot produce pressures at two different parts of the foot. Force plate data are not able to distinguish between these two pressure components; therefore, devices like pressure soles prove effective [72].

3.3.4 Dynamics of Seated Balance using First Principles and Biomechanical Measurements

The dynamics of seated balance can be quantified by utilizing anthropometric measurements (*see Section 3.3.1*), kinematics measurements (*see Section 3.3.2*), and kinetic measurements (*see Section 3.3.3*). For seated balance, consensus exists that the body stabilizes the HAT segment above the lower body, such that lower body remains stable and static with respect to the base of support [17], [19], [148], [149]. Studies have modelled the HAT segment to be a single-link inverted pendulum (Figure 3-4), with the mass of the HAT segment being concentrated at the 3D

COM location of the HAT segment. The COM is connected to the pelvis by a massless rod. The axis of rotation is considered at the pelvis, particularly between the fourth and the fifth lumbar vertebrae [8], [17], [33], [149], [150].

The dynamics of the single-link inverted pendulum model of human seated balance was obtained via the following analysis [151]: The torque produced at the joint was estimated using a top-down, inverse dynamics approach. To calculate the joint torque using this approach, consider Figure 3-4, where the mass of the HAT segment is attached to the massless rod. The length of the rod is the distance between the COM location of the HAT segment and the fifth lumbar vertebra. The angle θ represents the deflection of the inverted pendulum from the vertically upward direction. τ represents the joint torque produced to correct the deflection. l_{COM} represents the distance between the fifth lumbar vertebra and the COM. d_{COP} represents the distance of the COP from the fifth lumbar vertebra in the A-P direction. F_y and F_z are the ground reaction forces in the A-P and the vertically upward directions, respectively. The joint torque using the top-down approach can then be calculated using Equation (51), where τ is the joint torque; J is the moment of inertia about the axis of rotation; α is the angular acceleration; m_{com} is the mass of the upper body; g is the acceleration due to gravity; l_{com} is the length between the joint and the COM; and θ is the angular displacement of COM:

$$\tau = J\alpha - m_{com}gl_{com}sin\theta \qquad \text{Eq. (51)}$$

For small variations in θ (~ 0 to 5 degrees), we can approximate Equation (51) by Equation (52).

$$\tau = J\alpha - m_{com}gl_{com}\theta \qquad \text{Eq. (52)}$$

Assuming zero initial conditions, transforming Equation (52) into Laplace domain yields the following transfer function of the single-link inverted pendulum model. This transfer function represents the dynamics of a single-link inverted pendulum:

$$\frac{\theta}{\tau} = \frac{1}{Js^2 - m_{com}gl_{com}} \qquad \text{Eq. (53)}$$
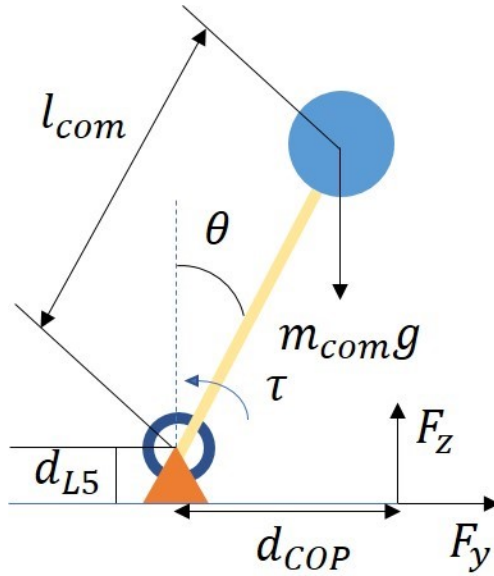
Figure 3-4: Inverted pendulum model of human seated balance. The mass of the head-arms-trunk (HAT) segment is attached to a massless rod, and the length of the rod is the distance between the center of mass location of the HAT segment and the fifth lumbar vertebra. θ is the angle, or angular deflection, of the inverted pendulum from the vertically upward direction. τ is the joint torque produced to counteract the deflection. d_{L5} is the distance between the fifth lumbar vertebra and the base of support. d_{COP} is the distance of the center of pressure from the fifth lumbar vertebra in the anterior-posterior (A-P) direction. F_y and F_z are the ground reaction forces in the A-P and the vertically upward directions, respectively.

The joint torque was also obtained using the bottom-up, inverse dynamics approach as reflected in Equation (54), where d_{L5} is the distance between the base of support and the fifth lumbar vertebra, d_{COP} is the COP location in the A-P direction, and F_y and F_z are the ground reaction forces measured by the force plate in the A-P and the vertically upward direction, respectively:

$$\tau = d_{L5} \times F_y + d_{COP} \times F_z \qquad \text{Eq. (54)}$$

The human vertebral column, or spine, consists of 33 different vertebrae that are separated from each other via intervertebral discs [105]. Each vertebra has a degree of freedom in the A-P and the M-L directions. The vertebral column is also divided into regions, namely, the cervical region, the thoracic region, the lumbar region, the sacrum region, and the coccyx region. Researchers have

modelled the human spine as a multi-link system, with each link having mass based on the anthropometric characteristics of each vertebra [119], [152]. The joint from one link to the next is assumed to be located at the intervertebral disc between regions (cervical, thoracic, and lumbar) or between vertebras. Implementing a top-down or bottom-up, inverse dynamics approach, the moments acting at each joint and the forces acting on each link can be calculated for multi-link models [72], [153]–[155].

3.3.5   Identification of Human Body Dynamics using System Identification

Researchers have modelled the dynamics of the human body using system identification, where a sensory perturbation is applied and neuromusculoskeletal time series such as body sway, joint torques, and/or weighted electromyography (EMG) are measured in response to that perturbation. To estimate the human body dynamics using this method, both the indirect (*see Section 2.3.2*) and/or the joint input-output approaches (*see Section 2.3.3*) have been implemented [8], [33], [34]. One of the models for upper body dynamics as identified by some of these studies is presented in Equation (53).

3.4   Sensory Dynamics

Three main sensory systems exist that can detect the 3D orientation of the human body in space: the visual system, the vestibular system, and the proprioceptive system. The body also regulates balance with the help of other somatosensory systems, where information about touch, pain, temperature, and vibration is utilized, along with information from the already mentioned sensory systems [21], [156]–[158].

3.4.1   Visual System

The visual system is part of the central nervous system (CNS) and has two main functions: (i) to process visual information, and (ii) to use non-image photo response functions. Visual information processing involves the reception of visible light and monocular image formation in the eyes; and the combination of 2D images obtained from each eye into one 3D image within the optic tract [159]. Non-image photo response functions include the circadian photoentrainment and pupillary light reflex [160].

The visual system is also believed to be involved in postural control in seated balance [21], [36], [161]. It has been shown that the visual system is the significant contributor to balance, surpassing the role of both the vestibular and proprioceptive systems [162]. Factors such as the environment perception clarity, the size of the visual field, the perceived depth, and the light and glare susceptibility play a significant role in the postural control of balance [163]. Many studies exist that artificially alter the visual information (physical motion of a screen or virtual motion of the image on the screen) or study disrupted visual information due to a disease (cataracts), with the goal of assessing their effects on balance. Such studies have shown that deprived or corrupted visual information leads to degraded balance [8], [21], [34], [164]–[166].

3.4.2 Vestibular System

The vestibular system is a major contributor to the sense of spatial orientation and balance [11], [21], [167]–[170]. It is part of the auditory system, being contained within the cochlea and the labyrinth of the inner ear. The vestibular system consists of two components: the semicircular canals to detect rotational motion of the head, and the otoliths to detect linear motion of the head. The vestibular system transmits signals to the brain, which in turn may activate muscles involved in postural control and/or to the neural structures involved in eye movement control (vestibulo-ocular reflex). The latter is required for stable vision [21], [167], [171], [172].

The vestibular system plays a vital role in human postural balance. There have been many studies that have assessed the role of the vestibular system in human stance control [21], [34]–[36], [167]–[170], [173]. Galvanic vestibular stimulation has been applied to excite the vestibular nerve fibers that can alter or corrupt the vestibular information and the biomechanical outcomes, including COP, COM, and gait parameters [169], [173].

3.4.3 Proprioceptive System

The proprioceptive system can sense the movement of joints in 3D space, but also the body's tissue movement, pain, and hunger [174]. Proprioception is achieved via specific receptors known as proprioceptors. They are present in tendons (Golgi tendon organs), skeletal striated muscle (muscles spindles), and the joints' fibrous capsules [174], [175]. The information provided by the proprioceptive and vestibular systems is often combined by the brain, along with other sensory information, to create a complete sense of the kinematic state of the body [21].

To disturb proprioceptive information, research studies have used rotations applied to the base of support of human test participants, demonstrating that this paradigm resulted in increased body sway during quiet standing [176]–[179]. Another study assessed the role of the proprioceptive system in stabilizing the trunk. The authors concluded that the proprioceptive system assists with stabilizing the trunk above the pelvis. However, this study also mentioned that trunk stability is primarily achieved via vestibular and visual information [180].

3.4.4 Models of Sensory Dynamics

The process of sensing the body's orientation in space by the visual, vestibular, and proprioceptive systems and of transferring this information to the CNS is referred to as sensory dynamics. Researchers have estimated models of the sensory dynamics by artificially stimulating individual sensory receptors. Methods used include galvanic vestibular stimulation [181] or muscle/tendon vibration [179], providing transient stimuli (for example, a perceived movement of the base of support [176], [182], [183]), and the application of motion stimuli (for example, rotating the base of support and/or visual surround [8], [21], [34]–[36]). The biomechanical and electrophysiological features (e.g., body kinematics, muscle activity, and ground reaction forces) of the human body are recorded. System identification techniques have been applied to identify the sensory dynamics [20], [21].

Each sensory system has a different sensory reference. For example, the visual system takes visual cues from the environment, the vestibular system captures deviations from the direction of gravity, and the proprioceptive system assesses, for example, the flatness of the base of support. The body's deviation from a reference orientation is sensed by the sensory systems, with the sensory information being combined linearly. One hypothesized concept of such linear combination is that each sensory system uses an individual weight, and the sum of all sensory weights is equal to one [21].

Some studies have identified a non-linearity in the sensory dynamics, which has been attributed to sensory channel re-weighting. In this process, the brain can dynamically change the weights for each sensory modality, termed *dynamic regulation in sensory dynamics*. This regulation is essential since, if information from one sensory system becomes corrupt or unavailable, the CNS can rely on other sensory information to maintain balance. For example, suddenly closing the eyes while standing on an unstable support surface will cause the brain to rely more heavily on

vestibular and/or proprioceptive information. If all sensory information is available, researchers have considered the sensory dynamics to be unity [21], [35], [157].

3.5 Neural Dynamics

The process by which the sensory system information is converted into motor commands in the CNS through active feedback control is defined as the neural dynamics.

3.5.1 Central Nervous System

The human brain, together with the spinal cord, is part of the CNS. In the CNS, all the information from various senses are received, processed, and an appropriate response (e.g., motor commands to muscles) is created. The human brain is also believed to be involved in domains related to language, creativity, thinking, reasoning, emotions, and memory. The human brain consists of the cerebrum (the most substantial part of the brain), the cerebellum, and the brain stem. The cerebrum is further divided into two cerebral hemispheres, where each hemisphere consists of a frontal, a temporal, a parietal, and an occipital lobe. The frontal lobe is associated with motor function, memory, language, judgement, planning, reasoning, and social behavior. The temporal and occipital lobes are primarily associated with auditory and visual perception, respectively. Two functional regions exist in the parietal lobe: one of the regions is involved in perception and sensation, and the other in integrating sensory information [184].

The cerebellum is involved in receiving information from various sensory systems, the spinal cord, and other parts of the brain. It is involved in voluntary motor movements, such as balance, posture, speech, and coordination. It helps in producing smooth and balanced muscular activity in motor movements. The brain stem controls the flow of information from the brain to the rest of the body. It is also involved in the control of breathing, heart rate, blood pressure, swallowing, consciousness, and sleep [184].

The spinal cord is made up of nervous tissues and support cells that extend from the brain stem to the lumbar vertebra. It is involved in the passage of information, acquired from sensory systems to the brain. It also acts as a channel to transfer the motor cortex information from the brain to the targeted muscles group. The spinal cord is also responsible for minor reflex actions such as the withdrawal reflex [185].

3.5.2 Control of Human Seated Balance through CNS

The control of human seated balance is a complex process that involves a series of steps as shown in Figure 3-5. Information on balance performance is sensed by visual, vestibular, and proprioceptive systems and converted into electrical signals that are further transmitted to the brain. Both the visual and the vestibular systems send information directly to the brain stem, whereas the proprioceptive system sends information to the brain stem through the spinal cord [186]. In the brain stem, balance information from these sensors is isolated from other information (for example, the body's distance to an object is separated from the color of the object in the visual image) and integrated to obtain a complete sense of balance performance. The integrated balance information is then passed on to the cerebellum, which combines it with past knowledge (via learning) sent by the cerebrum, to generate motor commands [21]. Simultaneously, the generated motor commands are transferred to the cerebrum for storage, learning, and future requirements. It has been proposed by many studies that the motor commands are generated based on the body's orientation and velocity with respect to an axis of the body [8], [22], [26], [187]. Some other studies argue that the motor commands are also affected by the body's acceleration with respect to such axis [8], [22]. Furthermore, the eye's gaze is kept stable by the brain to produce an accurate visual estimation of the body's orientation in space through the vestibulo-ocular reflex. Finally, the motor commands pass through the spinal cord to reach the muscles, facilitating postural adjustments ensuring seated balance [186], [188].

3.5.3 Identification of Neural Dynamics using System Identification

Several studies have identified the non-parametric estimates of the neural dynamics using system identification in standing and seated balance [8], [17], [22], [33]. As mentioned previously, to identify the controller, the external output noise should dominate the intrinsic output noise. In the literature, studies have implemented multi-sinusoidal and/or filtered white noise signals as the external output noise signal [8], [17], [20], [22], [30], [42], [189], [190].

As mentioned previously, the HAT segment dynamics can be modelled as a single-link inverted pendulum. It has been shown in a previous study that a proportional derivative (PD) controller is sufficient to balance a single-link inverted pendulum [191]. Some studies have fitted the neural dynamics to basic controllers, such as a proportional-integrative-derivative (PID) controller [17], [21], [35], [36], [178], a PD controller [26], [189], and a PD controller with acceleration feedback

[8], [192], [193] in standing and seated balance. Other studies have fitted the neural dynamics to more advanced controllers, such as neural network models and genetic algorithm models [191], [194]–[198]. The PD controller and PD controller with acceleration feedback were implemented in a feedback control model representing human standing balance in a simulation software, and both controllers were able to balance the single-link inverted pendulum model [8], [26].
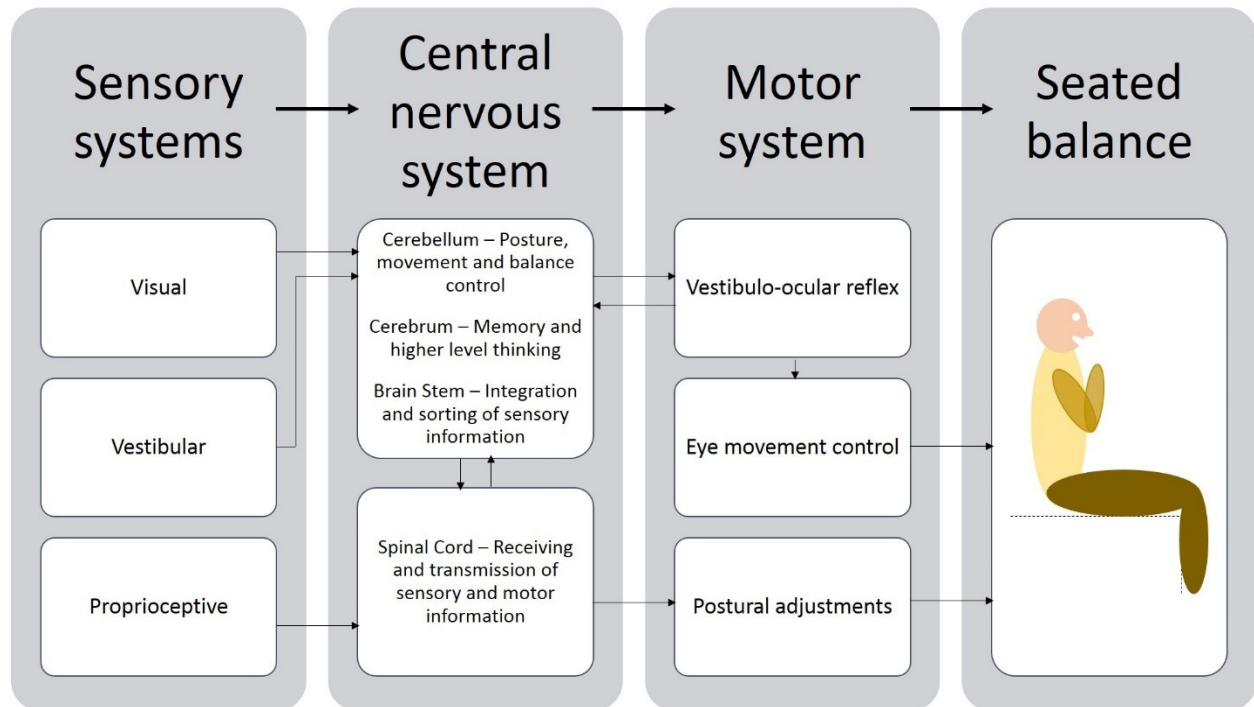
Figure 3-5: Overview of the process of neural dynamics (adapted from [186]). The neural dynamics involve the acquisition of information from sensory systems (visual, vestibular and proprioceptive systems). The information is then passed on to the central nervous system. The brain stem integrates and sorts the sensory information related to balance. The cerebellum then develops motor commands based on the brain stem's information and past knowledge sent by the cerebrum. The eye's gaze is kept stable to produce an accurate visual estimate of the body's orientation in space through the vestibulo-ocular reflex. Final postural adjustments are made for seated balance through the activation of relevant muscles.

3.6   Muscular Dynamics

Skeletal muscles are responsible for the stability of the human skeleton and the motion of all joints. These muscles are also responsible for establishing and maintaining seated balance at the instruction of the neuromuscular controller, which is influenced by internal and external disturbances that affect stability [72]. Thus, in this section, we discuss the underlying physiology of skeletal muscles, the muscles involved in seated balance, techniques for measuring electrical activity in muscles, and the modelling of the muscular dynamics, which is the process of generating torque in response to neuromuscular signals.

3.6.1   Physiology of muscles

The smallest unit that can be controlled by a motor neuron in human skeletal muscles is the *motor unit*. A motor unit consists of a motor neuron (starting from the synaptic junction between the motor neuron and the ventral root of the spinal cord to the motor neuron axonal terminal) and the muscle fibers innervated by the motor neuron. Each motor neuron can control a range of muscle fibers, varying from 3 to 2000, depending on the level of control required by that muscle [199]. Muscle fibers vary in length depending on location in the body. For example, muscle fibers of eyes, fingers, and face are shorter in length than the muscles fibers in the legs and trunk. Each muscle fiber is approximately 100 μm in diameter and consists of many *fibrils* that are each approximately 1 μm in diameter. Each fibril consists of many *filaments*, each of which has a diameter of approximately 100 Å. Each filament is made of several *actin* and *myosin* elements, together forming a contractile element called *sarcomere*. Tension in a muscle is produced by the sarcomere. The basic structure of a sarcomere is shown in Figure 3-6. The thin actin filament slides past thick myosin filaments by way of the cross-bridges (cross-hatched lines). This causes the sarcomere to reduce its length and produce tension in the muscle. The contractile elements are contained within *fascia*, which enclose the muscle, separate muscles into layers and groups, and connect muscles to the tendons [72].

The brain independently controls all the motor units in a muscle, and the recruitment process of each motor unit depends upon the *size principle* [72], [200]. The size principle states that, when the tension of muscle increases, the next recruited motor unit will have a larger size in comparison to the previously recruited motor unit. Each neural signal to the motor unit produces a twitch of tension in the muscle fiber. Thus, maintaining a constant tension in the muscle can be achieved in

two ways: (i) by increasing the simulation rate when sending repetitive brain signals; and/or (ii) by the recruitment of additional motor units [72]. Each motor unit has a maximum firing rate, and this rate is achieved well after the next motor unit is recruited [201].
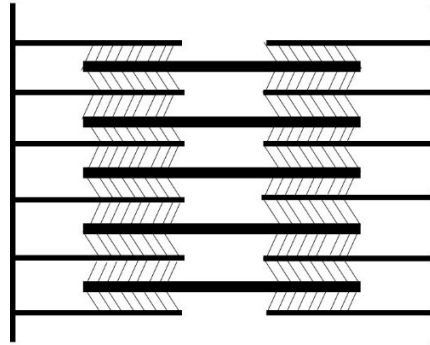
Figure 3-6: A basic structure of a sarcomere. Thick myosin filaments remain stable and thin actin filaments slide over it with the help of cross-bridges (cross-hatched lines).

3.6.2 Muscles Involved in Seated Balance

It is well established that there are many muscles in the trunk as well as the lower limbs that assist in seated balance through active feedback control. Muscles in the human body have been categorized as superficial, intermediate, and deep muscles. Invasive techniques are required to acquire the precise activity of intermediate and deep muscles. Surface EMG, which requires the electrodes being placed on the skin to measure a muscle's activity with reasonable accuracy, can be used for superficial muscles. Thus, the role of superficial muscles in seated balance can be studied through non-invasive measures. Superficial muscles have been divided into flexors causing the body segments to bend inwards, and extensors causing the body segments to bend outwards [72].

It has been reported that the trunk flexors involved in upper body stabilization include the rectus abdominis (RA), internal obliques, and external obliques (EO) muscles [202]–[207]. RA contributes to trunk flexion and to resisting a trunk displacement in the posterior direction. Internal obliques and EO contribute to trunk bending in the lateral and anterior directions and to axial rotation of the body in the transverse plane [208]. The trunk extensors include the erector spinae (ES) muscle that spans the whole back [208]. ES consists of three muscle groups, i.e., the

longissimus, spinalis, and iliocostalis muscles [208]. These muscle groups are involved in extending the back in an upright posture, and in resisting forward trunk displacement during a sudden forward push (trunk) or a sudden backward acceleration (base of support) [209]–[211].

Other superficial muscles exist that are involved in upper body stabilization. For example, the latissimus dorsi, which is on the dorsolateral side of the trunk, is involved in arm and shoulder movement, and lateral movement of the lower trunk [208]. A few muscles in the legs, e.g., the rectus femoris (RF) and biceps femoris (BF), are indirectly involved in trunk stabilization. The primary function of RF and BF relates to flexion and extension of the upper leg, respectively. They also produce stability of the trunk through stabilizing the pelvis above the pelvis via hip flexion and extension [212]–[216].

3.6.3 Electromyography (EMG)

Muscle contraction is accompanied by the generation of electrical signals that can be measured using a technique called electromyography (EMG). These electrical signals include the signal generated from the release of neurotransmitters by the motor axons (also known as end plate potential), the signal associated with electrical potentials in muscle tissue to recruit motor units, and the signal reflecting the influx and outflux of several ions throughout the muscle contraction process. The signal that can be detected by EMG is the second, i.e., the one due to the electrical potentials in muscle tissue. It is called a *motor unit action potential*. Electrodes used in EMG capture the algebraic sum of several motor unit action potentials travelling across the muscle fiber at a given moment [72].

EMG can be applied via both invasive and non-invasive methods. Invasive EMG involves the use of indwelling electrodes that are placed under the skin, while non-invasive EMG involves the use of surface electrodes. Surface electrodes and therefore non-invasive EMG is a preferred choice for superficial muscles, while indwelling electrodes and invasive EMG is preferred for intermediate or deep muscles. Invasive EMG is also used to record activity associated with subtle movements. The improved reproducibility of the data from surface electrodes versus indwelling electrodes for the same muscle suggests that surface electrodes are a better choice [217]. Surface electrodes are usually a metallic disk made up of silver/silver chloride, with a diameter close to 1 cm. There are other commercially available electrodes, for example, 2D array electrodes [218]. Indwelling

electrodes are hypodermic needles, with the conductor insulated from the outside and a bare end at the tip of the needle, with the diameter range of 2 to 15 mm [72], [219].

Some variables affect the quality of an EMG signal, particularly for surface electrodes. Among these factors is the propagation velocity of the signal in the muscle fiber, the distance between the electrode and muscle in consideration, the depth of the muscle fiber, and the electrode surface area [72]. It has been shown that electrodes with a small surface area produce a higher quality signal as compared to those with a larger surface area [220]. The same research has also shown that motor unit action potentials can be detected via electrodes that are very close to the motor units and, thus, the chance of also capturing signals from nearby muscles (crosstalk) is minimal.

Surface EMG requires the use of two electrodes that measure the voltage between two different muscle locations. In addition, a reference electrode is placed on a bony landmark (e.g., elbow or clavicle), allowing the removal of signals that are not due to the activity of the targeted muscle (e.g., heart rate). The voltage difference measured with the two main electrodes needs to be amplified to log the signal with physical instruments. EMG signals recorded from surface electrodes have a maximum voltage of 5 mV peak to peak. This signal is amplified such that the range of the amplified signal is within the range of the acquisition device. Good bio-amplifiers provide variability of ranges such that the amplified signal can be recorded optimally and without any clipping [72].

An electrode attached to the skin has a finite impedance that depends on the skin thickness, the amount of dead skin under the electrode, the surface area of the electrode, and the temperature at the contact site. These impedances cause a drop in the voltage signal acquired with the electrodes. Thus, there is a need for a high input impedance of the amplifier that can protect the EMG signal from attenuation. It is recommended to have an input impedance of 1 MΩ or higher and to have a skin impedance of less than 1000 Ω. The skin impedance can be reduced by sterilizing the skin. Usually, the skin is shaved to remove hair from the targeted skin area, and the area is wiped with alcohol to remove any dead skin. For many EMG systems, there is the need to add gel between the electrode and the skin to reduce the overall impedance of the skin-electrode interface [72], [221].

Another characteristic that needs to be looked upon in EMG amplification is the frequency bandwidth of the obtained signal. It has been reported that EMG recordings have a meaningful signal between 10 and 1000 Hz [72]. Thus, it is required that the EMG measuring instrument not

attenuate any frequency content of the signal within the above range. Attenuation of the signal outside of the EMG frequency bandwidth can reduce noise that is below 10 Hz (movement artifacts) and above 1000 Hz. However, several sources of noise, e.g., due to heart contractions at 100 Hz and the general power line (60 Hz), have frequencies within the frequency bandwidth of the signal and cannot be removed at this stage [72].

EMG is affected by the presence of radiations from domestic power sources, such as electronic machinery, power cables, and fluorescent lighting. These radiations add noise to the recorded EMG data known as hum, which could be up to 100 mV in amplitude. The most common method for reducing hum is to implement a differential amplifier that rejects any common signal between the two data streams recorded in di-electrode EMG. Since hum is present for both electrodes, it is rejected by the differential amplifier. A measure to calculate the differential amplifier's capability to reject the common signal is termed common-mode rejection ratio (CMRR). An expression of CMRR is presented in Equation (55), where A_d is the differential gain and $|A_c|$ the absolute common mode gain. It is recommended to have a CMRR of more than 80 dB for EMG devices [72].

$$CMRR = 20 \, log \left(\frac{A_d}{|A_c|} \right) dB \hspace{3cm} \text{Eq. (55)}$$

Once a high-quality, amplified EMG signal is acquired, the raw EMG data can be processed. This is required as the raw EMG signal has a high-frequency content (up to 1,000 Hz), which is difficult to visualize and relate to other biomechanical measures (e.g., body movement or joint torques). EMG processing involves some or all the following steps [72]:

➢ removal of DC bias
➢ full-wave or half-wave rectification
➢ filtering
➢ normalization
➢ more advanced processing (e.g., principal component analysis)

The EMG signal acquired after amplification may have a DC bias that is present due to instrumental error or constant voltage shifts. Removal of this DC component is essential for further processing of the signal and for correlating the signal with other biomechanical measures. Additional filtering can be performed to remove the influences of the heart rate and/or the power

line. Oftentimes, the signal is also full-wave, or half-wave rectified, such that the absolute value of the signal is taken [222], [223].

A full wave rectified EMG signal will have the same absolute value as the original signal, and the mean of the signal will correspond to the average activity of the muscle. Thus, to capture the time-varying activity of the muscle, an envelope of the signal is acquired. To obtain this envelope, a low-pass Butterworth filter with a cut-off frequency within the range of 2 to 10 Hz has oftentimes been employed [8], [22], [34], [206], [207], [224]–[226]. There are other time domain methods, for example, root mean square, mean absolute value, zero crossings, and integrated EMG that have been used to smooth the signal [64]. Sometimes the frequency information in EMG is of interest and, thus, parameters like mean frequency, median frequency, and wavelet coefficients are also computed. The choice of smoothening technique depends on the EMG features to be extracted [227].

If there is a need to compare EMG signals from one muscle to the other or from one individual to the other, EMG signals need to be normalized [228]–[230]. The normalization process scales the muscle activity as a percentage of a reference value. EMG normalization in the literature is oftentimes performed by using maximal voluntary contractions (MVC) of individual muscles, where the participants perform an exercise that produces a target muscle's maximum effort in a muscle [205], [228], [231], [232]. Along with MVC, baseline signals for all muscles in consideration are recorded when the participant is lying comfortably on a bed or mat, with all the muscles in a relaxed state. With these recordings, the normalized EMG can be calculated according to Equation (56) [210], [233]:

$$EMG_{normalized} = \frac{EMG - baseline}{MVC - baseline} * 100\% \qquad \text{Eq. (56)}$$

MVC are recorded by performing a set of exercises that are common among some of the muscles [229]. To produce a maximum effort, it may be required to provide a resistive force against the exercising motion. This external force can be provided either manually or by using a device such as a dynamometer [234]–[236]. The process of normalization has one major limitation: impaired individuals may not be able to produce maximum contractions for muscles affected by impairment [230], [232], [237]. Therefore, EMG results obtained from non-disabled individuals cannot be directly compared with those from impaired individuals.

Scientists have employed another normalization technique known as sub-maximal voluntary contractions (sub-MVC), where participants produce sub-maximal muscle activity or a percentage of maximum activity [228], [231], [232], [238]. This technique is employed when a participant is not able to produce maximum effort in the target muscles [230], [232], [237], when acquiring MVCs from a muscle is anatomically not possible [222], or when low levels of muscle activity need to be detected [204], [231], [239]. This sub-MVC is then used to calculate the normalized EMG, using the same technique as for the MVC (Equation (56)), but with the MVC value being replaced by the sub-MVC value. However, maintaining an equivalent sub-maximal load across participants and muscles is a difficult process [228].

Some studies normalize EMG signals by computing the standard deviation of the EMG time series across all trials and all participants. The EMG time series is then divided by the standard deviation to obtain normalized EMG signals [8], [22], [34]. This approach does not include specific exercises used in the MVC or sub-MVC approach. However, since the standard deviation is affected by the instrument type used, the placement of electrodes, the preparation of the skin, and the muscles in consideration [72], this approach provides some form of normalization as well.

Normalized EMG signals from several muscles are often combined to produce one weighted EMG signal [8], [22], [34]. Past perturbation studies have recorded the muscle activity from up to seven different muscles, where posterior muscles were given positive weights and anterior muscles negative weights [34]. The weights were then optimized, with the goal of maximizing the coherence between the weighted EMG and an external disturbance [34]. This signal was further used in system identification to estimate the mechanisms of seated and standing balance [8], [22], [34].

3.6.4 Neuromusculoskeletal modelling

In the literature, researchers have tried to quantify the muscular dynamics to make predictions about joint torques produced by muscles [8], [26], [34], [240], [241]. Such information is useful to develop rehabilitation devices, which can assist affected individuals in ADL [16], [240], [242]–[245]. Muscular dynamics are divided into three components: (i) *Muscle activation dynamics*; (ii) *Muscle contraction dynamics*; and (iii) *Musculoskeletal dynamics* [241].

Human skeletal muscle can be thought of as a mechanical actuator that also acts as a low-pass filter. This is due to the calcium dynamics in muscle, the transmission of muscle action potentials

requiring a finite amount of time, and the viscoelasticity of muscle and tendon [241]. EMG is a measure of the electrical signal flowing through the muscle fiber causing it to activate. The electrical activity measured by an EMG signal produces a chain of chemical reactions in the muscle, causing the muscle to produce a force by contraction [241]. The process of converting an EMG signal into muscle activation is termed muscle activation dynamics and can be modelled by first order, linear differential equation as shown in Equation (57) [246]:

$$e(t) = \tau_{act} \frac{da(t)}{dt} + [\beta + (1 - \beta)e(t)]a(t) \qquad \text{Eq. (57)}$$

Here, $e(t)$ is the processed EMG signal, $a(t)$ is the muscle activation, τ_{act} is the time constant, and β is a constant between 0 and 1. The muscle activation and the derivative of muscle activation appear in Equation (57) on the right hand side; thus, it needs to be solved using numerical integration, for example, via the Runge-Kutta algorithm. Another model of the same dynamics uses a second order, critically damped difference equation as shown in Equation (58) [247], where M, B, and K are constants and can be identified experimentally for the muscles in consideration:

$$a(t) = M \frac{de(t)^2}{dt^2} + B \frac{de(t)}{dt} + Ke(t) \qquad \text{Eq. (58)}$$

It has been reported that $a(t)$, when calculated via the above equation, may not be an accurate representation of muscle activation as it is non-linearly related to EMG [248]–[250]. Equation (59) includes the non-linearity present at lower muscle activation levels, and the linear relationship present at higher activation levels, where $d, c, b,$ and m are constants. This form of activation has been validated [251] and related to the size principle of motor unit recruitment [72].

$$a(t) = d \ln(ce(t) + 1) \qquad 0 \le e(t) < 0.3$$

$$a(t) = me(t) + b \qquad 0.3 \le e(t) \le 1 \qquad \text{Eq. (59)}$$

Another study has proposed Equation (60), which includes the non-linear characteristics of muscle activation, where A is a constant [252], [253]:

$$a(t) = \frac{e^{Ae(t)} - 1}{e^A - 1}, \qquad \text{Eq. (60)}$$

Once activated the muscle will contract and produce a force. This process is known as muscle contraction dynamics. The most common model that represents the muscle contraction dynamics

is the Hill-Type model [254]. The muscle-tendon arrangement can be modelled with viscoelastic tendons, and with a muscle fiber represented by an elastic component parallel to the contractile element (sarcomere). The Hill-Type model provides a model for the contractile element and can be represented by Equation (61), where $F(t)$ is the time-varying muscle fiber force, $f_v(t)$ is the normalized time-varying velocity-dependent fiber force, $f_l(t)$ is the normalized time-varying length-dependent fiber force, f_o is the maximum isometric muscle fiber force, and $a(t)$ is the muscle activation signal [241]:

$$F(t) = f_v(t) * f_l(t) * f_o * a(t) \qquad \text{Eq. (61)}$$

Tendon dynamics are similar to elastic rubber band dynamics, such that they have a slack length below which there will be no pulling force. Above that, the force varies with length. It has been reported that a maximal load produced by the muscle causes 3.3 % of tendon strain and that the tendon fails at 10% strain [246]. Tendon dynamics can be modelled by Equation (62), where T_t is the tension produced in the tendon and s is the slack length:

$$T_t = 0 \qquad\qquad s \leq 0$$

$$T_t = 1480.3s^2 \qquad 0 < s < 0.0127$$

$$T_t = 37.5s - 0.2375 \qquad s \geq 0.0127 \qquad \text{Eq. (62)}$$

The moment arm of the muscles needs to be known to compute the joint torques. However, both the moment arm and length of a muscle change with the joint angles [255], [256]. Therefore, musculoskeletal dynamics consider the change in moment arms and the joint angle. More complex models exist that include the geometry of the bones and the joint kinematics to determine changes in moment arms [257]. The moment arm was modelled as a function of muscle length and joint angle by An et al. (1984) using Equation (63), where $r(\theta)$ is the moment arm and $l(\theta)$ is the length of muscle as a function of joint angle θ [258]:

$$r(\theta) = \frac{\partial l(\theta)}{\partial \theta} \qquad \text{Eq. (63)}$$

However, this is a simplified approximation of the actual process. The muscle paths are complex: muscles cannot be approximated by a straight line as they often twist around bones, and the joints

oftentimes do not act as simple hinges [241]. Considering these factors would result in a highly sophisticated model that is computationally expensive to implement.

3.6.5   Identification of Muscular Dynamics using System Identification

Researchers have modelled the muscular dynamics using the system identification approach, where they apply a sensory disturbance and measure the neuromusculoskeletal time series (such as body sway, joint torques, and/or weighted EMG) as a response to a perturbation. They implemented the indirect (*see Section 2.3.2*) and/or the joint input-output approach (*see Section 2.3.3*) to estimate the muscular dynamics [8], [34]. The model for the muscular dynamics as estimated in these studies is presented in Equation (64), where H_{act} are the muscular dynamics in the Laplace domain, β is the damping coefficient, ω is the natural frequency, f is the frequency, and s is the Laplace variable.

$$H_{act} = \frac{\omega^2}{(s^2 + 2\beta\omega s + \omega^2)}, \omega = 2\pi f \qquad \text{Eq. (64)}$$

3.7   Mechanical Dynamics

As mentioned previously (*see Section 3.3*), the human body consists of skeletal, muscular, integumentary, and other organ systems (for example, respiratory and digestive systems). These systems are made up of tissues and gases (for example, oxygen and carbon dioxide in the lungs), with each of them having specific inertial and elastic properties, also known as intrinsic properties of the material. The intrinsic properties of a substance will resist the motion of the body when subjected to an external force and/or moment. The body's ability to resist an external disturbance due to intrinsic properties of its materials (bones, tissues, and intra-abdominal pressures) is termed mechanical dynamics [8], [17], [20]–[22], [26], [34], [35].

The human skeleton alone is not able to maintain an upright posture under the influence of gravity [72], [105]. It requires constant support from the muscles to maintain its structure. The musculo-tendon structure (*see Section 3.6.4*) can be modelled as a spring-damping system. Thus, even if the muscles were not activated, the physical properties of muscle would resist, but not prevent the body's movement away from the upright position. In that sense, physical stretching of the ES, as well as abdominal pressure, will resist the body's movement in the anterior direction. For posterior movements, stretching of the RA will resist the body's movement [72], [105].

In the literature, researchers have consistently modelled the mechanical dynamics of the upper body via a mass-spring-damper system [8], [17], [21], [22], [38], [259]. In one study, external perturbations were applied from eight different directions to obtain estimates of the mechanical dynamics in both the frontal and sagittal planes [148]. Mechanical dynamics can also be estimated using system identification, where physical or sensory perturbations are applied, and neuromusculoskeletal time series are measured. Using the indirect approach and joint input-output approach, non-parametric estimates of the mechanical dynamics are obtained, which are then further converted into parametric form via a first order differential equation (representing, essentially, a mass-spring-damper system) [8], [17], [22], [259].

3.8   Sensorimotor Time Delay

The process of transmitting the information from sensory systems to the CNS, processing the information in the CNS, transmitting the processed information to the periphery (e.g., muscles), and generating a response in the periphery (e.g., muscles), involves a time delay. Three types of time delays are mentioned in the literature, i.e., a feedback time delay, motor command time delay, and electromechanical time delay. The feedback time delay is the delay caused by the transmission of information from the sensory systems to the CNS. The motor command time delay is the delay caused by the processing of information in the CNS and transmitting the information to the muscles to produce a response. The electromechanical time delay is the delay caused by the muscles effort to produce a force and, ultimately, joint torque as a response to the electrical signals from the CNS [26]. The mathematical model to represent a time delay in the Laplace domain is mentioned in Equation (65), where TD is the time delay in seconds.

$$H_{TD} = e^{-TDs} \qquad \text{Eq. (65)}$$

3.9   Feedback Control Models of Human Balance in Sitting and Standing

System identification is a powerful mathematical tool that can be used to predict the characteristics of a system based on experimental input-output data. A control model of the given system is required to apply system identification techniques. In the literature, researchers have proposed models of seated and standing balance [8], [17], [20], [21], [26], [34], [38], [150], [189], [259],

[260]. All models follow one general framework: The plant represents the human body dynamics of standing or seated balance. The feedback branch considers the sensory dynamics. The controller encompasses an active controller that consists of neural dynamics, muscular dynamics, a sensorimotor time delay, and a passive controller that consists of mechanical dynamics. The output of the model is the body's orientation in space, measured via human motion tracking devices. The input is the joint torque measured via force transducers. In addition, some studies also consider muscle activity measured via EMG systems.

Audu et al. (2015) have modelled the seated balance as shown in Figure 3-7. They have modelled the body dynamics, or trunk dynamics, with a single-link inverted pendulum, with the mass situated at the COM location. The output is the trunk angle relative to the vertical direction. The input to the plant is the combined torque generated from the active and passive controller [17]. The active controller (neural dynamics) is modelled using a PID controller followed by a long latency time delay (sensorimotor time delay). The passive controller (mechanical dynamics) is modelled via a PD controller, with the differential term followed by a small latency time delay. The reference value is set to be the nominal trunk angle, which in this case reflects stable, upright sitting. The feedback is assumed to be unity [17].
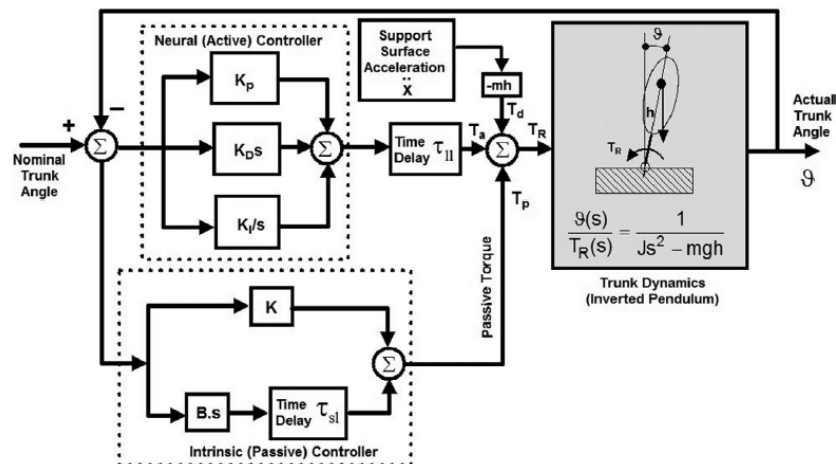
Figure 3-7: Closed-loop control model of human seated balance as described in [17]. This model consists of a plant modelled as a single-link inverted pendulum; the active controller dynamics modelled as a proportional-integrative-derivative controller; and the passive controller dynamics modelled as a proportional-derivative controller. The feedback dynamics equal one.

Masani et al. (2003) have implemented a closed-loop control model for standing balance as shown in Figure 3-8. Similar to the control model for seated balance mentioned above, the standing balance control model has a plant modelled as a single-link inverted pendulum. The controller is modelled as a PD controller with a reference set to zero degrees. The output measured is the body sway in the A-P direction, and the input to the plant is the joint torque produced by the PD controller as well as Gaussian noise. Two separate time delays are considered in this model, one in the feedback branch (feedback time delay), and another one as part of the neuromuscular dynamics (neuro-mechanical delay). The reference is selected as zero degrees from the vertical [38].
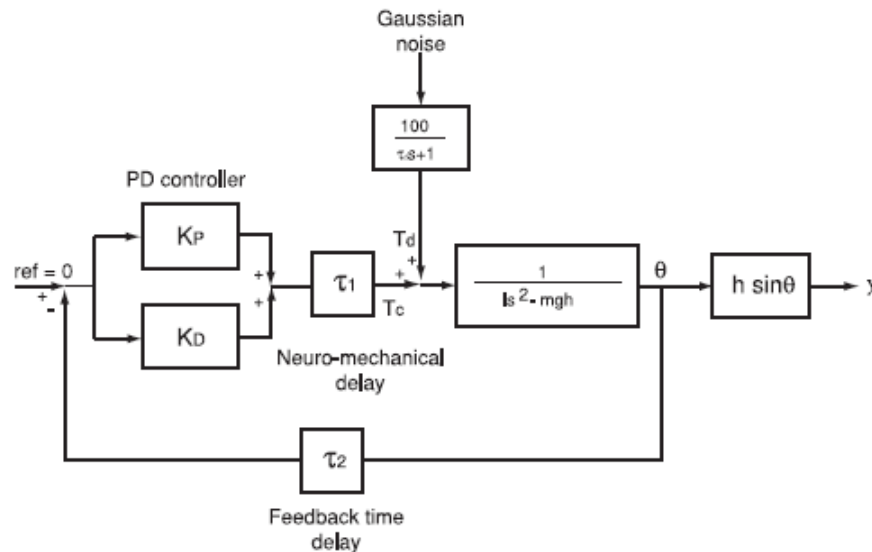
Figure 3-8: Closed-loop control model of human standing balance as described in [38]. This model consists of a plant, modelled as a single-link inverted pendulum; neural controller dynamics modelled as a proportional-derivative controller; and a sensorimotor time delay divided into a feedback time delay and a neuro-mechanical delay. The feedback dynamics equal one.

Vette et al. (2010) have described a standing balance control model as shown in Figure 3-9. The plant depicts the single-link inverted pendulum that produces body sway as an output. The output is fed back to the active controller (neural dynamics) and passive controller (mechanical dynamics). Both the active and passive controllers are modelled using a PD equation. A second-

order critically damped system represents the neuromusculoskeletal dynamics (muscular dynamics). There are three separate time delays considered: a feedback time delay, motor command time delay, and electromechanical delay (together called sensorimotor time delay) [26].
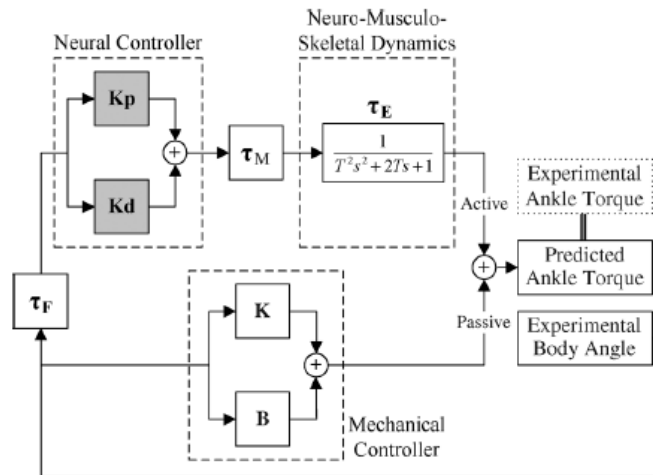
Figure 3-9: Closed-loop control model of human standing balance as described in [26]. This model consists of a plant modelled as a single-link inverted pendulum; neural controller dynamics and mechanical controller dynamics modelled as proportional-derivative controllers; and sensorimotor time delays divided into a feedback time delay, a motor command time delay, and an electromechanical time delay. The feedback dynamics equal one.

Pasma et al. (2014) have represented standing balance as a two-link inverted pendulum as shown in Figure 3-10. This model includes both the sensory and physical perturbations, and the biomechanical and electrophysiological responses that can be measured. For sensory perturbations, each sensory system can be perturbed via a separate mechanism. The visual system can be perturbed using the movement of the screen, the vestibular system can be perturbed using galvanic stimulation, and the proprioceptive system can be perturbed by rotating the base of support. Physical perturbations can be applied via two external pushes, one at the trunk level and one at the level of the lower segments. Two independent perturbations are required to separately identify the control mechanisms for both segments [33]. The biomechanical response measured can be the body sway using motion tracking and/or the ground reaction forces using force

transducers. The muscle activity can be measured using EMG. From the obtained data, one can estimate the characteristics of human body dynamics, the sensory systems, the active controller, the passive controller, the muscular dynamics, and the sensorimotor time delay using system identification techniques (Section 2.3). This method applies to identify the mechanisms of seated balance [261].
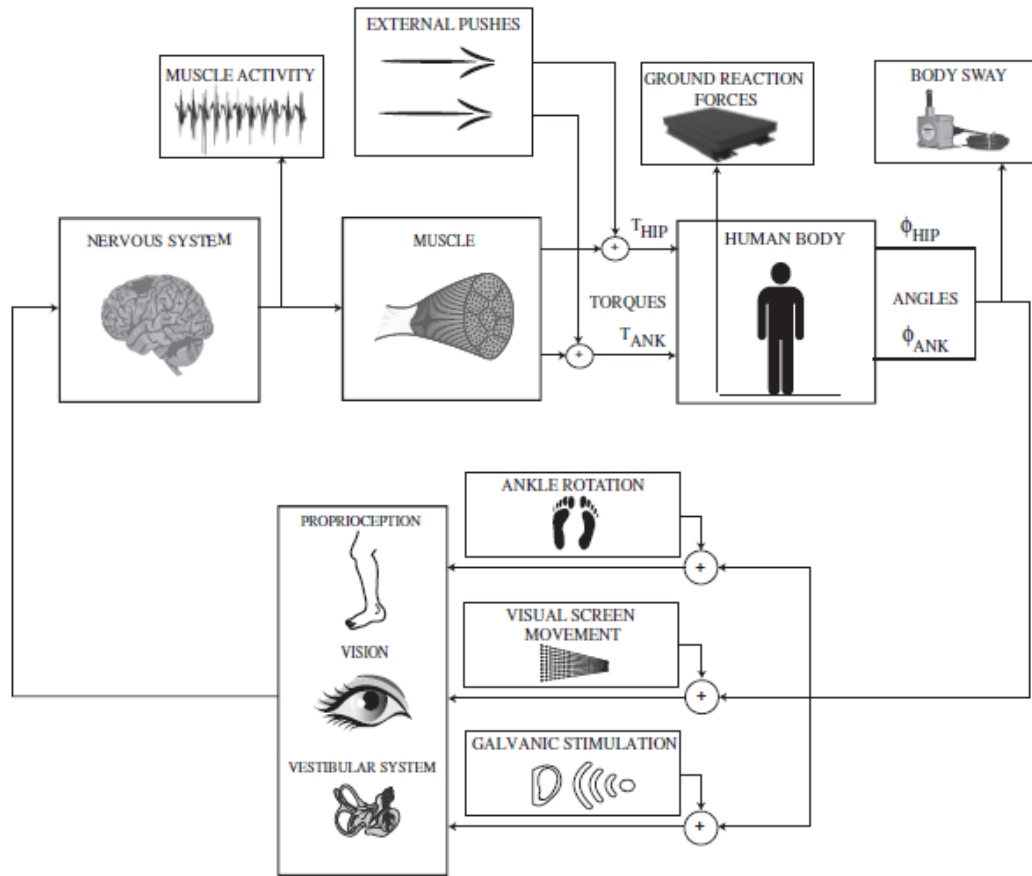
Figure 3-10: Closed-loop control model of human standing balance as described in [261]. This model provides a general framework for identifying the mechanisms of standing balance. To obtain estimates of the plant, controller and feedback branch, it is required to apply either sensory and/or physical perturbations. Sensory perturbations can be applied using the movement of the visual screen, galvanic stimulation, or a rotation of the base of support to affect the visual, vestibular, or proprioceptive systems, respectively. Physical perturbations can be applied by applying an external force. The response of these perturbations is estimated by recording body sway, ground reaction forces, and muscle activity.

Pasma et al. (2017) have implemented the model presented in Figure 3-11. It includes a plant, modelled as a single-link inverted pendulum. In this study, a sensory disturbance in the form of a rotation of the base of support is applied. Therefore, the proprioceptive feedback is isolated from other sensory systems (vision and vestibular system). The neural dynamics are modelled as a PD with acceleration feedback controller, and the mechanical dynamics are modelled as a PD controller. The sensorimotor time delay is considered as a single, lumped time delay. The activation dynamics (muscular dynamics) are modelled using a second-order, critically damped system. Force feedback is also considered in the model, providing information about muscle tension to the brain. The force feedback is modelled via a first order, low-pass filter [8].
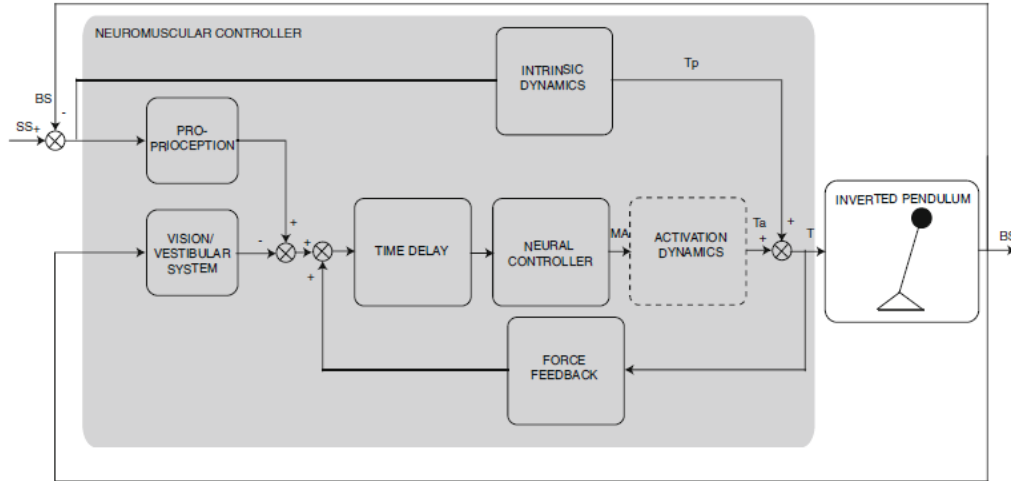
Figure 3-11: Closed-loop control model of human standing balance as described in [8]. This model consists of the plant modelled as a single-link inverted pendulum, proprioceptive feedback isolated from the others, an active controller, a time delay, and activation dynamics. A mechanical controller reflecting the mechanical dynamics is also included in the model. Force feedback is added to include the effect of the Golgi-tendon organ.

Peterka et al. (2002) have utilized the model presented in Figure 3-12 to accurately identify the individual weights of each of the sensory systems in standing balance. The plant is considered as a single-link inverted pendulum, the active controller is modelled as a PID controller, and the

passive controller as a PD controller. A time delay added to the neural controller encompasses the sensorimotor delays in the active control branch [21].
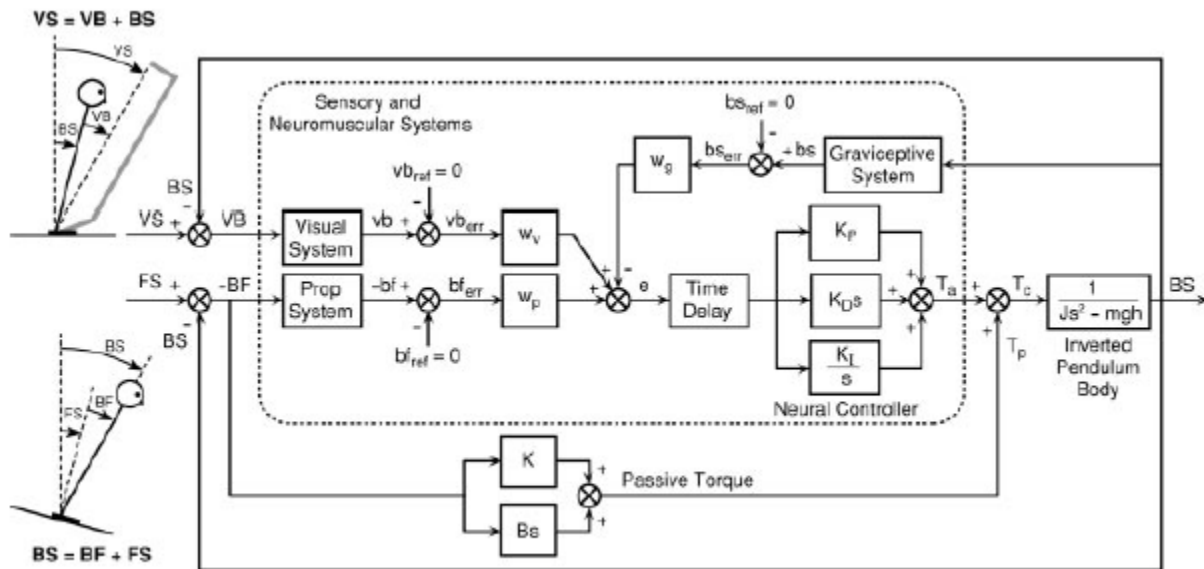
Figure 3-12: Closed-loop control model of human standing balance as described in [21]. This model consists of a plant modelled as a single-link inverted pendulum, feedback weights for individual sensory systems, neural dynamics and mechanical dynamics modelled as proportional-integrative-derivative and proportional-derivative controllers, respectively, and a time delay.

The models described above provide a consensus among researchers regarding the modelling of human balance. These models are, to a great extent, applicable to seated balance as well. As mentioned previously, human seated balance involves sensory systems to sense the body's orientation in space, a neural controller to integrate sensory information and provide motor commands to the muscles, and muscles to generate stabilizing joint torques. Thus, a human seated balance control model can be developed similarly to the ones described in this section.

4 Materials and Methods

4.1 Overview

This chapter focuses on the materials and methods implemented in this study. It includes the details of the participants, the feedback control model of human seated balance, the experimental setup and recordings, the experimental protocol, data cleaning and parameter extraction, and the experimental data analysis employed to estimate the mechanisms of seated balance. The estimated parameters of the mechanisms of seated balance were finally verified with a simulation analysis.

4.2 Participants

Fourteen male individuals participated in this study (mean age (standard deviation, SD): 24 (4) years; mean height (SD): 178 (7) cm; and mean weight (SD) 76 (11) kg). Using self-reporting via a health screening form (Appendix I), the participants reported that they did not have any history of neurological or musculoskeletal impairments or any significant injuries or disorders that may have affected their seated balance capabilities. Written consent regarding their participation in the study was provided before the start of the experiment (Appendix II). The experimental protocols were approved by the University of Alberta Health Research Ethics Board (Study ID: Pro00063998).

4.3 Feedback Control Model of Human Seated Balance

System identification is a tool used to identify the characteristics of a system based on the system's inputs and outputs (*see Section 2*). Human seated balance can be modelled as a closed-loop feedback system that can be subjected to system identification techniques. A common feedback control model of human seated balance is presented in

Figure 4-1. Human body dynamics represent the plant (P) of the closed-loop system, where the input is the joint torque (τ) about an axis of rotation at the fifth lumbar vertebra in the medio-lateral (M-L) direction, and the output is body sway (θ) in the anterior-posterior (A-P) direction. Tissue stiffness, tissue damping, and intra-abdominal pressure are captured in the mechanical

dynamics (C_P) for which the input and output are body sway and passive joint torque, respectively. The information obtained by the sensory systems and its transmission to the brain are captured in the sensory dynamics. The central nervous system (CNS) is modelled as neural dynamics (C_A), where sensory data is integrated and interpreted to generate an appropriate motor command (MC). The muscular response to the motor command and the generation of a corrective, active joint torque are modelled as muscular dynamics (H_{act}). The process of transmitting the information from the sensory systems to the CNS, processing the information in the CNS, transmitting the processed information to the periphery (e.g., muscles), and generating a response in the periphery (e.g., muscles), involves a time delay which is modelled as a sensorimotor time delay (H_{TD}). The body's intention to have a particular orientation of the head-arms-trunk (HAT) segment in the A-P direction is modelled as the set point. The external perturbation (d_{ext}) required for applying certain system identification techniques to the feedback control model is added to the input of the plant.
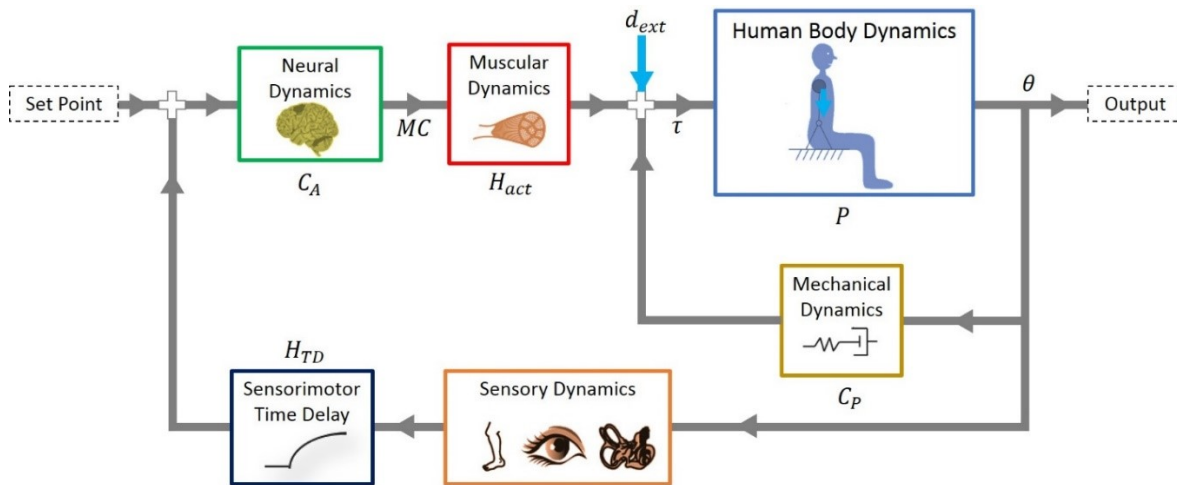
Figure 4-1: Feedback control model of human seated balance (adapted from [1]). Human body dynamics represent the plant (P), sensory dynamics the feedback, and neural dynamics (C_A) the central nervous system controller of the closed-loop system. The mechanical dynamics (C_P) capture the passive control components, and the muscular dynamics (H_{act}) capture the muscular response to the motor command (MC). The time delay due to transmitting and integrating information is modelled as the sensorimotor time delay (H_{TD}). The plant's input (τ) is the joint

torque, and the plant's output (θ) is body sway. The set point is the intent of the control task. d_{ext} is the external perturbation.

4.4   Experimental Setup and Recordings

In order to acquire the data needed for performing the system identification, each participant was asked to sit on a customized stool and maintain seated balance during quiet sitting and in the presence of external perturbations. This setup was realized using the Computer-Assisted Rehabilitation Environment (CAREN; Motekforce link, Amsterdam, The Netherlands). When applying the surface perturbations via motion of the CAREN platform on which each participant was sitting, the kinematics, muscle activity, and kinetics of the human body were measured.

Kinematics were obtained using a 12-camera (T020) motion capture system (Vicon Motion Systems Ltd., Oxford, UK) and the Nexus 2.3 software (Vicon Motion Systems Ltd.) at a sampling rate of 100 Hz. The sampling rate for the motion capture system was chosen based on the motion in consideration and in agreement with similar, previous studies [8], [20], [22], [72]. Based on the manufacturer's specifications, the mean error (SD) in the position of the markers as captured by the motion capture system was 1 mm (1 mm). The capture volume of the motion capture system was 3.40 m (x-direction; M-L) × 3.20 m (y-direction; A-P) × 2.70 m (z-direction; vertical). The camera locations and the motion capture coordinate system are shown in Figure 4-2.
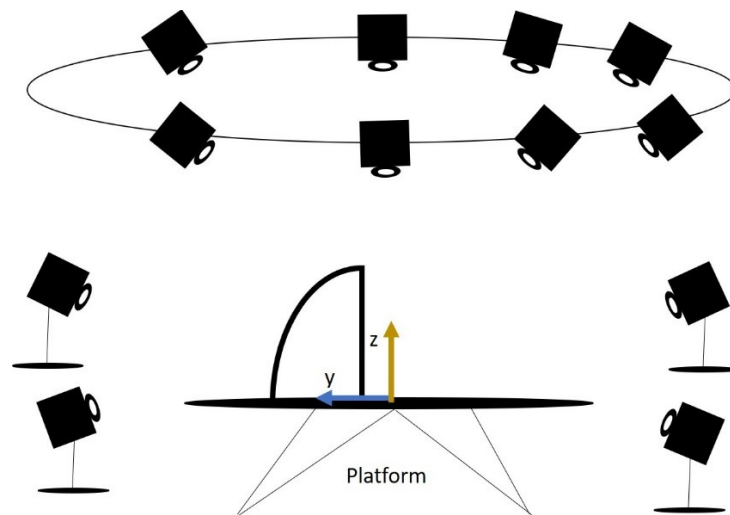
Figure 4-2: 12-camera motion capture system, installed within the Computer-Assisted Rehabilitation Environment.

Muscle activity was recorded using a 16-channel Bagnoli[TM] Electromyography (EMG) system (Delsys Inc., Natick, MA, USA) as presented in Figure 4-4, at a sampling rate of 2,000 Hz. Previous studies have reported that the meaningful EMG content is below 1,000 Hz. Hence, EMG data should be acquired at a minimum of 2,000 Hz [8], [22], [227]. The EMG system had one main amplifier and two input modules. Each input module had nine inputs to collect data from eight surface EMG sensors and one reference electrode. The input modules were connected with each other using an intermodule cable. The input modules were connected to the main amplifier with an input module cable. The surface EMG sensors (Delsys Inc.) had an inter-electrode gap of 1 cm. The baseline noise of the EMG system was in the range of 5 to 10 μV peak-to-peak. The applied signal gain was muscle- and participant-dependent (varying from 100 to 10,000) and was removed later in the data processing. The common-mode rejection ratio (Equation (55)) of the EMG system was -92 dB, and the input impedance of the electrodes was 10^{15} Ω and 0.2 p.
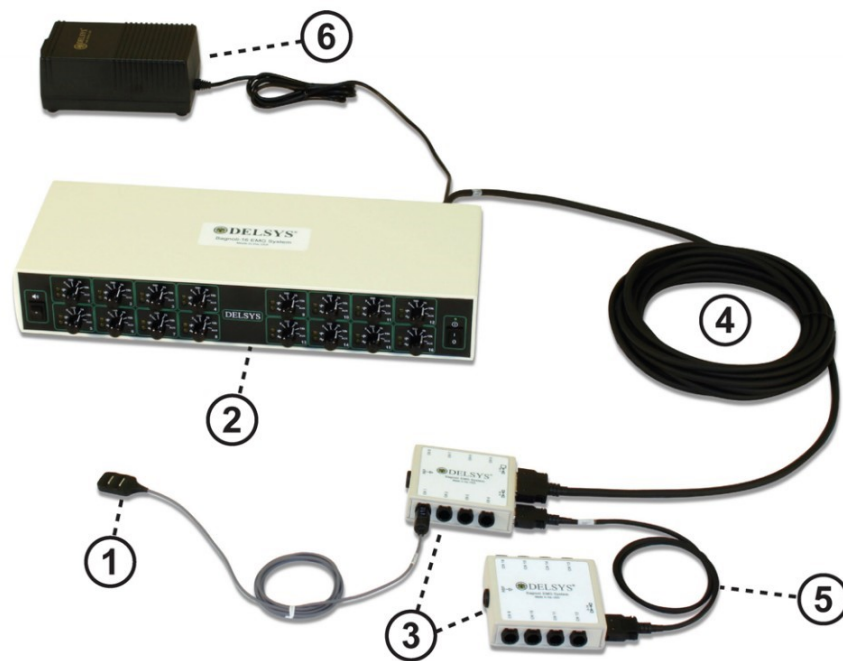
Figure 4-3: Electromyography (EMG) system. (1) Surface EMG electrodes; (2) main amplifier; (3) input modules; (4) input module cable; (5) intermodule cable; and (6) power supply. {Image source: Figure 1. Bagnoli[TM] EMG system user's guide 2014, Delsys Inc.}

The kinetics were obtained using a force plate (Advanced Mechanical Technology Inc., Watertown, MA, USA) as presented in Figure 4-4A, at a sampling rate of 2,000 Hz. The force plate data has meaningful frequencies of up to 500 Hz. Hence, the recommended sampling rate for the force plate was 1,000 Hz [72]. However, due to the integration of the EMG system and force plate into one system for synchronization purposes, we have acquired data from both systems at 2,000 Hz. The force plate signals, which were amplified with a Gen-5 Amplifier (Advanced Mechanical Technology Inc.), captured the ground reaction forces, F_x, F_y and F_z, and the moments, M_x, M_y and M_z, for three orthogonal axes. Measurements were also used to obtain the center of pressure (COP) fluctuation in the A-P and M-L directions. A manual calibration of the force plate was performed to test the accuracy of the force plate data as mentioned in Appendix III. The F_z component had an accuracy of ±1.31% relative to the applied load, the COP A-P component of ±1.18 mm, and the COP M-L component of ±2.36 mm relative to the actual location. The dimensions of the force plate were 464 mm × 508 mm × 82.5 mm. Data were recorded in 'fully-conditioned mode', for which the platform's calibration matrix was applied to the signal. In addition, the voltage drop along the length of wire was accounted for and the gains and excitation voltages determined from the amplifier calibration were used. The force plate was mounted on a customized stool as shown in Figure 4-4A. The force plate's front edge was placed perpendicular to the A-P direction of the platform. It was also assured that the force plate was at the center of the platform by measuring the distance (L) of the stool's legs from the edges of the red strips marked on the platform (Figure 4-4B).

All the three data streams acquired from the motion capture system, the EMG system, and the force plate were time synchronized using the lockbox (Vicon Motion Systems Ltd.) as shown in Figure 4-5A. The force plate and EMG outputs were connected to the lockbox with the BNC cables and connector box seen in Figure 4-5B.
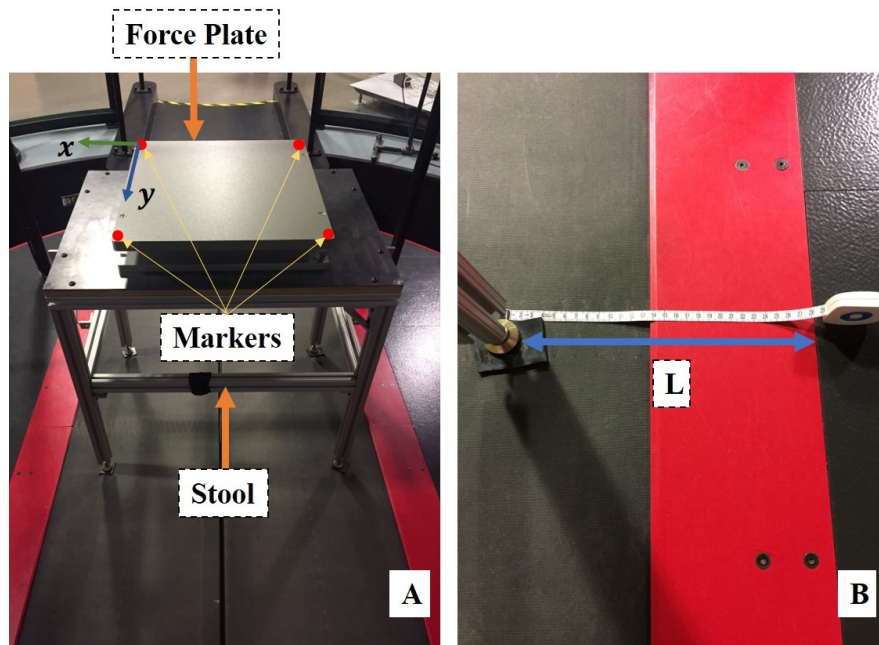
Figure 4-4: Force plate setup. (A) The force plate was mounted on top of the stool; (B) the stool was placed at a fixed distance L from the red markings. There were four markers placed on the force plate to assess potential movement of the force plate and stool relative to the Computer-Assisted Rehabilitation Environment platform and to define a local coordinate system.
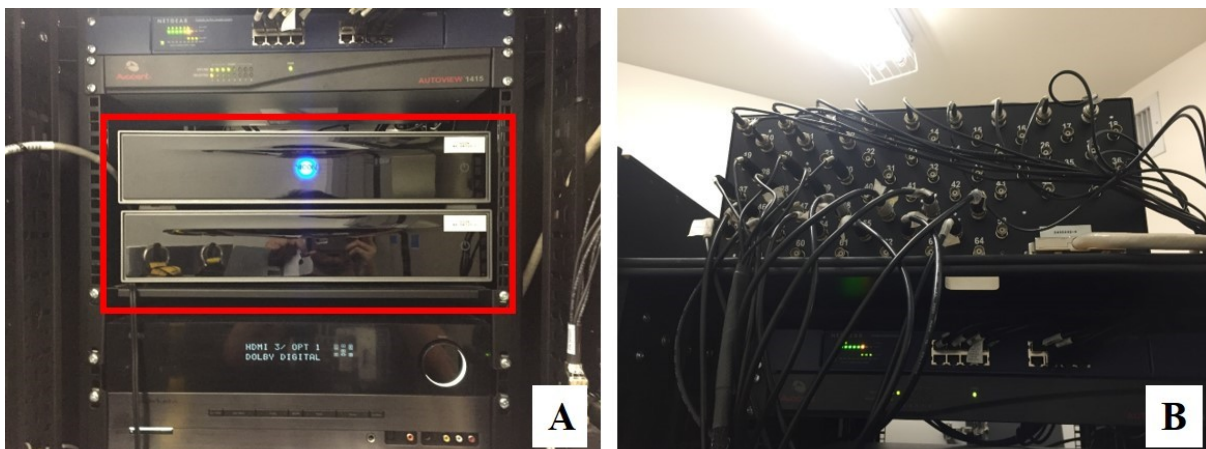
Figure 4-5: Lockbox setup. (A) Lockbox highlighted in red; (B) BNC box after connecting it with the analog outputs of the force plate and electromyography system using BNC cables.

The external perturbations were applied using the robotic platform of the CAREN. It has six hydraulic actuators connected in a Stewart configuration that allows motion for six degrees of freedom: three linear translations (x, y, and z) and three rotations (roll, pitch, and yaw) as shown in Figure 4-6. It also features a treadmill embedded in the platform and an 180° curved projection screen in front, for the purpose of altering the visual environment of the users. The projections on the screen were applied by four F-10 AS3D projectors (Barco, Fredrikstad, Norway). The perturbations to the participants were applied by moving the platform in the y-direction (refer to Figure 4-6). White two-dimensional (2D) grid lines on a black background were projected onto the virtual-reality screen [21], [22]. The CAREN facility lights were turned off during the experiment to allow for the visuals on the screen to be more effective. The platform was controlled by the D-flow 3.24.0 software (Motekforce link). A start trigger, sent by D-flow to the lockbox, time synchronized the CAREN signals (perturbation command and visual scene) with the other systems (motion capture system, EMG system, and force plate).
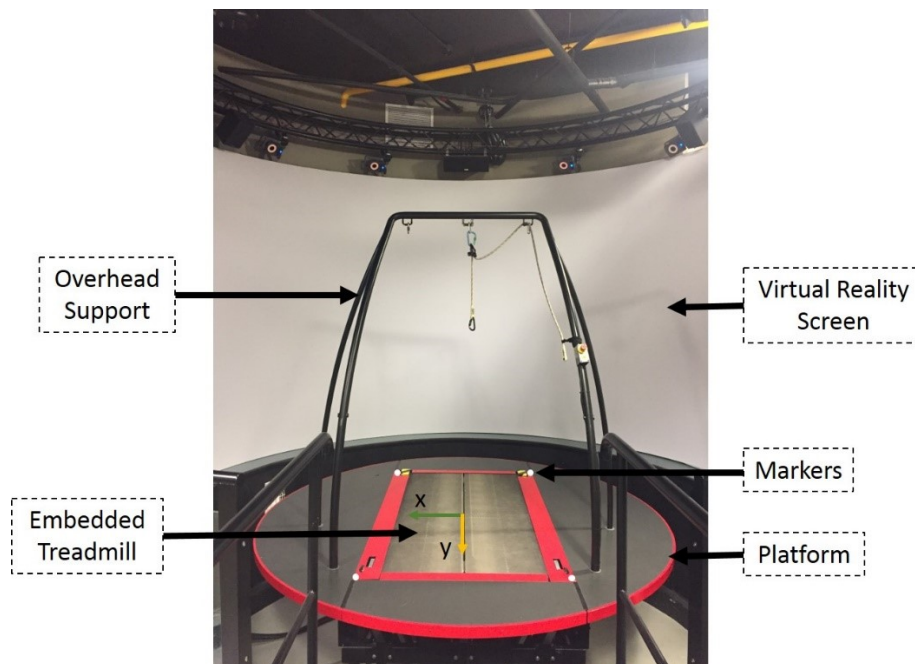
Figure 4-6: Computer-Assisted Rehabilitation Environment (CAREN). The CAREN includes a virtual-reality screen as well as a treadmill embedded in the platform. It also features a overhead support system to which a safety harness can be attached. There were four markers placed on the platform to record the platform motion by the motion capture system.

61

The external perturbation signal used to move the CAREN platform had characteristics of filtered white noise. The unfiltered white noise had a mean power spectral density of 4 cm²/Hz and a sampling rate of 200 Hz. The unfiltered white noise was filtered using a 1st order high-pass Butterworth filter with a cut-off frequency of 0.1 Hz, and an 8th order low-pass Butterworth filter with a cut-off frequency of 5 Hz. The first and the last 5 s of the 240 s perturbations had no platform motion. For the signal periods of 5 to 10 s and 230 to 235 s, the perturbation signal was multiplied with an increasing and decreasing ramp function, respectively, avoiding an abrupt beginning and end of the perturbations [22]. Only the middle 220 s were analyzed for each trial.

4.5 Experimental Protocol

As stated earlier, the study was performed in the CAREN, which is housed in the Glenrose Rehabilitation Hospital, Edmonton, Alberta, Canada. The motion capture system is already pre-installed and, hence, core component of the CAREN. Before each experiment, the EMG system and the force plate were connected with the motion capture system through the previously mentioned lockbox, using BNC cables (Figure 4-5B).
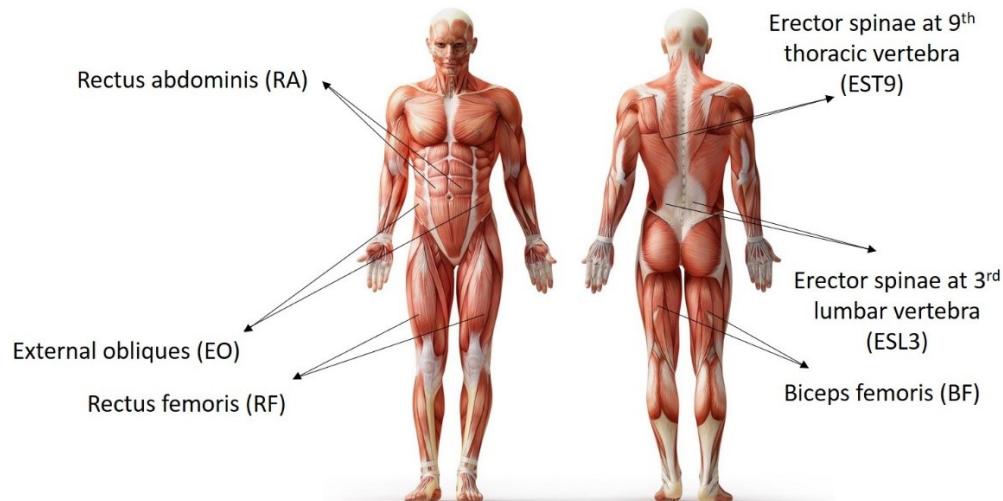
Figure 4-7: Placement of the electromyography electrodes on the human body. The electrodes were placed over the rectus abdominis, the external obliques, the rectus femoris, the erector spinae at the ninth thoracic vertebra, the erector spinae at the third lumbar vertebra, and the biceps femoris. {Image Source: istock photo}

4.5.1 Health Screening and Anthropometric Parameters

The participants reported their body height, body weight, age, and any existing medical conditions (if any) on a Health Screening form (Appendix I). The medical conditions were used to determine the eligibility of a participant to perform the experiment. The body weight was used further to calculate other biomechanical parameters specific to the participant.

4.5.2 EMG Electrode Placement and Maximum Voluntary Contractions

Once all the hardware connections were established, we identified and marked the placement sites of the EMG electrodes and the motion capture system's markers on the participants. The muscles where EMG electrodes were placed are shown in Figure 4-7. The electrodes were placed bilaterally on the muscles. The anatomical location within each muscle over which the EMG electrodes were placed and the orientation of each electrode on each muscle are presented in Table 4-1.

Once the locations for electrode placement were identified, the next step was to clean the skin. Cleaning involved shaving (if the target location had hair) and removing dead cells using alcohol wipes. After cleaning, the electrodes were placed on the skin using 2-bar sensor adhesive interfaces (Delsys Inc.). Skin sensitive tape (3M Transpore^{TM}) was used to secure the electrodes during the experiment. In addition, a self-adhesive reference electrode (Dermatrode, Delsys Inc.) was placed over the right iliac crest. All electrodes, including the reference electrode, were connected to one of the two input modules (worn by the participants).

Following electrode placement, participants were asked to lie down in a relaxed position on a mattress facing upwards, with their eyes closed and the body kept still. This position was used to measure the baseline EMG in a relaxed state for 60 seconds (Figure 4-8).

Figure 4-8: The relaxed state of the participant in which the baseline of electromyography was collected for the different muscles.

Table 4-1. The electromyography electrodes placement sites for different muscles and the direction of the electrode on each muscle.

Muscle	Anatomical location	Direction of electrode	References
Rectus Abdominis (RA)	3 cm lateral of the umbilicus	Vertically downwards	[202], [205]–[207], [262]
External Obliques (EO)	15 cm lateral of the umbilicus	45° from the vertically downward, in the direction of muscle fiber	[202], [206], [207], [262]
Thoracic Erector Spinae (EST9)	5 cm lateral of the ninth thoracic vertebra	Vertically downwards	[202], [204], [207], [262]
Lumbar Erector Spinae (ESL3)	3 cm lateral of the third lumbar vertebra	Vertically downwards	[202], [205], [207], [262]–[264]
Rectus Femoris (RF)	Mid-point of the imaginary line between the anterior superior iliac spine and the superior part of the patella	Vertically downwards	[265]–[269]
Biceps Femoris (BF)	Mid-point of the imaginary line between the ischial tuberosity and the lateral condyle of the tibia	Vertically downwards	[267]–[269]

The next step was for the participant to perform maximum voluntary contractions (MVC) exercises. Each exercise was carried out for 30 s, with a resting time of 30 s in between exercises [270]. Each exercise was performed three consecutive times to account for learning effects and statistical errors [210]. The muscle activity was monitored during the exercise to ensure the highest quality of the signal. The instructions for each exercise were given by the author of this thesis, and the help of the assistant was only used for static bracing. The exercises for individual muscles are

as described below and as shown in Figure 4-9. Note that all participants were instructed to exert their maximum effort in the direction of motion as specified in the individual exercises.

➢ Rectus Abdominis – seated abdomen crunch (Figure 4-9A). The participant's torso was at an angle of 45º with respect to the base of support. The legs and knees were flexed at 45º, and both the hands were at the back of the head. The participant's legs were braced by an assistant to avoid any movement of the legs. The torso was held by another assistant to resist the effort made by the participant in crunching upward [271]–[275].

➢ External Obliques – side crunch (Figure 4-9B). Similar to the rectus abdominis position, the participant's torso was at an angle of 45º with respect to the base of support, the legs and knees were flexed at 45º, and both the hands were at the back of the head. The participant's legs were braced by an assistant to avoid any movement of the legs, and the torso was held by another assistant to resist the twist motion. In the twist motion, the participant had to touch the right (left) knee with the left (right) elbow to rotate the upper body with a twisting motion and maximum effort [272], [273], [276].

➢ Thoracic and Lumbar Erector Spinae – supine back extension (Figure 4-9C). The participant was lying down on the mattress, with the front of the body facing the mattress and both arms extended forward, without touching the ground or body. The participant's legs were braced by an assistant to avoid any movement of the legs. The torso was held by another assistant at the inferior border of the scapula to resist the effort exerted by the participant to extend himself upwards [271], [274], [275], [277].

➢ Biceps Femoris – prone knee flexion (Figure 4-9D). The participant was lying down, with the front of the body facing the mattress. The participant's lower leg was held by an assistant at an angle of 90º with respect to the base of support, while the participant was instructed to extend the knee joint with maximum effort [278].

➢ Rectus Femoris – seated knee extension (Figure 4-9E). The participant was sitting on a chair with both feet on the ground and both arms on the armrest of the chair. One leg at a time, the participant's leg was held by an assistant. The participant exerted maximum effort to extend his leg as the assistant resisted the motion [278].
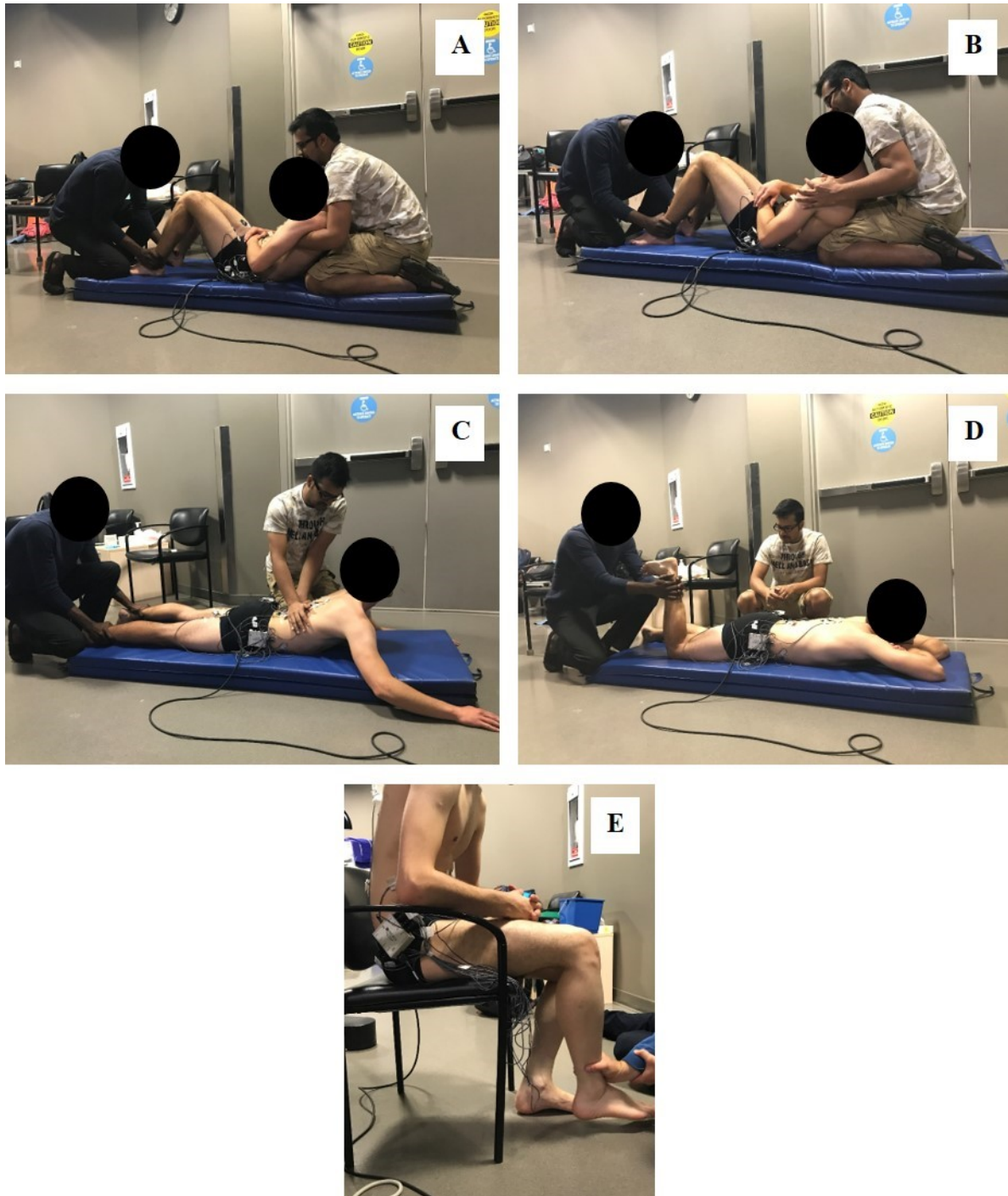
Figure 4-9: Exercises for the different muscles to obtain the maximum voluntary contractions. (A) Seated abdomen crunch; (B) Side crunch; (C) Supine back extension; (D) Prone knee flexion; and (E) Seated Knee Extension.

4.5.3 Motion Capture Marker Placement

After performing MVC, the next step was to place thirty-seven motion capture markers (Vicon Motion Systems Ltd.) on anatomical landmarks of the body as shown in Figure 4-10. The marker placement sites were based on past studies [279] and Vicon preparation guidelines (Vicon Motion Systems Ltd.). The markers were attached to the skin using double-sided adhesive tape and plastic marker bases (Vicon Motion Systems Ltd.). The markers were placed bi-symmetrically on the human body as described in Table 4-2.
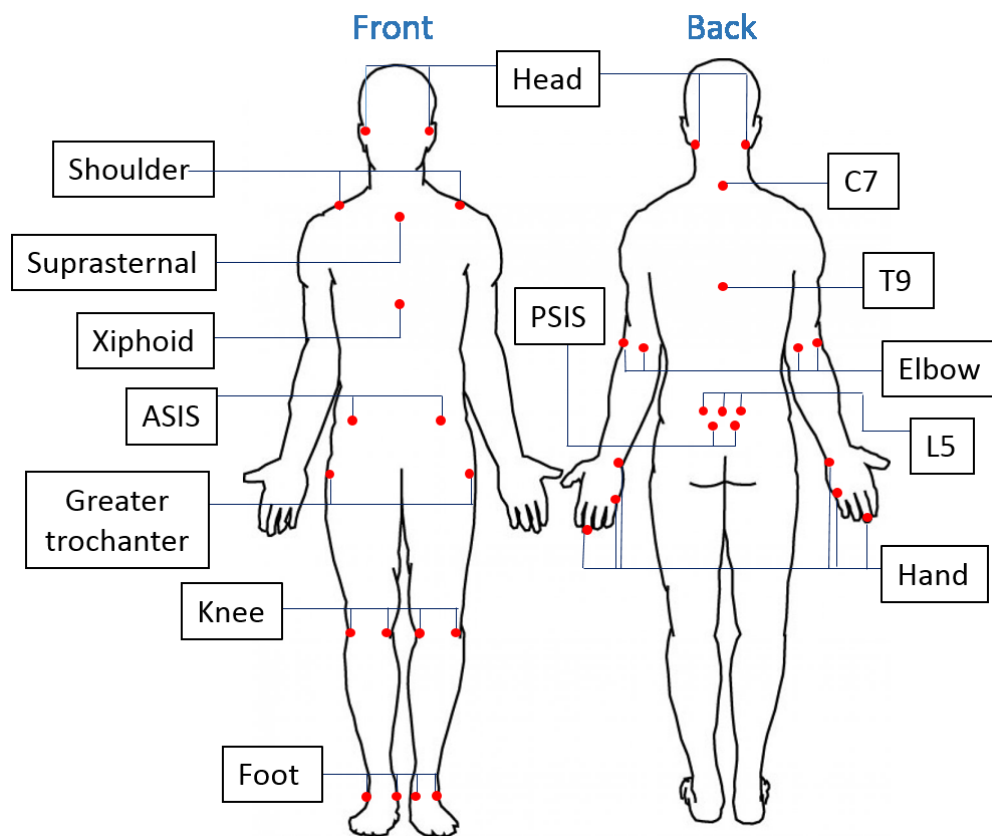
Figure 4-10: Placement of the motion capture markers on the anatomical landmarks of the body. Markers were placed on the head, arms, trunk, and leg segment. C7: seventh cervical vertebra; T9: ninth thoracic vertebra; L5: fifth lumbar vertebra; ASIS: anterior superior iliac spine; and PSIS: posterior superior iliac spine. {Image Source: body pictures}

Table 4-2. List of markers placed on anatomical landmarks of the human body, including their lateral position and label.

Body Segment	Anatomical Location	Lateral Position	Label
Head	Condyloid process	Left	LFHD
	Condyloid process	Right	RFHD
	Mastoid process	Left	LBHD
	Mastoid process	Right	RBHD
Trunk	Shoulder (acromion)	Left	LSHO
	Shoulder (acromion)	Right	RSHO
	Seventh cervical vertebra	Center	C7
	Suprasternal	Center	SUP
	Xiphoid	Center	XIP
	Ninth thoracic vertebra	Center	T9
	Fifth lumbar vertebra	Left (5 cm)	LL5
	Fifth lumbar vertebra	Center	L5
	Fifth lumbar vertebra	Right (5 cm)	RL5
	Anterior superior iliac spine	Left	LASIS
	Anterior superior iliac spine	Right	RASIS
	Posterior superior iliac spine	Left	LPSIS
	Posterior superior iliac spine	Right	RPSIS
Arms	Elbow (lateral epicondylitis)	Left	LLELB
	Elbow (lateral epicondylitis)	Right	RLELB
	Elbow (olecranon)	Left	LMELB
	Elbow (olecranon)	Right	RMELB
	Distal ulna bone	Left	LDUB
	Distal ulna bone	Right	RDUB
	Little finger, metacarpal head	Left	LPFMH
	Little finger, metacarpal head	Right	RPFMH
	Middle finger, distal phalanges	Left	LMFDP
	Middle finger, distal phalanges	Right	RMFDP
Legs	Greater trochanter	Left	LGTR

Greater trochanter	Right	RGTR
Knee (lateral epicondylitis)	Left	LLKNE
Knee (lateral epicondylitis)	Right	RLKNE
Knee (medial epicondylitis)	Left	LMKNE
Knee (medial epicondylitis)	Right	RMKNE
Ankle (lateral malleolus)	Left	LLANK
Ankle (lateral malleolus)	Right	RLANK
Ankle (medial malleolus)	Left	LMANK
Ankle (medial malleolus)	Right	RMANK

The markers were also placed on the force plate and the CAREN platform as defined in Table 4-3 (Figure 4-4A and Figure 4-6).

Table 4-3. List of the markers placed on top of the force plate and the Computer-Assisted Rehabilitation Environment platform.

Instrument	Relative position	Label
Force Plate	Left-Forward	LFFP
	Left-Backward	LBFP
	Right-Forward	RFFP
	Right-Backward	RBFP
Platform	Left-Forward	LFP
	Left-Backward	LBP
	Right-Forward	RFP
	Right-Backward	RBP

4.5.4   Anatomical Calibration

After placing the markers, participants were asked to stand on the CAREN platform in a T-pose while facing the CAREN's virtual reality screen for anatomical calibration (Figure 4-11A). The anatomical calibration was performed to capture the relative positions of the markers on the body, to reconstruct any markers that were occluded during an experimental trial, to develop template models in the Nexus software, and to label markers automatically across trials and participants. Following calibration, participants were asked to wear a safety harness to ensure safety in case of any malfunctioning of the CAREN platform. The safety harness was secured to the platform via the overhead support system as shown in Figure 4-11B.
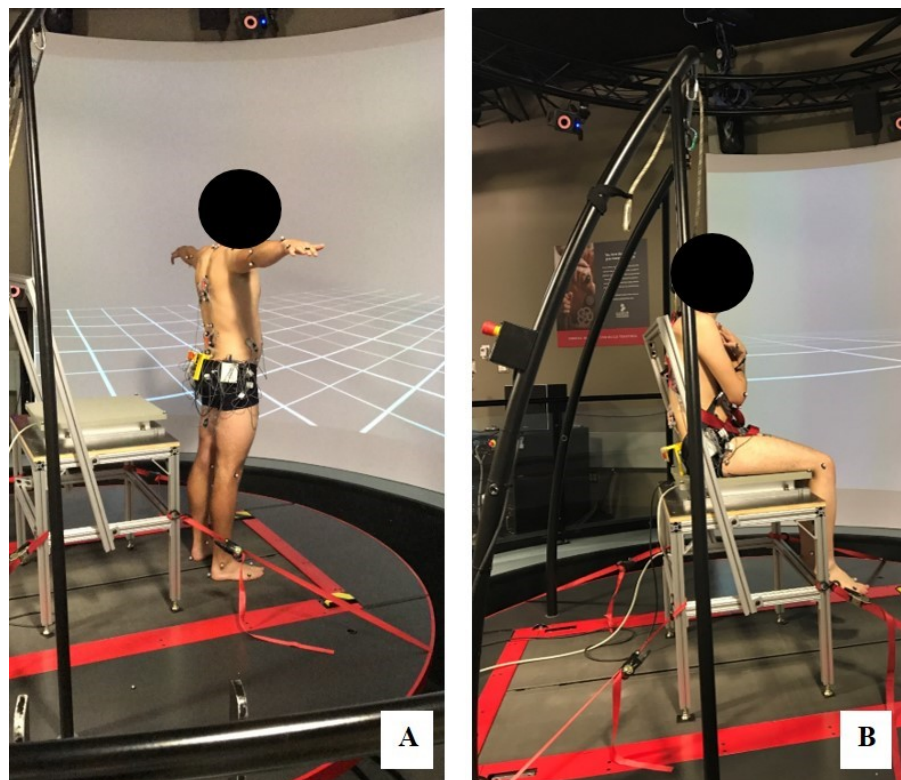
Figure 4-11: Anatomical calibration and human posture during the experimental trials. (A) T-pose; and (B) Crossed arms, legs hanging, eyes open, and spine completely erect.

4.5.5 Quiet Sitting Trial

The participants were asked to sit on top of the customized force plate, with their arms crossed above the chest, the legs hanging in the air without touching the base of support or stool, the eyes open, and the spine completely erect (Figure 4-11B). Each participant was asked to maintain balance for 120 seconds. A 1-minute break for resting was given at the end of the trial. This trial was used to compare the neuromusculoskeletal time series obtained during quiet sitting and perturbed sitting. A significant difference between the two would confirm the applicability of the system identification techniques in this study.

4.5.6 Perturbed Sitting Trial

In this trial, the participants had to sit on the customized force plate with their arms crossed above the chest, the legs hanging in the air without touching the base of support or stool, the eyes open and looking straight onto the virtual reality screen, and the spine completely erect (Figure 4-11B). Platform perturbations were applied in the A-P direction for 240 s as described earlier. Each participant was asked to maintain balance for the whole trial. A total of three trials were performed, with external perturbations that had statistically independent signal characteristics (while still fulfilling the signal characteristics described above). The same three perturbation signals were used across all participants. A one-minute gap was administered between trials, allowing the participant to recover.

4.6 Experimental Data Cleaning and Neuromusculoskeletal Time Series Extraction

The Nexus 2.6 software was used for experimental data acquisition and preliminary data cleaning. MATLAB R2017a (MathWorks, Natick, MA, USA) was used for further data cleaning and neuromusculoskeletal time series extraction.

4.6.1 EMG Data

The EMG data, including MVC data, baseline data, quiet sitting data, and perturbed sitting data were first exported to a Microsoft Excel file from the Nexus 2.6 software. They were then imported into MATLAB as distinct MATLAB variables using MATLAB R2017a.

MVC data for each muscle were divided by gain, converted from Volts to mV, demeaned, rectified, filtered using a 4th order Butterworth filter with a cut-off frequency of 5 Hz, and down-sampled to 100 Hz [72]. The maximum value of the three filtered MVC trials for each exercise was selected

as the MVC value for a particular muscle of that participant [210]. The baseline trial for each muscle was divided by gain, converted from Volts to mV, demeaned, rectified, filtered using a 4th order Butterworth filter with a cut-off frequency of 5 Hz, and down-sampled to 100 Hz (same as for the MVC data) [72]. The mean value of the filtered baseline trial was selected as the baseline value for a particular muscle of a given participant [210]. The MVC and EMG baseline values for all 12 muscles and 14 participants were calculated based on the described approach. The MVC and EMG baselines values were then compared between the left and right muscles to assess the similarity between body sides using the Wilcoxon signed rank test.

The EMG data obtained during the quiet and perturbation sitting trials were divided by gain, converted from Volts to mV, demeaned, rectified, filtered using a 4th order Butterworth filter with a cut-off frequency of 5 Hz, and down-sampled to 100 Hz. The EMG signal was normalized using the MVC and baseline values for each muscle according to Equation (56) [210].

After cleaning the EMG data from the perturbation trials, the data sets from different muscles were used to obtain the neuromusculoskeletal time series called "weighted EMG". The weighted EMG can represent the motor command mentioned earlier and is a time series of combined muscle activity obtained by applying weights to the activity time series for individual muscles. The process of obtaining the weighted EMG is captured in Equation (66) [8], [22], where $w1$ to $w12$ are the weights, $RA, EO, RF, ESL3, EST9,$ and BF are the activity time series of individual muscles, and R is the coefficient corresponding to right muscles and L is the coefficient corresponding to left muscles.

$$EMG = w1 * RRA + w2 * REO + w3 * RRF + w4 * RESL3 + w5 * REST9 + w6 * RBF \dots$$
$$\dots + w7 * LRA + w8 * LEO + w9 * LRF + w10 * LESL3 + w11 * LEST9 + w12 * LB$$

Eq. (66)

The muscles of the front of the body, i.e., rectus abdominis, external obliques, and rectus femoris, were given negative weights, whereas the muscles of the back of the body, i.e., erector spinae at third lumbar vertebra, erector spinae at ninth thoracic vertebra, and biceps femoris, were given positive weights. The absolute sum of all the weights was maintained at one. The weights were optimized by maximizing the mean squared coherence between the weighted EMG and the external perturbation signal. The mean squared coherence between the two time series (a, b) was

calculated using Equation (67), where $P_{aa}(\omega)$ and $P_{bb}(\omega)$ are the power spectral densities of time series a and b, respectively.

$$|C_{ab}(\omega)|^2 = \left|\frac{|P_{ab}(\omega)|^2}{P_{aa}(\omega)P_{bb}(\omega)}\right|^2 \qquad \text{Eq. (67)}$$

The optimization was performed in MATLAB R2017a using the function *fmincon,* where a customized function is developed to calculate the mean squared coherence value between the weighted EMG signal and the external perturbation. The MATLAB function used to calculate the mean squared coherence is *mscohere*, where a Hanning window was chosen with 40 s window length, 50% overlap, and a frequency range of 0.3 to 5 Hz [22].

4.6.2   Motion Capture Data

The motion capture data was processed using Nexus 2.6 to label the markers, reconstruct missing marker locations, and export the data to Microsoft Excel. Note that labelling of markers could be done manually by labelling individual markers for each trial, or automatically by Nexus 2.6 when a pre-defined template of markers was provided. For this study, it was decided to label individual markers manually for each trial.

When a marker went missing during a trial (e.g., due to occlusion), it was reconstructed in Nexus 2.6 through either a spline fill or a rigid-body fill. In the spline fill, the gap was filled by performing a cubic spline interpolation operation, based on data points on either side of the gap. This method required sufficient data before and after the gap to accurately estimate the cubic spline. The spline fill was generally used when the gap size was small (typically less than ten missing points). In the rigid-body fill, if two markers were placed on a rigid body or semi-rigid-body segment and one of the markers went missing, the other marker on the segment could be used to reconstruct data for the missing marker. In our study, we used spline fill to reconstruct smaller gaps, and rigid-body fill to reconstruct larger gaps.

After the reconstruction of missing markers, motion capture data was exported to Microsoft Excel. The exported data contained the three-dimensional (3D) coordinates of each marker in the motion capture coordinate system. The Microsoft Excel data was then imported into MATLAB as distinct MATLAB variables.

The coordinate system (X, Y, Z) of the Vicon motion capture system is shown in Figure 4-6. The force plate had four markers placed on top that were used to define a local coordinate system (x, y, z) as shown in Figure 4-4A. Since a coordinate system could be defined using any of the three markers as mentioned in Section 3.3.2.2, we used markers LFFP, LBFP, and RBFP to define the local coordinate system. From this, we defined the positive x-axis to be pointing to the right of the participant when facing the virtual reality screen, the positive y-axis to be pointing in the anterior direction, and the positive z-axis to be pointing upwards. All other marker data were converted into the local coordinate system according to Equation (68), where x, y, z is the marker location in the local coordinate system; X, Y, Z is the marker location in the motion capture coordinate system; and P_1, P_2, P_3 is the distance vector from the motion capture coordinate system to the local coordinate system.

$$\begin{bmatrix} x \\ y \\ z \end{bmatrix} = \begin{bmatrix} -1 & 0 & 0 \\ 0 & -1 & 0 \\ 0 & 0 & 1 \end{bmatrix} * \begin{bmatrix} X \\ Y \\ Z \end{bmatrix} + \begin{bmatrix} P_1 \\ P_2 \\ P_3 \end{bmatrix} \qquad \text{Eq. (68)}$$

The motion capture data was used to measure the external perturbation time series, the 2D center of mass (COM) location, and the body sway as would be explained in the upcoming sections.

4.6.2.1 External Perturbation Time Series and Estimated Perturbation Torque

The four markers (LFFP, LBFP, RBFP, and RFFP) placed on top of the force plate were used to calculate the acceleration of the base of support, which in turn was used to quantify the external perturbation. Since the platform accelerated only in the y-direction (A-P direction), there was negligible change in position of the force plate markers in the z-direction (as defined in the local coordinate system). Thus, the z-component of all four markers was ignored in the subsequent analysis. The x- and y-components of the marker data were filtered using a 4th order Butterworth filter with a cut-off frequency of 5 Hz [72]. The x-component of the LFFP, LBFP, RFFP, and RBFP markers were compared to assess the force plate rotation about the z-axis. As mentioned in Section 4.4, it was assured that the front edge of the force plate was perpendicular to the forward direction of the platform. The force plate orientation obtained via motion capture data verified the experimental choice. Thus, also the x-component was ignored in the subsequent analysis. After removing the DC offset from the y-component of the LFFP, LBFP, RBFP, and RFFP markers, the mean of all four marker's y-component was taken to quantify the perturbation. These data were

double-differentiated using Equation (69), where p_{n+1} and v_{n+1} are the y-direction position and velocity of the base of support, respectively, at sample $n + 1$; p_{n-1} and v_{n-1} are the y-direction position and velocity of the base of support, respectively, at sample $n - 1$; v_n and a_n are the y-direction velocity and acceleration of the base of support, respectively, at sample n; and Δt is the sampling time period. Zeroes were added at the beginning and end of the velocity and acceleration vectors to ensure that the acceleration data had the same length as the position data.

$$v_n = \frac{p_{n+1} - p_{n-1}}{2\Delta t}$$

$$a_n = \frac{v_{n+1} - v_{n-1}}{2\Delta t} \qquad \text{Eq. (69)}$$

The human body was approximated as a single-link inverted pendulum when quantifying the effect of the external perturbations on the participants (Figure 3-4). The human body, due to its inertia, feels a sudden force acting opposite to the direction of acceleration of the base of support [280]. The external torque, which causes the human body to move in the A-P direction, is caused by the sudden force and can be calculated using Equation (70). In Equation (70), d_{ext} is the torque experienced by the human body due to the acceleration of the base of support; m_{com} is the mass of the HAT segment; a is the acceleration of the base of support; l_{com} is the distance between the COM location and the axis of rotation; and θ is the body sway. The torque was used as the external perturbation for further analysis.

$$d_{ext} = -m_{com} a l_{com} \cos\theta \qquad \text{Eq. (70)}$$

4.6.2.2 Calculation of COM Location and of Other Biomechanical Parameters

The markers placed on the HAT segment were used to calculate the COM location of the HAT segment. The relevant markers' 3D data were filtered using a 4th order Butterworth filter with a cut-off frequency of 5 Hz [72]. Since the external perturbation was applied in the y-direction, there was minimal human motion in the x-direction. Therefore, the COM location was obtained in the y- and z-directions only.

The y- and z-direction components of the COM of the head were obtained from the mid-point of the line joining the LFHD and RFHD markers. The COM of the upper arm segment was obtained as 40.59% of the straight-line distance between the elbow (lateral epicondylitis) marker and the shoulder (acromion) marker. Similarly, the COM location for the lower arm segment was obtained

as 54.26% of the straight-line distance between the distal ulna bone marker and the elbow (lateral epicondylitis) marker. The z-direction COM location of the trunk segment was obtained as 51.12% of the straight-line distance between the seventh cervical vertebra marker and mid-point of the line joining the RGTR and LGTR markers. The y-direction COM of the trunk segment was calculated as the mid-point between the y-direction component of the T9 marker and the y-direction component of the XIP marker. The COM locations of the HAT segment in the y- and z-directions were then obtained through Equation (71), where COM_y and COM_z are the y- and z-direction components of the HAT segment COM, respectively; $\hat{y}$ and $\hat{z}$ are the y- and z-direction components of a given segment's COM respectively; H and T stand for the head and trunk segments, respectively; LUA, RUA, LLA and RLA stand for the left upper arm, right upper arm, left lower arm and right lower arm segments, respectively [72], [117].

$$COM_y = \frac{0.0694(\hat{y}_H)+0.4346(\hat{y}_T)+0.0271(\hat{y}_{LUA})+0.0271(\hat{y}_{RUA})+0.0162(\hat{y}_{LLA}) +0.0162(\hat{y}_{RLA})}{0.5711}$$

$$COM_z = \frac{0.0694(\hat{z}_H)+0.4346(\hat{z}_T)+0.0271(\hat{z}_{LUA})+0.0271(\hat{z}_{RUA})+0.0162(\hat{z}_{LLA}) +0.0162(\hat{z}_{RLA})}{0.5711} \quad \text{Eq. (71)}$$

The self-reported weight of the participants was used to estimate the mass of the upper body (m_{COM}) for each participant based on Equation (72).

$$m_{COM} = 0.603 * weight \qquad \text{Eq. (72)}$$

The length of the COM (L_{COM}) for each participant was calculated using the COM location in the y- and z-direction, and the position of the L5 marker during the perturbed sitting trials as shown in Equation (73). Note that $L5_y$ and $L5_z$ are the positions of the L5 marker in the y- and z-direction, respectively.

$$L_{COM} = \sqrt{\left(mean\,(COM_y) - mean(L5_y)\right)^2 + (mean(COM_z) - mean(L5_z))^2} \quad \text{Eq. (73)}$$

The mean z-direction distance between the base of support and the fifth lumbar vertebra (d_{L5}) for each participant was calculated using the L5, LFFP, LBFP, RFFP, and RBFP markers during the perturbed sitting trials as shown in Equation (74). Note that $L5_z$, $LFFP_z, LBFP_z, RFFP_z,$ and $RBFP_z$ are the positions of the L5, LFFP, LBFP, RFFP, and RBFP markers in the z-direction, respectively.

$$d_{L5} = mean\ (L5_z) - mean(LFFP_z, LBFP_z, RFFP_z, RBFP_z) \qquad \text{Eq. (74)}$$

The moment of inertia of the upper body (J) with respect to the axis of rotation fixed at the fifth lumbar vertebra was calculated, for each participant, using m_{COM} and L_{COM} and Equation (75) [117].

$$J = 1.6 * m_{COM} * L_{COM}^2 \qquad \text{Eq. (75)}$$

4.6.2.3 Body Sway

The 2D COM location of the HAT section could be identified for the quiet sitting trial and perturbation trials by following the procedure mentioned in Section 4.6.2.2. The line segment joining the L5 marker and the 2D COM position of the HAT segment forms an angle θ with respect to the positive z-axis (when the axis of rotation points to the left of the individual), as depicted in Figure 3-4. θ can be calculated as mentioned in Equation (76).

$$\theta = tan^{-1}\left(\frac{COM_z - L5_z}{COM_y - L5_y}\right) \qquad \text{Eq. (76)}$$

The mean value of the θ time series was subtracted from θ to obtain the body sway. The body sway angle was converted from degrees to radians. In addition to the weighted EMG, the body sway was another neuromusculoskeletal time series used to estimate the mechanisms of seated balance.

4.6.2.4 Joint Torque using Top-down Inverse Dynamics Approach

The body sway data were used to estimate the joint torque produced by the muscles to counter the effects of the external perturbation, gravity, and internal disturbances. The human body HAT segment could be modelled as the single-link inverted pendulum as mentioned in Section 3.3.3.1. This model was used to estimate the joint torque using a top-down inverse dynamics approach ("top-down joint torque") as described in Equation (77), where $\tau_{control}$ is the top-down joint torque, J is the moment of inertia of the upper body, and $\ddot{\theta}$ is the angular rate of change of body sway. The top-down joint torque was another neuromusculoskeletal time series used to estimate the mechanisms of seated balance.

$$\tau_{control} = J\ddot{\theta} - m_{com}gl_{com}sin\theta - m_{com}al_{com}cos\theta \qquad \text{Eq. (77)}$$

4.6.3 Force Plate Data

The force plate data were exported to Microsoft Excel in Nexus 2.6. The Microsoft Excel data were further imported into MATLAB using distinct MATLAB variables. The force plate data were converted from units of voltages to physical units by multiplying by 1,000 and dividing by the sensitivity matrix mentioned in Equation (78). The force plate data with physical units were filtered using a 4th order Butterworth filter with a cut-off frequency of 5 Hz [72]. The signal was then down-sampled to 100 Hz to compare it with the weighted EMG and the body sway data.

$$Sensitivity = [0.8992, 0.8992, 0.2248, 2.2127, 2.2127, 4.4254\,] \qquad \text{Eq. (78)}$$

The inertial effects due to the acceleration of the force plate were removed from the force plate data according to the method mentioned in Appendix IV. The lower body inertial effect was removed from the force plate data by normalizing the force plate data of a trial with the mean F_z component of force of that trial [155].

4.6.3.1 COP

As mentioned in Section 3.3.3.2, the COP can be obtained using Equations (49) and (50). The same technique was applied to obtain the COP for the HAT segment under the influence of the external perturbation. The coordinate system of the force plate is shown in Figure 4-12. The COP readings were converted from the force plate coordinate system to the local coordinate system as mentioned in Equation (79), where COP_x, COP_y, and COP_z are the COP components in the local coordinate system, COP_X, COP_Y, and COP_Z are the COP components in the force plate coordinate system, and Q_1, Q_2, and Q_3 are the components of the position vector from the force plate coordinate system to the local coordinate system.

$$\begin{bmatrix} COP_x \\ COP_y \\ COP_z \end{bmatrix} = \begin{bmatrix} -1 & 0 & 0 \\ 0 & 1 & 0 \\ 0 & 0 & -1 \end{bmatrix} * \begin{bmatrix} COP_X \\ COP_Y \\ COP_Z \end{bmatrix} + \begin{bmatrix} Q_1 \\ Q_2 \\ Q_3 \end{bmatrix} \qquad \text{Eq. (79)}$$
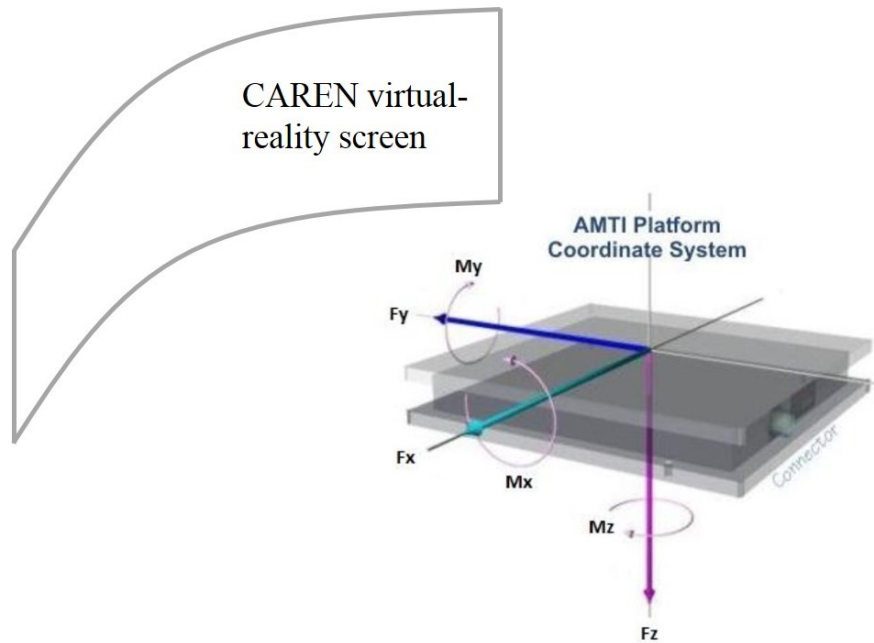
Figure 4-12: Force plate coordinate system. {Image source: AMTI Force Platform Manual_V4.3, Advanced Mechanical Technology, Inc., USA}

4.6.3.2 Joint Torque using Bottom-up Inverse Dynamics Approach

The joint torque using the bottom-up inverse dynamics approach ("bottom-up joint torque") was calculated using Equation (54). The torque was normalized by dividing the joint torque by the mean F_z component of the force of the trial and scaled by a factor of upper body mass multiplied by gravity. The bottom-up joint torque was another neuromusculoskeletal time series used to estimate the mechanisms of seated balance.

4.7   Experimental Data Analysis

The mean squared coherence ($|C_{ab}(\omega)|^2$) and the maximum normalized cross-correlation ($\bar{R}_{ab}(i)$) were calculated between the external perturbation and the neuromusculoskeletal time series, including the body sway, the weighted EMG, the top-down joint torque, and the bottom-up joint torque, to assess their relation. The normalized cross-correlation between the two time series (a, b) was calculated using Equation (80), where $R_{ab}(i)$ is the cross-correlation magnitude of two time series (a, b) at the ith time lag; E is the expected value; n is the sample number; $R_{aa}(0)$ is the

magnitude of the auto-correlation of time series a at 0 lag; and $R_{bb}(0)$ is the magnitude of the auto-correlation of time series b at 0 lag.

$$R_{ab}(i) = E\{a_{n+i}b_n^*\}$$

$$\bar{R}_{ab}(i) = \frac{R_{ab}(i)}{\sqrt{R_{aa}(0)*R_{bb}(0)}} \qquad \text{Eq. (80)}$$

The time lag between the external perturbation and the neuromusculoskeletal time series was used to verify the position of individual blocks in the implemented feedback control model. The time lag between the external perturbation and the body sway, and between the external perturbation and the weighted EMG time series were selected as the lag at which $\bar{R}_{ab}(i)$ was maximum. The time lag between the external perturbation and the top-down joint torque, and between the external perturbation and the bottom-up joint torque time series were selected as the lag at which $\bar{R}_{ab}(i)$ was minimum.

4.7.1   Non-Parametric Estimates

As mentioned in Section 2.3, to obtain the non-parametric estimates of the components of a closed-loop system, we could have applied either an indirect or a joint input-output approach. However, as mentioned in Section 2.3.2, the indirect approach requires the knowledge of the plant to obtain estimates of the controller, whereas the joint input-output approach did not require this. The joint input-output approach was therefore chosen and applied to obtain the estimates of the control mechanisms of seated balance.

The cross-spectral density ($P_{ab}(\omega)$) between two time series (a, b) can be calculated with Equation (81), where $R_{ab}(i)$ is the cross-correlation magnitude of two time series (a, b) at the ith time lag; and ω is the angular frequency. To smoothen the cross-spectral density estimates, Welch's averaged modified periodogram method of spectral estimation was applied [281].

$$P_{ab}(\omega) = \sum_{i=-\infty}^{\infty} R_{ab}(i)e^{-j\omega i} \qquad \text{Eq. (81)}$$

The ratio of the cross-spectral density between the weighted EMG signal and the external perturbation, as well as the cross-spectral density between the body sway and the external perturbation provided us with the estimates of active controller components (including the neural

dynamics and the sensorimotor time delay) as described in Equation (82), where CSD is the cross-spectral density function.

$$\frac{CSD(d_{ext}, weighted\ EMG)}{CSD(d_{ext}, \theta)} = -H_{TD}C_A \qquad \text{Eq. (82)}$$

Similarly, the ratio of the cross-spectral density between the joint torque and the external perturbation and the cross-spectral density between the body sway and the external perturbation provided us with the estimates of active-passive controller components (including the neural dynamics, the mechanical dynamics, the muscular dynamics and the sensorimotor time delay) as described in Equation (83).

$$\frac{CSD(d_{ext}, \tau)}{CSD(d_{ext}, \theta)} = -(C_P + H_{TD}C_A H_{act}) \qquad \text{Eq. (83)}$$

We calculated the cross-spectral density and complex coherence between two time series for all the participants using the MATLAB function *cpsd* and *mscohere*, respectively, with a Hanning window of length 40 s, 50% overlap, and a frequency range of 0.3 to 5 Hz at 100 different frequencies equally spaced on the logarithmic scale [22]. The bootstrap standard error in the estimates of active and active-passive controller components among all the participants was computed using the percentile-t method with 400 nested bootstrap resamples for variance estimation, and 4,000 bootstrap resamples [282].

4.7.2 Parametric Estimates

The parametric estimates of the neural dynamics, the mechanical dynamics, the muscular dynamics, and the sensorimotor time delay were obtained through model fitting, where different orders of linear transfer functions were fitted to the data in MATLAB. The optimization was performed using the function *fminsearch* that uses a simplex algorithm to compute the minimum of the cost function. This algorithm does not guarantee a global minimum; therefore, we used various combinations of initial values of the constants of the transfer function, with the aim to reach the global minimum. The optimization was also performed using the MATLAB function *ga* that uses a genetic algorithm to compute the minimum of the cost function. This algorithm guarantees the global minimum, and the results from the simplex algorithm were compared with it to guarantee that the identified parameters produce the best fit to the experimental data points.

The error minimized by the function is presented in Equation (84), where $y_{pre}(f)$ is the predicted value from the transfer function and $y_{act}(f)$ is the experimental value, both at frequency f.

$$Error = \frac{\sum_{i=1}^{N}(|gain(y_{pre}(f)-y_{act}(f))|)}{\sum_{i=1}^{N}(|gain(y_{pre}(f))|)} + \frac{\sum_{i=1}^{N}(|phase(y_{pre}(f)-y_{act}(f))|)}{\sum_{i=1}^{N}(|phase(y_{pre}(f))|)}$$ Eq. (84)

The selection of the transfer function was based on the Akaike information criteria (AIC) and the goodness-of-fit (GOF) as presented in Equations (85) and (86), where v is the number of variables in the transfer function, N is the number of data points used in the optimization, y_{pre} is the predicted value, y_{act} is the actual value obtained from the experiment, and f is the frequency [8], [30].

$$AIC = log(Error) + \frac{2v}{N}$$ Eq. (85)

$$GOf(\%) = \left[1 - \left(\frac{\sum_{i=1}^{N}|y_{pre}(f)-y_{act}(f)|}{\sum_{i=1}^{N}|y_{pre}(f)|}\right)\right]$$ Eq. (86)

Once an appropriate transfer function was selected for a mechanism (i.e., the neural dynamics, the mechanical dynamics, the muscular dynamics, and the sensorimotor time delay), the variance accounted for (VAF) between the experimental time series data $(y(t))$ and the predicted time series data $(\hat{y}(t))$ was computed, as stated in Equation (87). The experimental time series includes the top-down joint torque, the bottom-up joint torque, and the weighted EMG. The predicted time series were calculated from the estimated transfer functions of the active and active-passive control components and from the experimental body sway time series. The VAF computes the quality of the model in the time domain, such that, the higher the percentage of VAF, the better the quality of the estimated model.

$$VAF_{y(t),\hat{y}(t)} = \left(1 - \frac{var(y(t)-\hat{y}(t))}{var(y(t))}\right) * 100\%$$ Eq. (87)

4.7.3 Stability Analysis

The stability of the identified transfer functions was computed by calculating the zeroes of the characteristic equation (mentioned in Equation 88) of the closed-loop control model. A stable system is defined in the literature as a system where all the zeroes of the characteristic equation have negative real parts, i.e., the zeroes are on the left of the imaginary axis in the pole-zero plot [283].

$$Characterstic\ equation = 1 + P * (C_P + H_{TD}C_A H_{act}) \qquad \text{Eq. (88)}$$

4.8 Simulation Data Analysis

Lastly, we performed simulations in Simulink R2017a (MathWorks, Natick, MA, USA) to evaluate our findings in a closed-loop model (Figure 4-13). This model incorporated the estimated transfer functions of the neural dynamics, the mechanical dynamics, the muscular dynamics, the sensorimotor time delay, and the external perturbations. The human body dynamics were selected as the single-link inverted pendulum dynamics described in Equation (53). The parameters of the human body dynamics were selected based on the mean anthropometric measurements of the fourteen participants. The time series of the body sway, the joint torque, and the EMG were generated (at a 100 Hz sampling rate) as a response to the three statistically independent external perturbation time series used in the experiments (100 Hz sampling rate). The same joint input-output approach was implemented as employed for the experimental, non-parametric estimates to identify the non-parametric estimates of the active and active-passive controller components. The parametric estimates of the neural dynamics, the mechanical dynamics, the muscular dynamics and the sensorimotor time delay were obtained using the same optimization as for the experimental data. The experimental and simulated parameters were compared by calculating the mean relative difference (Equation (89)), where m_d is the mean relative difference, P_1 is the parameter calculated from the experimental data, and S_1 is the parameter calculated from simulated data [8], [26].

$$m_d = \left[\frac{P_1 - S_1}{S_1}\right] * 100\ \% \qquad \text{Eq. (89)}$$
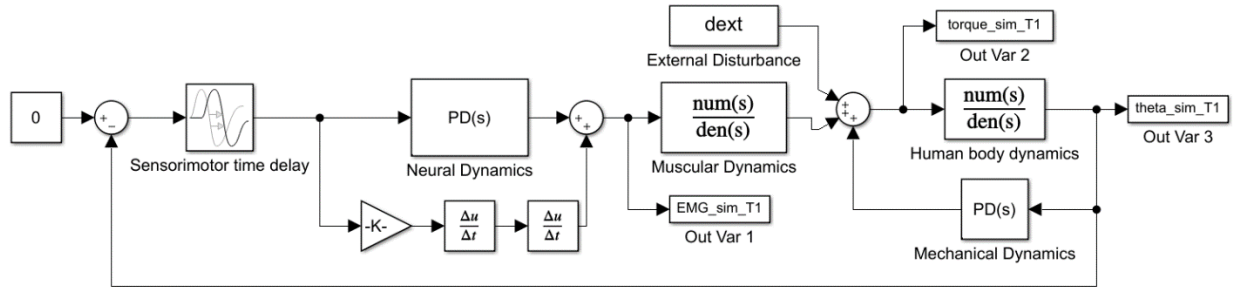
Figure 4-13: Closed-loop model implementing the estimated transfer functions. The model consists of the human body dynamics, the neural dynamics, the muscular dynamics, the mechanical dynamics, and the sensorimotor time delay. The human body dynamics parameters were based on the anthropometric measurements of the participants, while all other parameters were selected based on the experimental data. The external perturbation is added as an external noise to the system. In response to the external perturbation, the body sway, the weighted EMG, the joint torque, the torque generated by mechanical dynamics, and the torque generated by neural dynamics were obtained. The set-point is set to be zero.

5 Results

5.1 Overview

This chapter presents the results obtained by conducting experiments as described in Chapter 4. It includes the results regarding the external perturbation and the estimation of the neuromusculoskeletal time series. Subsequent to that presentation, the correlation, coherence, and time delay between the external perturbation and the neuromusculoskeletal time series are documented. Next, the non-parametric estimates, parametric estimates, and the stability analysis of the identified mechanisms are presented. Finally, the simulation results are compared with the experimentally identified parameters.

5.2 External Perturbation and Neuromusculoskeletal Time Series Estimation

The time series of the external perturbation and the neuromusculoskeletal time series, including the body sway, the weighted EMG, the top-down joint torque, and the bottom-up joint torque, required knowledge of anthropometric measurements, maximum voluntary contractions (MVC) and Electromyography (EMG) baseline values, and EMG weights.

5.2.1 Body Segment Parameters

Fourteen male individuals participated in this study whose weight, height, mass of the upper body, mean distance (standard deviation, SD) between the center of mass (COM) and the axis of rotation, mean distance (SD) between the base of support and the fifth lumbar vertebra, and the moment of inertia about the axis of rotation are presented in Table 5-1.

5.2.2 Maximum Voluntary Contractions and EMG Baseline

Examples of processed (demeaned, rectified, and filtered) muscle activity time series obtained for the different MVC exercises and muscles (see Section 4.5.2) are presented for one participant in Figure 5-1 (muscles in front of body) and Figure 5-2 (muscles in back of body). The MVC values for the front and back muscles are listed in Table 5-2. Similarly, the EMG baseline values for the front and back muscles are listed in Table 5-3.

Table 5-1. Body Segment Parameters of all the participants. m_{COM} denotes the mass of the upper body, L_{COM} the mean distance (standard deviation, SD) between the center of mass and axis of rotation, d_{L5} the mean distance (SD) between the base of support and the fifth lumbar vertebra, and J the moment of inertia about the axis of rotation.

Participant Number	Weight (kg)	Height (cm)	m_{COM} (kg)	L_{COM} (cm)	d_{L5} (cm)	J (kg·m²)
1	61	173	36.7	33.3 (0.4)	13.1 (1.2)	6.5
2	78	178	47.0	38.1 (0.1)	17.5 (0.3)	11.1
3	85	183	51.3	24.9 (0.1)	13.0 (0.2)	5.1
4	90	187	54.3	39.1 (0.4)	16.4 (0.4)	13.6
5	80	183	48.4	18.1 (0.2)	13.3 (0.4)	2.6
6	60	169	36.2	37.5 (0.1)	21.6 (0.2)	8.3
7	82	183	49.5	39.2 (0.1)	22.8 (0.3)	12.2
8	68	170	41.0	36.9 (0.1)	24.7 (1.4)	8.9
9	86	184	51.9	42.4 (0.1)	28.7 (0.3)	15.0
10	83	182	50.1	34.0 (0.2)	26.2 (0.8)	9.4
11	60	175	36.2	36.9 (0.1)	15.7 (0.4)	7.8
12	92	185	55.3	37.1 (0.2)	15.8 (0.6)	12.2
13	63	164	38.1	35.8 (0.2)	14.7 (0.5)	7.8
14	80	178	48.2	37.3 (0.1)	12.4 (0.8)	10.9
Mean	**76**	**178**	**46.0**	**35.0**	**18.3**	**9.4**
SD	**11**	**7**	**6.7**	**6.1**	**5.3**	**3.3**
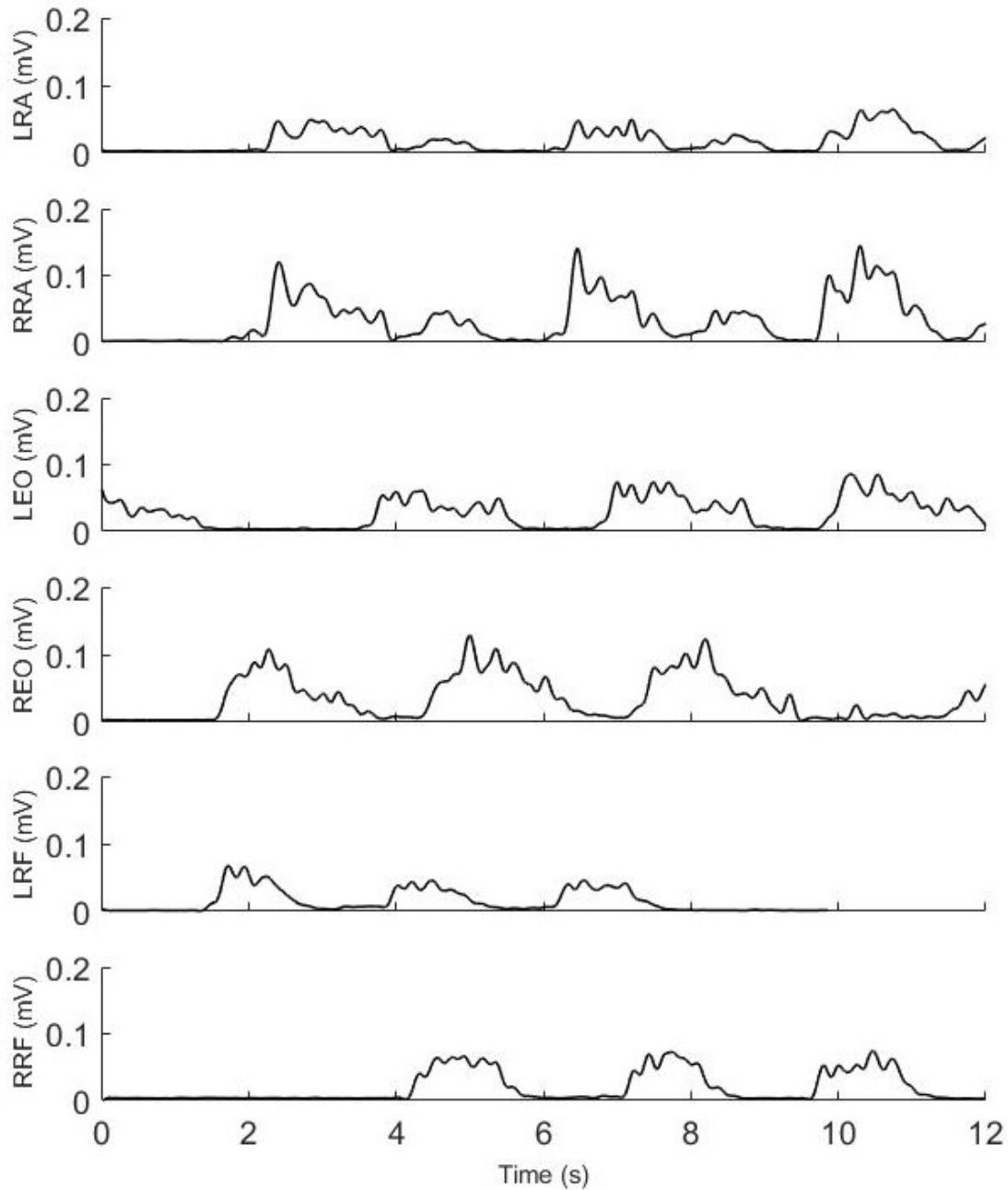
Figure 5-1: Processed electromyography signal (demeaned, rectified, and filtered) of the muscles in the front of the body, obtained during maximum voluntary contractions (MVC) exercises. The figure shows the data for one participant and the various MVC exercises. Note that the three peaks in a given trial correspond to the three bursts of MVC effort applied by the participant. LRA: left rectus abdominis; RRA: right rectus abdominis; LEO: left external obliques; REO: right external obliques; LRF: left rectus femoris; and RRF: right rectus femoris.
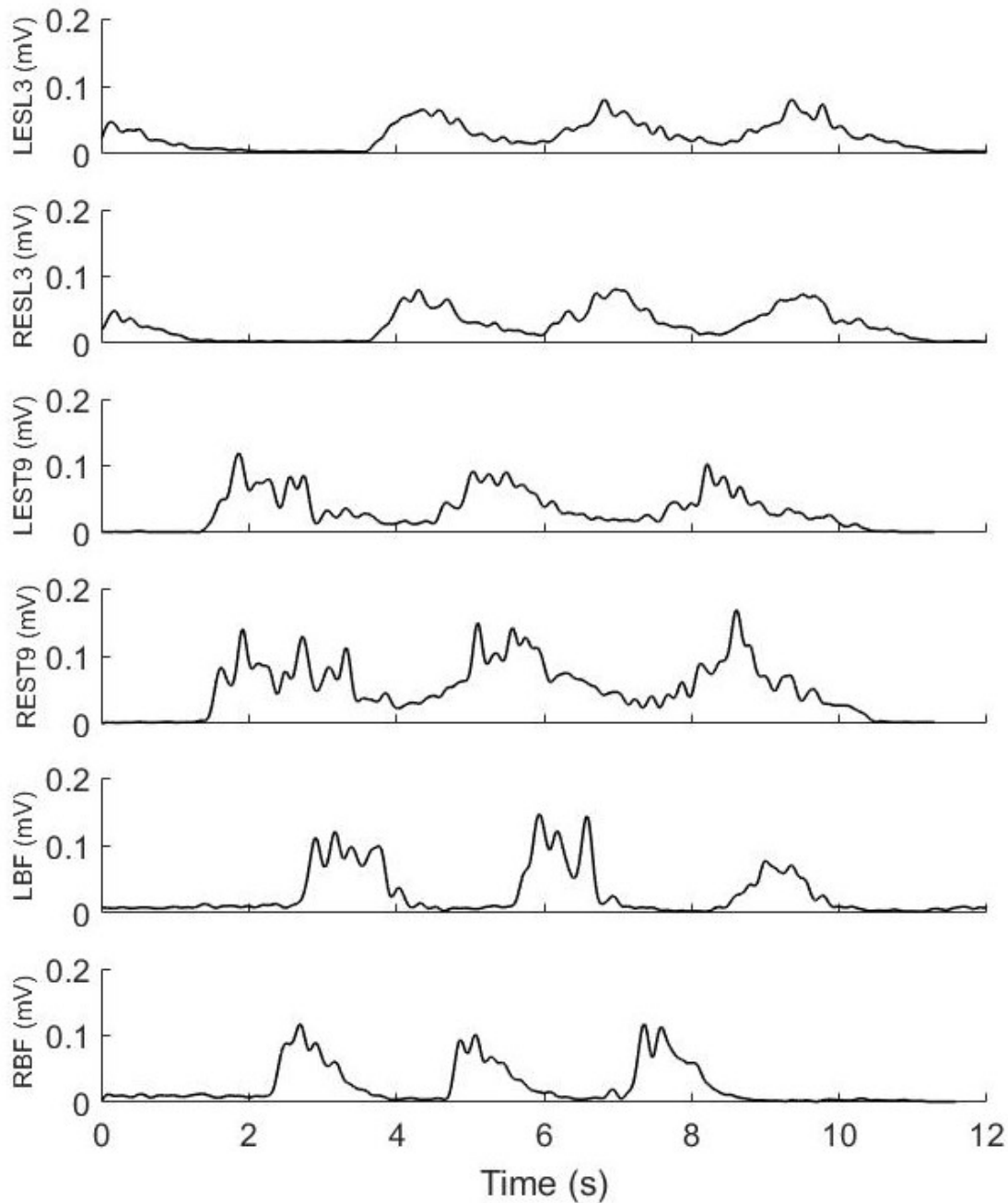
Figure 5-2: Processed electromyography signals (demeaned, rectified, and filtered) of the muscles in the back of the body, obtained during maximum voluntary contractions (MVC) exercises. The figure shows the data for one participant and the various MVC exercises. Note that the three peaks in a given trial correspond to the three bursts of MVC effort applied by the participant. LESL3: Left erector spinae at the third lumbar vertebra; RESL3: Right erector spinae at the third lumbar vertebra; LEST9: Left erector spinae at the ninth thoracic vertebra; REST9: Right erector spinae at the ninth thoracic vertebra; LBF: Left biceps femoris; and RBF: Right biceps femoris.

Table 5-2. Maximum voluntary contractions values for the front and back muscles. RA: rectus abdominis; EO: external obliques; RF: rectus femoris; ESL3: erector spinae at the third lumbar vertebra; EST9: erector spinae at the ninth thoracic vertebra; and BF: biceps femoris. R marks right, and L marks left muscles. SD: Standard deviation.

P No.	RA (mV)		EO (mV)		RF (mV)		ESL3 (mV)		EST9 (mV)		BF (mV)	
	R	L	R	L	R	L	R	L	R	L	R	L
1	0.14	0.24	0.17	0.31	0.07	0.13	0.16	0.16	0.34	0.34	0.12	0.06
2	0.12	0.14	0.16	0.14	0.04	0.03	0.07	0.07	0.14	0.10	0.06	0.06
3	0.12	0.15	0.16	0.15	0.05	0.10	0.05	0.06	0.16	0.27	0.09	0.12
4	0.05	0.05	0.15	0.15	0.10	0.07	0.10	0.08	0.24	0.08	0.09	0.08
5	0.24	0.10	0.24	0.29	0.20	0.14	0.10	0.10	0.11	0.09	0.22	0.18
6	0.16	0.08	0.08	0.09	0.13	0.07	0.08	0.08	0.24	0.15	0.13	0.19
7	0.14	0.06	0.13	0.09	0.07	0.07	0.08	0.08	0.17	0.12	0.12	0.15
8	0.05	0.09	0.09	0.05	0.12	0.05	0.07	0.07	0.25	0.23	0.09	0.10
9	0.08	0.05	0.03	0.06	0.09	0.03	0.06	0.08	0.09	0.10	0.20	0.11
10	0.08	0.10	0.14	0.18	0.13	0.05	0.16	0.13	0.34	0.16	0.12	0.13
11	0.18	0.09	0.23	0.19	0.12	0.12	0.14	0.15	0.09	0.06	0.19	0.13
12	0.12	0.10	0.08	0.16	0.18	0.17	0.08	0.09	0.27	0.22	0.10	0.14
13	0.03	0.04	0.12	0.17	0.08	0.12	0.09	0.17	0.14	0.19	0.08	0.08
14	0.17	0.20	0.04	0.05	0.03	0.03	0.05	0.06	0.04	0.03	0.19	0.16
Mean	**0.12**	**0.11**	**0.13**	**0.15**	**0.10**	**0.08**	**0.09**	**0.10**	**0.19**	**0.15**	**0.13**	**0.12**
SD	**0.06**	**0.06**	**0.06**	**0.08**	**0.05**	**0.04**	**0.04**	**0.04**	**0.09**	**0.08**	**0.05**	**0.04**

Table 5-3. Electromyography baseline values for the front and back muscles. RA: rectus abdominis; EO: external obliques; RF: rectus femoris; ESL3: erector spinae at the third lumbar vertebra; EST9: erector spinae at the ninth thoracic vertebra; and BF: biceps femoris. R marks right, and L marks left muscles. SD: Standard deviation.

P No.	RA (μV)		EO (μV)		RF (μV)		ESL3 (μV)		EST9 (μV)		BF (μV)	
	R	L	R	L	R	L	R	L	R	L	R	L
1	1.4	1.7	1.6	1.6	1.6	1.5	2.1	1.4	2.9	2.2	1.9	2.2
2	2.7	2.8	1.8	1.9	3.3	1.3	2.2	1.9	2.5	2.1	1.2	5.4
3	1.6	1.9	2.3	1.8	2.1	2.1	2.4	2.2	1.9	2.3	2.0	3.0
4	1.8	1.7	2.4	2.1	1.9	1.5	1.6	1.5	2.3	3.3	1.7	2.0
5	1.8	1.6	2.3	1.7	1.9	1.8	2.7	3.5	2.5	2.4	0.4	2.2
6	1.6	1.6	1.6	1.5	1.7	1.6	1.9	1.5	2.1	2.1	1.9	1.6
7	1.8	2.4	2.1	3.3	2.0	2.1	1.9	1.6	1.9	1.5	1.3	2.1
8	1.5	1.8	1.7	1.7	1.5	1.7	1.5	1.4	2.1	2.1	2.4	1.2
9	2.6	8.9	1.7	1.8	5.1	1.7	2.4	1.9	2.2	2.3	1.8	3.0
10	1.7	2.3	1.9	2.1	1.6	1.6	1.6	1.6	1.7	3.0	2.0	1.7
11	2.1	2.6	2.6	2.7	1.7	1.6	2.1	1.7	2.3	2.3	1.6	1.6
12	2.0	3.1	1.4	1.2	3.6	3.0	2.6	2.0	8.1	5.1	1.9	3.2
13	1.4	1.6	1.8	1.6	1.6	2.2	1.8	2.7	2.0	3.6	0.9	1.1
14	2.1	2.8	2.2	2.0	2.7	1.9	1.5	1.5	1.5	1.7	1.7	2.5
Mean	1.9	2.6	2.0	1.9	2.3	1.8	2.0	1.9	2.6	2.6	1.6	2.3
SD	0.4	1.8	0.3	0.5	1.0	0.4	0.4	0.6	1.6	0.9	0.5	1.1

The comparison of the left and right muscle's MVC values, and the comparison of the left and right muscle's EMG baseline values revealed a p-value of $p > 0.05$ when using the Wilcoxon signed rank test. Only exception was the EMG baseline values for rectus abdominis (RA) and biceps femoris (BF), which had p-values of $p = 0.002$ and $p = 0.042$, respectively. As such, there was no difference in MVC and baseline values for most muscles when comparing the same muscle across body sides.

5.2.3 EMG Weights

The weights for individual muscles across participants that were identified for the perturbation trials are presented in Table 5-4 and Table 5-5.

Table 5-4. The mean electromyography weights (standard deviation) for the front muscles as obtained in all perturbation trials. RA: rectus abdominis; EO: external obliques; and RF: rectus femoris. R marks right, and L marks left muscles.

P	RA		EO		RF	
No.	R	L	R	L	R	L
1	-0.000	-0.148	-0.110	-0.195	-0.065	-0.007
	(0.000)	(0.064)	(0.070)	(0.040)	(0.023)	(0.010)
2	-0.138	-0.096	-0.124	-0.171	-0.006	-0.001
	(0.020)	(0.059)	(0.025)	(0.017)	(0.006)	(0.001)
3	-0.142	-0.034	-0.001	-0.085	-0.000	-0.000
	(0.108)	(0.049)	(0.001)	(0.120)	(0.000)	(0.000)
4	-0.000	-0.000	-0.203	-0.251	-0.118	-0.122
	(0.000)	(0.000)	(0.158)	(0.189)	(0.167)	(0.149)
5	-0.021	-0.000	-0.123	-0.215	-0.069	-0.071
	(0.030)	(0.001)	(0.070)	(0.050)	(0.046)	(0.101)
6	-0.297	-0.075	-0.059	-0.251	-0.031	-0.000
	(0.106)	(0.045)	(0.072)	(0.096)	(0.043)	(0.000)

	ESL3		EST9		BF	
7	-0.044	-0.026	-0.093	-0.004	-0.015	-0.014
	(0.022)	(0.011)	(0.029)	(0.005)	(0.020)	(0.013)
8	-0.014	-0.063	-0.095	-0.066	-0.041	-0.027
	(0.016)	(0.047)	(0.054)	(0.021)	(0.020)	(0.022)
9	-0.069	-0.029	-0.040	-0.131	-0.003	-0.003
	(0.049)	(0.024)	(0.036)	(0.057)	(0.004)	(0.004)
10	-0.040	-0.023	-0.062	-0.115	-0.148	-0.012
	(0.029)	(0.024)	(0.008)	(0.057)	(0.029)	(0.009)
11	-0.020	-0.049	-0.129	-0.142	-0.039	-0.016
	(0.022)	(0.041)	(0.091)	(0.056)	(0.024)	(0.023)
12	-0.024	-0.010	-0.191	-0.159	-0.043	-0.041
	(0.035)	(0.014)	(0.091)	(0.086)	(0.021)	(0.058)
13	-0.046	-0.033	-0.062	-0.227	-0.035	-0.214
	(0.009)	(0.007)	(0.026)	(0.048)	(0.014)	(0.013)
14	-0.356	-0.034	-0.186	-0.115	-0.030	-0.009
	(0.262)	(0.048)	(0.059)	(0.072)	(0.021)	(0.008)

Table 5-5. The mean electromyography weights (standard deviation) for the back muscles as obtained in all perturbation trials. ESL3: erector spinae at the third lumbar vertebra; EST9: erector spinae at the ninth thoracic vertebra; and BF: biceps femoris. R marks right, and L marks left muscles.

P	ESL3		EST9		BF	
No.	R	L	R	L	R	L
1	0.080	0.049	0.217	0.074	0.037	0.018
	(0.023)	(0.044)	(0.053)	(0.025)	(0.034)	(0.015)

2	0.123	0.142	0.034	0.153	0.013	0.000
	(0.001)	(0.000)	(0.011)	(0.027)	(0.013)	(0.000)
3	0.179	0.222	0.007	0.100	0.119	0.111
	(0.049)	(0.033)	(0.010)	(0.075)	(0.097)	(0.069)
4	0.100	0.090	0.059	0.009	0.000	0.048
	(0.088)	(0.076)	(0.083)	(0.008)	(0.000)	(0.064)
5	0.000	0.127	0.110	0.095	0.083	0.085
	(0.000)	(0.090)	(0.017)	(0.014)	(0.053)	(0.117)
6	0.036	0.074	0.029	0.096	0.014	0.038
	(0.004)	(0.036)	(0.018)	(0.044)	(0.013)	(0.054)
7	0.461	0.051	0.098	0.079	0.116	0.000
	(0.209)	(0.016)	(0.029)	(0.029)	(0.062)	(0.000)
8	0.054	0.098	0.159	0.168	0.014	0.201
	(0.039)	(0.007)	(0.086)	(0.023)	(0.017)	(0.081)
9	0.075	0.106	0.087	0.089	0.313	0.055
	(0.025)	(0.045)	(0.069)	(0.046)	(0.232)	(0.053)
10	0.062	0.095	0.215	0.071	0.034	0.124
	(0.012)	(0.041)	(0.033)	(0.023)	(0.043)	(0.096)
11	0.177	0.214	0.014	0.011	0.101	0.089
	(0.065)	(0.105)	(0.009)	(0.001)	(0.089)	(0.066)
12	0.094	0.001	0.105	0.089	0.044	0.199
	(0.042)	(0.002)	(0.007)	(0.027)	(0.032)	(0.070)
13	0.099	0.045	0.045	0.156	0.018	0.020
	(0.028)	(0.026)	(0.016)	(0.036)	(0.026)	(0.028)
14	0.116	0.078	0.029	0.047	0.000	0.000
	(0.052)	(0.037)	(0.015)	(0.011)	(0.000)	(0.000)

The mean EMG weights for each muscle and all participants, along with their 95% confidence interval, are depicted in Figure 5-3. The external obliques (EO) seem to provide the largest magnitude in weights (left EO: -0.152 and right EO: -0.105) in the front trunk muscles, and the erector spinae at third lumbar vertebra (ESL3) seem to provide the largest magnitude in weights (left ESL3: 0.099 and right ESL3: 0.118) in the back trunk muscles. Both leg muscles (rectus femoris, RF and BF) provided relatively small magnitudes in weights (left RF: -0.038, right RF: -0.046, left BF: 0.071, and right BF: 0.065).
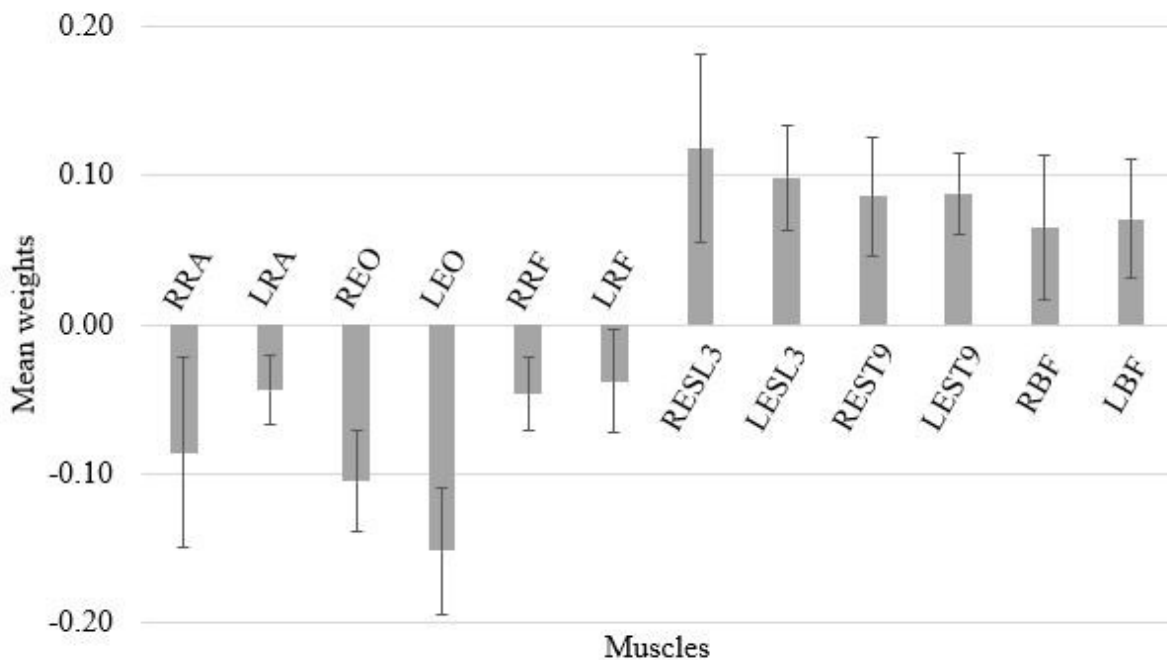
Figure 5-3: The mean electromyography weights for each muscle and all participants, with error bars marking the 95% confidence interval. RA: rectus abdominis; EO: external obliques; RF: rectus femoris; ESL3: erector spinae at third lumbar vertebra; EST9: erector spinae at ninth thoracic vertebra; and BF: bices femoris. R marks right, and L marks left muscles.

5.2.4 Time Series

The time series of the external perturbation, the body sway, the weighted EMG, the top-down joint torque and the bottom-up joint torque for one trial of one participant are presented in Figure 5-4. A visual inspection suggests, that the external perturbation, the body sway, and the weighted EMG

signals follow similar trends. However, the top-down and bottom-up joint torques adhere to a reversal of sign when compared to the external perturbation. This and previous correlation analyses suggest that the body sway and weighted EMG signals were in phase with the external perturbation, whereas the top-down and bottom-up joint torque signals were 180° out of phase with the external perturbation.
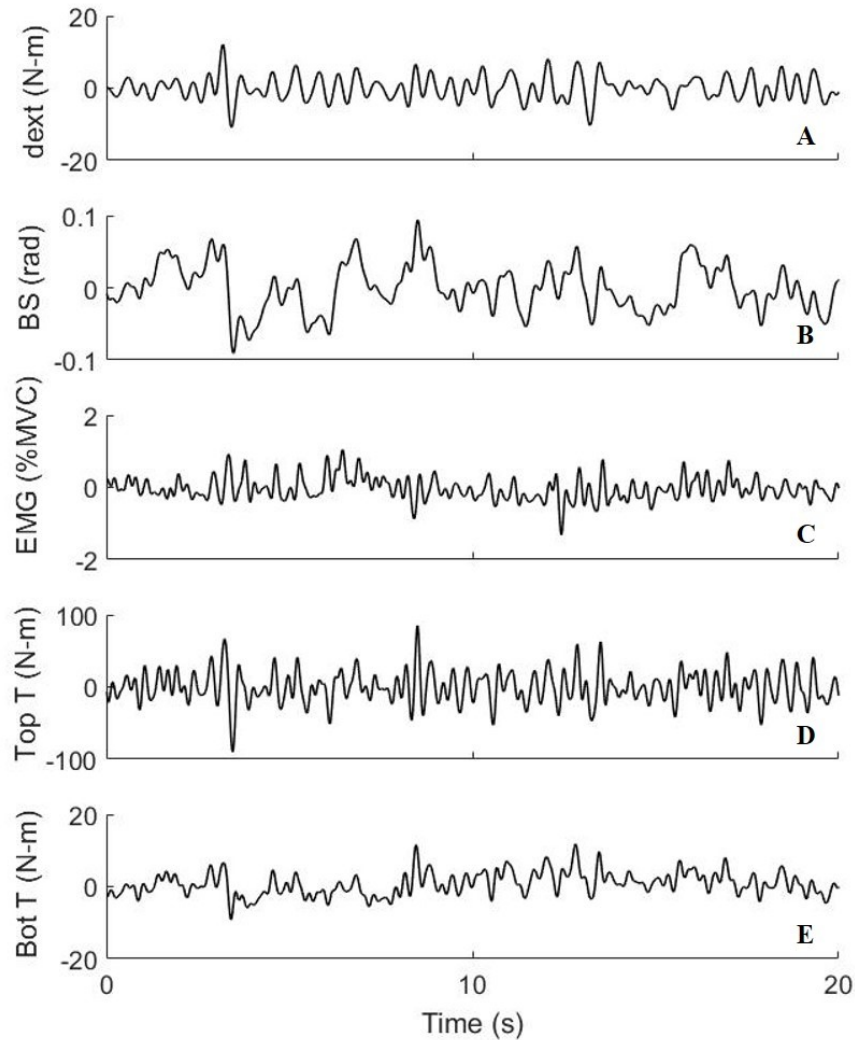
Figure 5-4: The time series of the external perturbation, the body sway, the weighted EMG, the top-down torque and bottom-down torque for one participant and one trial. (A) dext: external perturbation; (B) BS: body sway; (C) EMG: weighted EMG; (D) Top T: top-down joint torque; and (E) Bot T: bottom-up joint torque.

5.3 Correlations, Coherence, and Time Delay between External Perturbation and Neuromusculoskeletal Time Series

The normalized cross-correlations and the mean squared coherence between the external perturbation and the neuromusculoskeletal time series (including the body sway, the weighted EMG, the top-down joint torque, and the bottom-up joint torque) are presented in Table 5-6 to Table 5-9. The absolute cross-correlation coefficients and the mean squared coherence values between the external perturbation and all time series were high. The time delay was small between the external perturbation and the body sway (0.00–0.04 s), followed by a larger time delay between the external perturbation and the weighted EMG (0.10–0.23 s), and an even larger time delay between the external perturbation and the joint torque (top-down joint torque: 0.27–0.32 s, and bottom-up joint torque: 0.26–0.50 s).

Table 5-6. The normalized cross-correlation coefficient values, time delays, and mean squared coherence values between the external perturbation and the body sway across all participants. The mean values (standard deviation, SD) from three trials are presented.

Participant Number	Body Sway		
	Correlation Coefficient	Delay (s)	Mean Squared Coherence
1	0.42 (0.04)	0.02 (0.01)	0.84 (0.04)
2	0.45 (0.02)	0.04 (0.00)	0.86 (0.02)
3	0.42 (0.02)	0.03 (0.00)	0.82 (0.02)
4	0.45 (0.03)	0.04 (0.00)	0.78 (0.02)
5	0.55 (0.00)	0.04 (0.01)	0.83 (0.01)
6	0.47 (0.03)	0.00 (0.01)	0.83 (0.01)
7	0.43 (0.02)	0.03 (0.00)	0.86 (0.01)
8	0.45 (0.03)	0.01 (0.00)	0.81 (0.03)
9	0.40 (0.04)	0.04 (0.00)	0.81 (0.01)
10	0.55 (0.03)	0.01 (0.00)	0.90 (0.01)
11	0.45 (0.02)	0.00 (0.00)	0.87 (0.02)
12	0.29 (0.14)	0.03 (0.01)	0.67 (0.11)
13	0.59 (0.01)	0.02 (0.00)	0.89 (0.02)
14	0.61 (0.03)	0.01 (0.00)	0.88 (0.01)
Mean (SD)	**0.47 (0.08)**	**0.02 (0.01)**	**0.83 (0.05)**

Table 5-7. The normalized cross-correlation coefficient values, time delays, and mean squared coherence values between the external perturbation and the weighted EMG across all participants. The mean values (standard deviation, SD) from three trials are presented.

Participant Number	Weighted EMG		
	Correlation Coefficient	Delay (s)	Mean Squared Coherence
1	0.51 (0.10)	0.14 (0.01)	0.61 (0.07)
2	0.38 (0.01)	0.18 (0.00)	0.48 (0.01)
3	0.48 (0.02)	0.16 (0.00)	0.55 (0.03)
4	0.37 (0.02)	0.23 (0.02)	0.37 (0.01)
5	0.54 (0.09)	0.17 (0.02)	0.61 (0.02)
6	0.65 (0.02)	0.15 (0.01)	0.63 (0.03)
7	0.42 (0.03)	0.14 (0.00)	0.46 (0.08)
8	0.55 (0.07)	0.15 (0.00)	0.57 (0.03)
9	0.54 (0.03)	0.21 (0.00)	0.56 (0.00)
10	0.68 (0.04)	0.16 (0.00)	0.69 (0.01)
11	0.48 (0.04)	0.15 (0.00)	0.61 (0.04)
12	0.35 (0.10)	0.15 (0.01)	0.38 (0.03)
13	0.60 (0.03)	0.16 (0.01)	0.53 (0.02)
14	0.57 (0.01)	0.10 (0.01)	0.57 (0.00)
Mean (SD)	**0.51 (0.10)**	**0.16 (0.03)**	**0.54 (0.09)**

Table 5-8. The normalized cross-correlation coefficient values, time delays, and mean squared coherence values between the external perturbation and the top-down joint torque across all participants. The mean values (standard deviation, SD) from three trials are presented.

Participant Number	Top-Down Joint Torque		
	Correlation Coefficient	Delay (s)	Mean Squared Coherence
1	-0.63 (0.02)	0.28 (0.01)	0.86 (0.04)
2	-0.64 (0.01)	0.30 (0.00)	0.88 (0.02)
3	-0.61 (0.01)	0.30 (0.00)	0.83 (0.02)
4	-0.68 (0.01)	0.31 (0.00)	0.80 (0.02)
5	-0.71 (0.01)	0.32 (0.01)	0.84 (0.01)
6	-0.61 (0.03)	0.27 (0.01)	0.84 (0.01)
7	-0.63 (0.02)	0.29 (0.00)	0.87 (0.01)
8	-0.68 (0.04)	0.30 (0.01)	0.83 (0.03)
9	-0.65 (0.02)	0.32 (0.00)	0.83 (0.01)
10	-0.75 (0.02)	0.30 (0.00)	0.91 (0.01)
11	-0.53 (0.03)	0.27 (0.00)	0.88 (0.02)
12	-0.60 (0.08)	0.31 (0.01)	0.71 (0.09)
13	-0.66 (0.03)	0.28 (0.00)	0.89 (0.02)
14	-0.63 (0.01)	0.27 (0.00)	0.89 (0.01)
Mean (SD)	**-0.64 (0.05)**	**0.29 (0.02)**	**0.85 (0.05)**

Table 5-9. The normalized cross-correlation coefficient values, time delays, and mean squared coherence values between the external perturbation the bottom-up joint torque across all participants. The mean values (standard deviation, SD) from three trials are presented.

Participant Number	Bottom-Up Joint Torque		
	Correlation Coefficient	Delay (s)	Mean Squared Coherence
1	-0.31 (0.06)	0.29 (0.00)	0.83 (0.04)
2	-0.24 (0.01)	0.35 (0.01)	0.82 (0.02)
3	-0.23 (0.02)	0.33 (0.00)	0.77 (0.04)
4	-0.32 (0.04)	0.30 (0.19)	0.61 (0.02)
5	-0.33 (0.07)	0.26 (0.00)	0.77 (0.03)
6	-0.58 (0.05)	0.32 (0.01)	0.84 (0.01)
7	-0.29 (0.03)	0.32 (0.01)	0.86 (0.01)
8	-0.36 (0.05)	0.34 (0.02)	0.82 (0.03)
9	-0.30 (0.06)	0.39 (0.01)	0.81 (0.01)
10	-0.51 (0.04)	0.31 (0.00)	0.90 (0.01)
11	-0.46 (0.03)	0.34 (0.01)	0.85 (0.02)
12	-0.17 (0.03)	0.50 (0.13)	0.62 (0.02)
13	-0.38 (0.02)	0.30 (0.01)	0.89 (0.02)
14	-0.61 (0.07)	0.27 (0.02)	0.85 (0.01)
Mean (SD)	**-0.36 (0.13)**	**0.33(0.06)**	**0.80 (0.09)**

5.4 Estimates of the Mechanisms of Seated Balance

We obtained the non-parametric estimates of the active and active-passive controller components as well as the parametric estimates of the neural dynamics, the mechanical dynamics, the muscular

dynamics, and the sensorimotor time delay. The stability analysis assesses the stability of the identified mechanisms when implemented in a closed-loop system.

5.4.1   Non-parametric Estimates

The non-parametric estimates of the active, active-passive (calculated using top-down joint torque), and active-passive controller components (calculated using bottom-up joint torque) are presented in Figure 5-5. For the active and active-passive (calculated using top-down joint torque) controller components, the gain of the frequency response was approximately constant for lower frequencies (< 0.4 Hz) and then steadily rose as the frequency increased. For the active-passive controller components (calculated using bottom-up joint torque), the gain of the frequency response was approximately constant for lower frequencies (< 1.5 Hz) and then steadily rose as the frequency increased.

The frequency response of the active control components had a phase of 30 degrees for the lower frequencies and steadily rose as the frequency increased; however, it saturated around 110 degrees as the frequency reached approximately 3 Hz. The frequency response of the active-passive control components (calculated using top-down joint torque) had a constant phase of approximately 180 degrees for the lower frequencies (< 1Hz) that gradually increased to approximately 185 degrees at 2.5 Hz and then settled at approximately 180 degrees. The frequency response of the active-passive control components (calculated using bottom-up joint torque) had a constant phase of approximately 180 degrees for the lower frequencies (< 1.4 Hz) and steadily rose as the frequency increased.

The across-participant variability of the non-parametric estimates of the active, active-passive (calculated using top-down joint torque), and active-passive (calculated using bottom-up joint torque) controller components was small. The standard errors of the gain and phase in the frequency response of the active control components ranged from 3.1 to 5.8 dB and from 7.8 to 32.9 degrees, respectively, across the different frequencies. The standard errors of the gain and phase in the frequency response of the active-passive control components (calculated using top-down joint torque) ranged from 2.3 to 3.1 dB and from 0.2 to 4.3 degrees, respectively, across the different frequencies. The standard errors of the gain and phase in the frequency response of the active-passive control components (calculated using bottom-up joint torque) ranged from 3.8 to 13.4 dB and from 6.9 to 37.2 degrees, respectively, across the different frequencies.
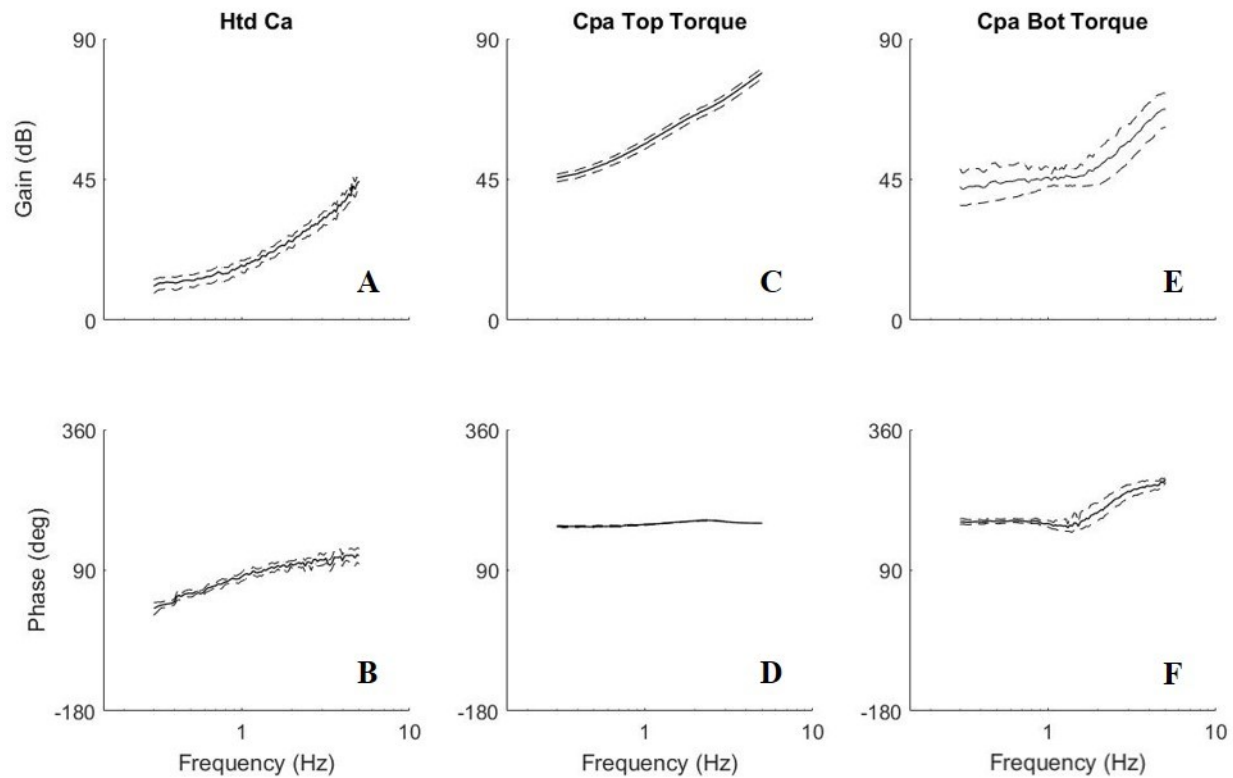
Figure 5-5: Non-parametric estimates of active, active-passive (calculated using top-down joint torque), and active-passive (calculated using bottom-up joint torque) controller components. (A-B) Htd Ca: active control components; (C-D) Cpa Top Torque: active-passive control components (calculated using top-down joint torque); and (E-F) Cpa Bot Torque: active-passive control components (calculated using bottom-up joint torque). The solid and dashed lines represent the mean and the bootstrap standard error, respectively.

5.4.2 Parametric Estimates

The non-parametric estimates obtained in the last section were further used to obtain the parametric estimates of the neural dynamics, the mechanical dynamics, the muscular dynamics, and the sensorimotor time delay. The equations that fit the non-parametric estimates of the active, active-passive (calculated using top-down joint torque), and active-passive (calculated using bottom-up joint torque) controller components, are presented in Equations (90-92), where $H_{TD}C_A$ represents the active controller components, C_{PA-T} the active-passive controller components (calculated

using top-down joint torque), C_{PA-B} the active-passive controller components (calculated using bottom-up joint torque), and s the Laplace variable, with all other symbols being constants.

$$H_{TD}C_A = C_1 * e^{-TDs} * (K_A + D_As + A_As^2) \qquad \text{Eq. (90)}$$

$$C_{PA-T} = -K_P - D_Ps + \left[C_1 * e^{-TDs} * (K_A + D_As + A_As^2) * \frac{C_2(1+a_1s)}{(1+b_1s-b_2s^2)} \right] \qquad \text{Eq. (91)}$$

$$C_{PA-B} = -K_{P2} + \left[C_1 * e^{-TDs} * (K_A + D_As + A_As^2) * \frac{C_3(1-a_2s-a_3s^2-a_4s^3)}{(1+b_3s)} \right] \qquad \text{Eq. (92)}$$

The neural dynamics were identified as a proportional-derivative (PD) controller with acceleration feedback, the sensorimotor time delay as an exponential decay function, the mechanical dynamics as a PD controller (estimated using top-down joint torque) and proportional controller (estimated using bottom-up joint torque), and the muscle activation dynamics as a second-order transfer function (estimated using top-down joint torque) and third-order transfer function (estimated using bottom-up joint torque). The across-participant values of the parametric estimates, goodness-of-fit (GOF), Akaike information criteria (AIC), and variance accounted for (VAF) for the active, active-passive (calculated using top-down joint torque), and active-passive (calculated using bottom-up joint torque) control components are presented in Table 5-10 to Table 5-12.

Table 5-10. The across-participant values of the parameters for the active control components. K_A, D_A, A_A, TD, and C_1 are constants, GOF% the goodness-of-fit, AIC the Akaike Information Criterion, and VAF the variance-accounted-for. SD: Standard deviation.

P No.	$K_A \frac{N{\cdot}m}{rad}$	$D_A \frac{N{\cdot}m{\cdot}s}{rad}$	$A_A \frac{N{\cdot}m{\cdot}s^2}{rad}$	$TD\ ms$	C_1	GOF%	AIC	VAF
1	1144.9	379.5	42.1	34	0.0024	99.74	1.19	41.96
2	1095.0	280.4	25.3	38	0.0035	99.61	1.31	41.36
3	837.6	280.4	30.5	48	0.0063	99.51	1.24	50.35
4	1526.4	365.5	26.4	21	0.0031	99.49	1.54	28.95
5	1419.3	322.1	36.3	29	0.0032	99.69	1.18	56.84
6	1356.3	393.5	32.6	36	0.0041	99.69	1.24	50.25
7	1445.0	466.1	51.0	28	0.0010	99.60	1.28	41.20
8	1272.3	374.0	60.2	52	0.0029	99.82	1.10	54.61
9	1137.9	361.2	25.9	47	0.0055	99.64	1.15	59.48
10	1243.2	361.4	33.0	37	0.0029	99.71	1.17	60.75
11	1086.8	268.3	19.6	37	0.0061	99.68	1.13	50.74
12	1597.5	348.6	46.0	21	0.0015	99.24	1.40	36.24
13	1277.2	493.2	36.3	32	0.0010	99.61	1.24	47.32
14	956.4	342.6	47.9	20	0.0033	99.76	1.22	60.47
Mean	**1242.6**	**359.8**	**36.7**	**34.3**	**0.0033**	**99.63**	**1.24**	**48.61**
SD	**208.1**	**61.9**	**11.1**	**9.7**	**0.0016**	**0.14**	**0.11**	**9.31**

Table 5-11. The across-participant values of the parameters for the active-passive (calculated using top-down joint torque) control components. K_P, D_P, a_1, b_1, b_2, and C_2 are constants. GOF% the goodness-of-fit, AIC the Akaike Information Criterion, and VAF the variance-accounted-for. SD: Standard deviation.

P No.	$K_P \frac{N \cdot m}{rad}$	$D_P \frac{N \cdot m \cdot s}{rad}$	a_1	b_1	b_2	C_2	GOF%	AIC	VAF
1	437.2	89.1	492.1	305.2	12.7	53.2	99.92	0.49	99.03
2	706.3	152.5	423.2	170.5	6.8	56.6	99.92	0.48	99.02
3	356.7	66.7	549.8	370.8	14.2	41.3	99.92	0.36	99.70
4	798.3	169.3	547.4	145.3	5.9	42.5	99.90	0.52	99.31
5	202.5	31.5	149.0	348.4	14.0	70.0	99.91	0.44	99.54
6	501.8	107.0	363.7	242.4	9.7	69.6	99.93	0.40	99.36
7	755.8	161.7	380.8	175.6	6.9	69.8	99.92	0.41	99.44
8	565.1	115.1	371.0	202.5	8.7	62.3	99.91	0.47	99.11
9	897.2	201.2	245.1	123.8	5.0	93.9	99.90	0.51	99.02
10	579.5	117.5	439.8	208.5	8.5	54.2	99.91	0.41	99.53
11	496.5	108.0	423.9	328.1	13.0	79.9	99.94	0.35	99.52
12	767.6	164.4	396.4	186.3	7.8	72.2	99.90	0.54	97.66
13	495.8	103.7	438.6	249.6	10.2	56.5	99.92	0.40	99.39
14	669.7	134.2	413.6	181.9	7.4	58.9	99.92	0.37	99.53
Mean	587.9	123.0	402.5	231.4	9.3	62.9	99.92	0.44	99.23
SD	183.4	43.2	102.3	75.6	2.9	13.7	0.01	0.06	0.48

Table 5-12. The across-participant values of the parameters for the active-passive (calculated using bottom-up joint torque) control components. K_{P2}, a_2, a_3, a_4, b_3, and C_3 are constants. GOF% the goodness-of-fit, AIC the Akaike Information Criterion, and VAF the variance-accounted-for. SD: Standard deviation.

P No.	$K_{P2} \frac{N \cdot m}{rad}$	b_3	a_2	a_3	a_4	C_3	GOF%	AIC	VAF
1	101.1	583.1	986.3	215.7	21.7	0.4	99.78	0.76	53.26
2	112.5	458.9	1164.2	126.2	16.7	0.6	99.80	0.90	70.87
3	91.6	1081.9	84.6	134.9	16.3	1.0	99.79	0.77	84.33
4	377.4	73.0	0.0	154.1	14.0	2.1	99.27	1.62	14.98
5	51.5	973.0	0.0	198.3	18.9	1.5	99.42	1.07	36.68
6	164.7	431.1	1470.4	76.7	7.2	1.0	99.77	0.80	54.95
7	153.6	577.5	811.7	64.6	6.6	2.3	99.78	0.75	63.82
8	131.0	310.1	1285.2	171.5	8.0	0.9	99.78	0.92	47.19
9	181.5	293.3	1293.7	74.1	10.1	1.3	99.76	0.94	68.71
10	145.6	343.2	1037.3	93.1	7.1	1.6	99.80	0.77	85.24
11	132.2	773.1	1084.5	106.8	5.0	1.0	99.79	0.81	65.60
12	133.1	682.0	0.0	232.5	22.7	0.8	99.64	1.00	68.02
13	90.5	810.3	0.3	249.1	30.8	0.4	99.83	0.77	82.45
14	134.3	660.8	0.0	412.0	23.1	0.3	99.78	0.97	69.64
Mean	**142.9**	**575.1**	**658.4**	**165.0**	**14.9**	**1.1**	**99.71**	**0.92**	**61.84**
SD	**72.7**	**269.7**	**577.2**	**90.1**	**7.6**	**0.6**	**0.16**	**0.22**	**18.69**

The fitting of the frequency response for the parametric equations with that for the mean non-parametric estimates of the active, active-passive (calculated using top-down joint torque), and active-passive (calculated using bottom-up joint torque) controller components is shown in Figure 5-6. The GOF and AIC values for respective fitting were 99.77 % and 0.92 (active components), 99.92 % and 0.39 (active-passive components using top-down joint torque), and 99.82 % and 0.63 (active-passive components using bottom-up joint torque), respectively.
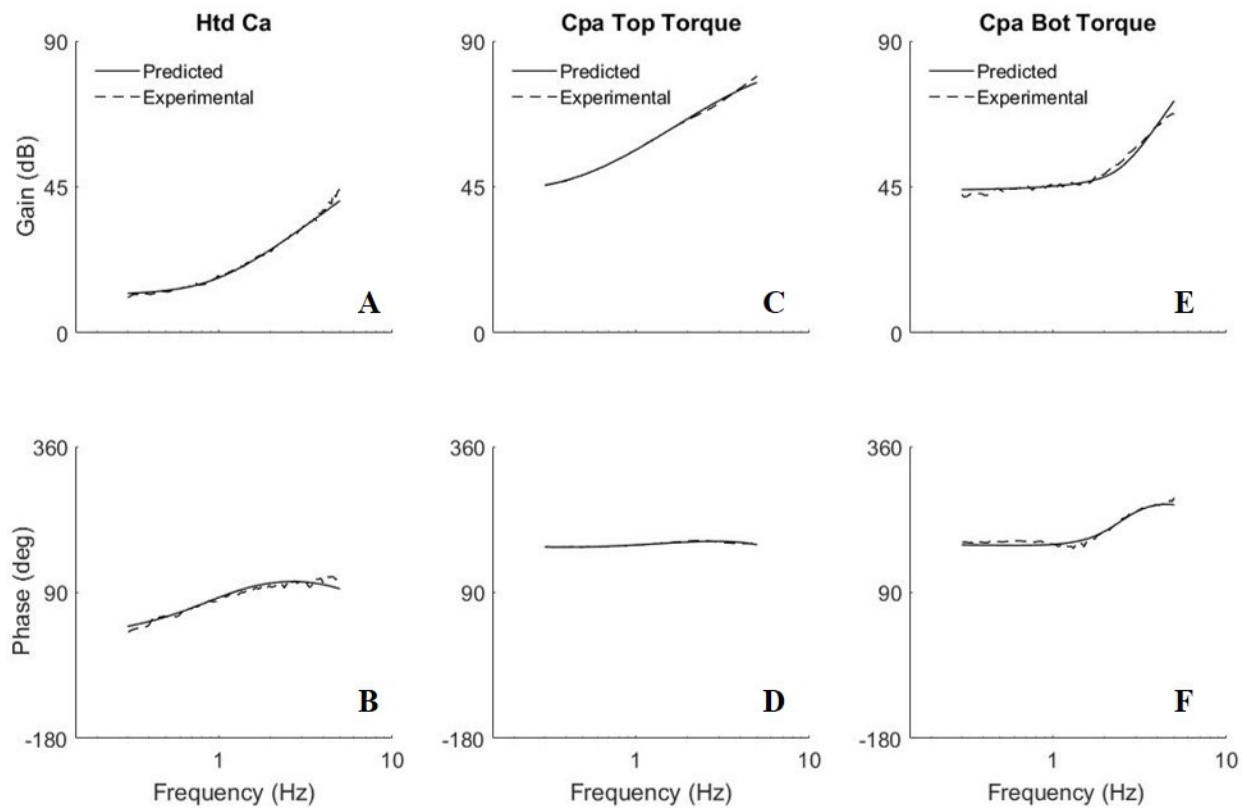
Figure 5-6: The fitting of the frequency response for the parametric equations with that for the mean non-parametric estimates of the active, active-passive (calculated using top-down joint torque), and active-passive (calculated using bottom-up joint torque) controller components. (A-B) Htd Ca: active control components; (C-D) Cpa Top Torque: active-passive (calculated using top-down joint torque) control components; and (E-F) Cpa Bot Torque: active-passive (calculated using bottom-up joint torque) control components.

The parameters obtained from the fitting are presented in Table 5-13. Parameters including J, l_{COM} and m_{COM} are the mean of the participant's moment of inertia, distance of the COM from the joint of rotation, and upper body mass, respectively.

Table 5-13: The parameters obtained from fitting. Top Torque: active-passive control components (calculated using top-down joint torque); and Bot Torque: active-passive control components (calculated using bottom-up joint torque).

Parameter	Symbol	Mean Value (SD)
Moment of Inertia	J	9.4 (3.3) $kg \cdot m^2$
Length from axis of rotation to COM	l_{COM}	35 (6) cm
Mass of upper body	m_{COM}	46 (7) kg
Reflexive stiffness	K_A	964.5 (208.1) $\frac{N \cdot m}{rad}$
Reflexive damping	D_A	280.0 (61.9) $\frac{N \cdot m \cdot s}{rad}$
Acceleration feedback	A_A	27.2 (11.1) $\frac{N \cdot m \cdot s^2}{rad}$
Sensorimotor time delay	TD	36 (10) ms
EMG normalization constant	C_1	0.0040 (0.0016)
Passive stiffness (Top torque)	K_P	588.5 (183.4) $\frac{N \cdot m}{rad}$
Passive Damping (Top torque)	D_P	122.9 (43.2) $\frac{N \cdot m}{rad}$
Passive stiffness (Bot torque)	K_{P2}	164.5 (72.6) $\frac{N \cdot m}{rad}$
Muscular dynamics (Top torque)	C_2	54.6 (13.7)
Muscular dynamics (Bot torque)	C_3	1.0 (0.6)
Muscular dynamics (Top torque)	a_1	407.6 (102.3)

Muscular dynamics (Bot torque)	a_2	630.9 (577.2)
Muscular dynamics (Bot torque)	a_3	184.4 (90.1)
Muscular dynamics (Bot torque)	a_4	15.4 (7.6)
Muscular dynamics (Top torque)	b_1	190.2 (75.6)
Muscular dynamics (Top torque)	b_2	7.8 (2.9)
Muscular dynamics (Bot torque)	b_3	458.1 (269.7)

5.4.3 Stability Analysis

The poles and zeros of the characteristic equation (Equation (88)) were computed using the parameters listed in Table 5-13. The parameters for the muscular dynamics and the mechanical dynamics computed using the top-down joint torque were implemented to quantify the characteristic equation. There were four zeros at (-3.4 + j 2.4), (-3.4 - j 2.4), (195.5 + j 0.0), and (-0.0 + j 0.0) as shown in Figure 5-7. Since there was one zero on the right-hand side of the imaginary axis, the system was unstable.

The characteristic equation was also quantified by implementing the muscular dynamics and the mechanical dynamics computed via the bottom-up joint torque. There were five zeros at (-11.9 + j 0.0), (-4.9 + j 0.0), (-2.7 + j 5.7), (-2.7 - j 5.7), and (0.0 + j 0.0) as shown in Figure 5-8. Since one zero was on the imaginary axis (origin), the system was marginally stable.

The parameters for the muscular dynamics and the mechanical dynamics calculated from the top-down joint torque and the bottom-up joint torque produced an unstable system. In a subsequent step, it was identified that the muscular dynamics model calculated from the top-down joint torque and the bottom-up joint torque caused the instability. In addition, also the mechanical dynamics model calculated from the top-down joint torque caused the instability. Therefore, to validate the neural dynamics, the sensorimotor time delay, and the mechanical dynamics (computed using the bottom-up joint torque), we decided to implement a muscular dynamics model from the literature into the simulation model. The muscular dynamics model chosen for the simulation is presented

in Equation (64), where ω was equal to 9.3 $\frac{rad}{sec}$ and β was equal to 1.3 [8]. The poles and the zeros of the characteristic equation using this muscular dynamics model from the literature and the mechanical dynamics (computed using the bottom-up joint torque) are shown in Figure 5-9. There were four zeros at (-8.5 + j 7.9), (-8.5 - j 7.9), (-3.6 + j 5.5), and (-3.6 - j 5.5). Since all the zeros were on the left-hand side of the imaginary axis, the system was stable.
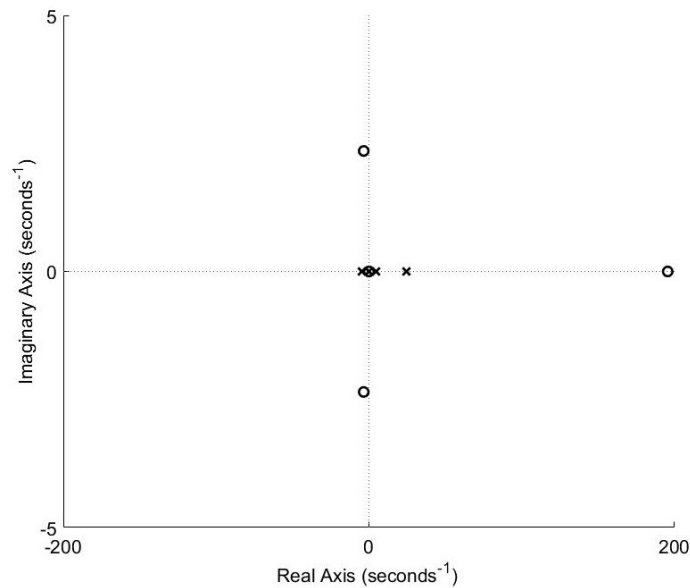
Figure 5-7: Pole-zero plot of the characteristic equation when implementing the mechanical dynamics and the muscular dynamics parameters computed using the top-down joint torque. The zeros are presented as circles, and the poles are presented as crosses.
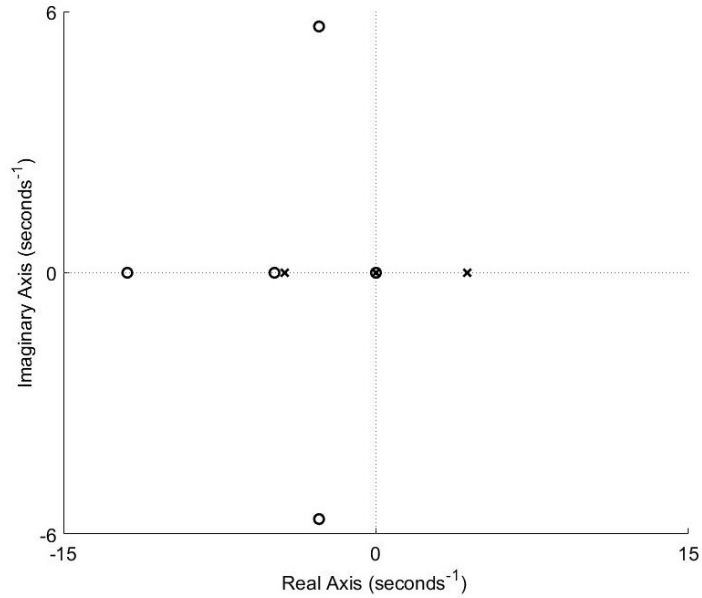
Figure 5-8: Pole-zero plot of the characteristic equation when implementing the mechanical dynamics and the muscular dynamics parameters computed using the bottom-up joint torque. The zeros are presented as circles, and the poles are presented as crosses.
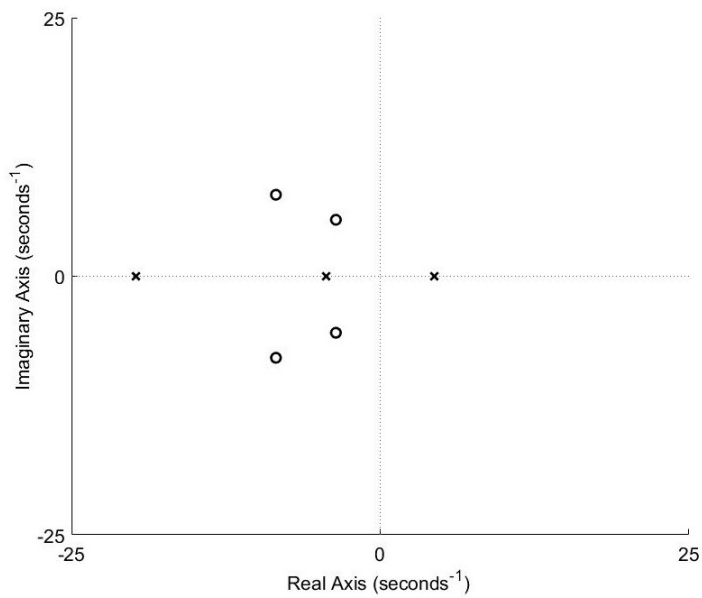
Figure 5-9: Pole-zero plot of the characteristic equation when implementing the muscular dynamics model from the literature [8] and the mechanical dynamics (computed using the bottom-up joint torque). The zeros are presented as circles, and the poles are presented as crosses.

5.5 Simulations

We have implemented the estimated neural dynamics, the sensorimotor time delay, the mechanical dynamics (computed using the bottom-up joint torque), and the muscular dynamics from the literature [8] in a closed-loop model (*see Section 4.8*) for simulations. The GOF and AIC values for fitting the non-parametric estimates of the simulated active controller components to the parametric equations were 97.7 % and 1.7, respectively. The GOF and AIC values for fitting the non-parametric estimates of the simulated active-passive controller components to the parametric equations were 99.5 % and 2.0, respectively. The parameters obtained from the simulations are presented in Table 5-14. The mean relative difference between the simulated and experimental values was small for K_A, D_A, TD, and K_{P2}.

Table 5-14. Summary of the simulation results. The experimental values are compared to the simulation values for each parameter. The mean relative difference (m_d) is presented.

Parameter	Experimental Value	Simulation Value	m_d %
K_A	964.5 (208.1) $\frac{N.m}{rad}$	954.6 $\frac{N.m}{rad}$	1.0
D_A	280.0 (61.9) $\frac{N.m.s}{rad}$	329.6 $\frac{N.m.s}{rad}$	15.0
A_A	27.2 (11.1) $\frac{N.m.s^2}{rad}$	54.3 $\frac{N.m.s^2}{rad}$	50.0
TD	36 (10) ms	37 ms	2.7
K_{P2}	164.5 (72.6) $\frac{N.m.s}{rad}$	195.3 $\frac{N.m.s}{rad}$	15.8

6 Discussion

6.1 Overview

This chapter discusses the adequacy of the methods of the study as well as its results and their significance. First, the adequacy of using the applied system identification for quantifying the mechanisms of seated balance as well as the adequacy and quality of the neuromusculoskeletal time series are discussed. Then, the identified mechanisms of seated balance and the associated parameters are characterized in the context of existing work. Finally, the limitations of this study are presented for consideration in future studies.

6.2 Adequacy of using System Identification to Quantify the Mechanisms of Seated Balance

Extensive research has been performed to understand the mechanisms of balance during postural control. Techniques associated with system identification prove to be a reliable method for quantifying the mechanisms of seated and standing balance [20]. Our results support the conclusion that system identification can be used to robustly quantify the mechanisms of seated balance, and this with reasonable variability across individuals. As previously described (*see Figure 2-1*), the use of system identification requires several choices regarding the feedback control model(s) of human postural balance, the external perturbation characteristics, the neuromusculoskeletal time series, the identification approach, and the fitting and validation criteria. The following sections will demonstrate that the system identification approach implemented in this study – along with associated experimental and methodological choices – can facilitate the quantification of the mechanisms responsible for the control of seated balance.

6.2.1 Feedback Control Models of Human Postural Balance

The utilized feedback control models of human postural balance have varied across studies and depended on the research question being addressed. Past studies have focused on identifying the human body dynamics, neural dynamics, mechanical dynamics, sensory dynamics, muscular dynamics, and sensorimotor time delay in seated and standing balance [8], [17], [20]–[22], [26],

[30], [33]–[35]. In addition, one study had proposed additional feedback (force feedback) in the feedback control model that incorporates the Golgi tendon force feedback dynamics [8]. Previous studies had considered a general framework of postural control balance, where the plant represented the human body dynamics, the controller represented the neural dynamics and the mechanical dynamics, the feedback represented the sensory dynamics, and the time delays represented the sensorimotor time delay. Based on the described body of research, it was decided to adhere to the same methodological choices and their configuration in the present work. In fact, the sequential order of the mechanisms of seated balance was confirmed with the temporal relationships found in this study, as discussed in more detail below.

The small time delay between the external perturbation and body sway (0.00 to 0.04 s) suggested a direct linkage between (1) the external perturbation and (2) the human body and its sway in the feedback control model (Figure 4-1), which was in line with previous studies [8], [20], [22]. The second largest time delay relative to the perturbation was found between the external perturbation and the combined muscle activity ("weighted EMG") (0.10 to 0.23 s). This agrees with the placement of the human body dynamics, sensory dynamics, and neural dynamics between the external perturbation and the weighted EMG in the feedback control model. The largest time delay relative to the perturbation was found between the external perturbation and the joint torque (0.27 to 0.32 s for the top-down joint torque, and 0.26 to 0.50 s for the bottom-up joint torque). This suggests that the placement of the human body dynamics, sensory dynamics, neural dynamics, muscular dynamics, and passive dynamics between the external perturbation and the joint torque in the feedback control model was adequate.

6.2.2 External Perturbation Characteristics

The external perturbation signal was designed to be a persistent excitation signal [22] and to have characteristics recommended and used in the literature. Accordingly, the order of the signal (5,500) was much larger than the maximum order of the mechanisms being identified (4th order). In addition, the body sway evoked by the external perturbation signal had a root-mean-square (RMS) value of approximately 4 degrees, which is four times greater than the RMS of the body sway during quiet sitting (approximately 1 degree; data not reported). This, in turn, suggests that the power of the external perturbation signal was significantly larger than the power of the noise intrinsically present in quiet sitting (e.g., due to breathing and internal movements). As a

consequence, the external perturbation in the feedback control model could be treated as the output noise, allowing us to implement system identification approaches to quantify mechanisms of human sitting control.

6.2.3 Identification Approach

Among the closed-loop system identification approaches, only the indirect approach and the joint input-output approach can provide reliable estimates of the components in a closed-loop control system [20]. In agreement with studies that have reported on non-parametric estimates of the mechanisms involved in *human stance control* [22], [34], [42], the present study chose to implement the joint input-output approach. This approach is particularly recommended when two or more neuromusculoskeletal time series are used. In the present case, time series for the body sway, the weighted EMG, and the joint torque have been reliably identified (*see Section 6.3 below*) using high-quality experimental data together with established theoretical methods.

6.2.4 Fitting and Validation Criteria

The objective cost function implemented in this study to fit the non-parametric estimates with the parametric equations was informed by previous work that also performed the fitting in the frequency domain [240]. As data in the frequency domain can be represented by gain and phase, the fitting criteria can be designed to incorporate fitting for both the gain and phase. This ensures no bias in the fitting procedure, and that the estimated parametric equations can adequately capture the experimental data. The algorithm implemented to optimize the cost function uses a simplex search method, which is a direct method that does not include the use of numerical or analytical gradients [284]. However, the simplex search method cannot guarantee the detection of the global minimum. Therefore, a genetic algorithm was also implemented (data not reported) to verify the results obtained with the simplex search method. In the present study, the two algorithms were found to converge to similar results, confirming the detection of the global minimum. Lastly, the validation criteria implemented in the study (goodness-of-fit, GOF; and Akaike information criteria, AIC) were based on previous studies that used them as their standard evaluation criteria [8], [26], [41].

6.3 Adequacy and Quality of the Neuromusculoskeletal Time Series

To quantify the mechanisms involved in seated balance, it is essential to select appropriate neuromusculoskeletal time series in response to the external perturbations. As argued in the literature, the body sway and activity of relevant muscles can be used to estimate the active controller components [20]. Similarly, the body sway and relevant joint torque can be used to estimate the active-passive controller components [20]. In the following sections, the choices for obtaining these time series are justified and validated.

6.3.1 Body Sway

The orientation of the upper body was obtained using a 'gold standard' marker-based motion capture system. The system was implemented to track the motion of the head-arms-trunk (HAT) segment, the pelvis, and the lower body segments. The accuracy of the body sway estimation via motion capture was affected by the accuracy of anatomical landmark identification use in marker placement [118], [122], [123]. Other potential sources of error include the use of extrapolation to reconstruct missing marker samples and the use of previously reported data to estimate body segment parameters.

The placement locations for the markers were based on similar studies in the past (e.g., [279]) and the Vicon preparation guidelines. Placement sites chosen were bony anatomical landmarks that could be easily identified and that were highly repeatable across participants. All the measures were taken to correctly identify the placement sites of the markers. In addition, the motion capture system's accuracy in identifying a marker's location was approximately 1 mm, which is small compared to the body motion observed in this study. The accuracy of the extrapolation to reconstruct missing marker samples depended on the length of the gap. The shorter in length, the more accurate the reconstruction. Since, in this study, most gaps were shorter than ten frames, spline fill was used to reconstruct the missing markers. In cases where reconstruction through spline fill was not possible due to larger gap sizes, pattern fill was adopted. Both techniques, the spline fill and pattern fill, were able to reconstruct missing marker trajectories with reasonable accuracy (as stated by the manufacturer). The body segment parameters were identified following the procedure described by DeLeva et al. (1996), using the participant's height and weight [117]. Note that the values proposed by DeLeva et al. (1996) were identified via a similar population and are, hence, valid for this study [117]. However, body segment parameters obtained via this method

can still be error-prone. It has been suggested that more accurate body segment parameters could be obtained through the identification of human body dynamics using system identification [20].

In addition to the above considerations, the calculation of body sway required choosing a representative joint for the single-degree of freedom model. In the literature, studies focusing on trunk motion during its flexion/extension have concluded that trunk rotation is most prominent between the fifth lumbar vertebra and the first sacral vertebra [285],[286]. Using the fifth lumbar vertebra as the single-degree of freedom joint as well as the three-dimensional (3D) center of mass (COM) location calculated via motion capture, the body sway in the anterior-posterior direction could be computed.

The body sway of a representative participant (Figure 5-4B) had a range of approximately 10 degrees when subjected to the external perturbation. In a previous study by Audu et al. (2015), this range of body sway was approximately 4 degrees [17]. The difference in the two ranges can be attributed to the difference in perturbation signal amplitude and in the instrumentation used to deliver the perturbation. In studies by Kiemel et al. (2011) and Pasma et al. (2017), the range of body sway in a standing posture was approximately 8 and 2 degrees, respectively [8], [22], when subjected to external perturbations. Thus, the range of body sway obtained in our study was comparable to some of the ranges obtained in past studies on sitting and standing posture. Since body sway obtained in our study was relatively small (<10 degrees), the use of the small angle approximation was justified.

The correlation coefficient (0.29 to 0.61) and the mean squared coherence (0.67 to 0.90) between the body sway and the external perturbation time series indicate substantial similarity between the two signals in both the time and frequency domains. This suggests that the fluctuation in body sway angle is primarily affected by the external perturbation. While other, intrinsic disturbances affect body sway as well, they can be assumed to be negligible in comparison to the external perturbation.

6.3.2   Muscle Activity

Muscle activity was recorded from surface muscles that have been understood to be involved in seated balance [202]–[206], [208], [210], [287]. While the obtained electromyography (EMG) data contained frequency components between 0 and 1,000 Hz, it has been shown that the meaningful frequencies in the EMG data for small motion lies below 10 Hz [72], [210]. Therefore, we chose

a low-pass filter with an appropriate cut-off frequency that was relevant to our purposes. Note that the implemented filtering method and normalization technique were previously applied in other studies (e.g., [210]).

The comparison of the maximum voluntary contractions (MVC) values between left and right muscles had p-values of $p > 0.05$ for all muscles, suggesting that no significant differences were found between left and right MVC values. Similarly, the EMG baseline values for all muscles, except the rectus abdominis and biceps femoris, were not found to be significantly different between corresponding left and right muscles (p-value of $p > 0.05$). The low p-value for the EMG baseline comparison for the rectus abdominis ($p = 0.002$) and the biceps femoris ($p = 0.042$) suggests that differences between the left and right baseline values existed. These differences may be attributed to the fact that, during baseline testing, a few participants exhibited comparably high muscle activity in these muscles for one body side. Small motions of the participant and/or pressing the EMG electrodes against the base of support could be potential reasons for higher EMG activity in these cases.

The EMG data for the twelve muscles were combined into one EMG signal based on the technique described by Kiemel et al. (2008) [34]. The mean weights obtained across all participants were significantly different from zero within a 95% confidence interval. In the literature, the rectus abdominis (RA) and external obliques (EO) are involved in trunk stabilization during sudden backward movement, whereas the erector spinae are involved in trunk stabilization during sudden forward movement [210]. Since we obtained large weights for RA, EO, the erector spinae at the ninth thoracic vertebra, and the erector spinae at the third lumbar vertebra, these muscles' contributions may be fundamental in the trunk stabilization process. The two lower limb muscles (biceps femoris and rectus femoris), which were indirectly involved in trunk stabilization by stabilizing the pelvis, exhibited lower weights compared to the other muscles. The lower weights might correspond to a lower relative contribution of these muscles to the trunk stabilization process. One reason may be that the lower amplitude of the external perturbation might not demand higher activities in the leg muscles.

The weighted, normalized muscle activity shown in Figure 5-4C had a magnitude between –1 and 1% of MVC. It has been reported in past studies that the effect of the used normalization technique could be seen only in the gain of the estimated frequency response function [34]. Therefore, during

the parametric identification of the active controller components, a normalization constant was added to the parametric equation to remove the effect of normalization from the estimated parameters [34].

The correlation coefficient (0.35 to 0.68) and the mean squared coherence (0.37 to 0.69) between the weighted EMG and the external perturbation time series indicate substantial similarity between the two signals in both the time and frequency domains. This suggests that the activity in the studied trunk and leg muscles is primarily caused by the external perturbation. While other, intrinsic disturbances can affect the muscles' activity, they can be assumed to be negligible in comparison to the external perturbation.

6.3.3   Joint Torque

The joint torque was used in the past to quantify the mechanisms of standing balance using system identification techniques. However, none of the existing studies had used the joint torque for quantifying the mechanisms of seated balance. One reason may be associated with the error that accompanies joint torque calculations in general [154], [155]. In this research, the joint torque was computed using top-down and bottom-up inverse dynamics, and the mechanisms obtained from both approaches were compared.

6.3.3.1   Top-Down Inverse Dynamics Approach

The top-down inverse dynamics approach required the body segment parameters and the body's orientation over time (i.e., body sway angle) to estimate the joint torque ("top-down joint torque"). The accuracy of the body segment parameters and of the body sway angle have previously been discussed (*see Section 6.3.1*). One challenge with the top-down inverse dynamics approach is that it can amplify high-frequency noise in the results due to calculating angular acceleration from the body sway time series.

The top-down joint torque shown in Figure 5-4D had a magnitude between –90 and 85 N·m. The joint torque of the upper body required to compensate for the torque due to gravity (for body sway of up to 10 degrees), due to the external disturbance, and due to the inertia of the upper body was approximately 40 N·m, 20 N·m, and 40 N·m, respectively. Therefore, the range of the computed top-down joint torque agrees with the range that was required to stabilize the upper body.

The correlation coefficient (–0.75 to –0.53) and the mean squared coherence (0.71 to 0.91) between the top-down joint torque and the external perturbation time series indicate substantial similarity between the two signals in both the time and frequency domains. This suggests that the top-down joint torque was generated mostly due to the external perturbation. While other, intrinsic disturbances can affect the top-down joint torque, they can be assumed to be negligible in comparison to the external perturbation.

6.3.3.2 Bottom-up Inverse Dynamics Approach

The bottom-up inverse dynamics approach required the estimation of the forces and moment arms in the relevant directions to calculate the joint torque ("bottom-up joint torque"). In this study, the forces were obtained from the force plate, and the moment arms were obtained via the force plate and motion capture system. The accuracy of the force plate data was discussed previously (*see Section 4.4*).

The top-down joint torque as shown in Figure 5-4D had a magnitude between –90 and 85 N·m, and the bottom-up joint torque as shown in Figure 5-4E had a magnitude between -9 and 13 N·m. Similar differences between the magnitudes of the top-down and the bottom-up joint torques were observed in past studies, which were attributed to the (in)accuracy in the body segment parameters and potential offsets in the center of pressure location [154].

The correlation coefficient (–0.61 to –0.17) and the mean squared coherence (0.61 to 0.90) between the bottom-up joint torque and the external perturbation signal indicate substantial similarity between the two signals in the time and frequency domains. This suggests that the bottom-up joint torque was mostly generated due to the external perturbation. Other intrinsic disturbances effect on the bottom-up joint torque were present. While other, intrinsic disturbances can affect the bottom-up joint torque, they can be assumed to be negligible in comparison to the external perturbation.

6.4 Quantification of the Mechanisms of Seated Balance

Non-parametric and parametric estimates of the mechanisms of seated balance were obtained in this study. The non-parametric estimates exhibited low variability across participants, and the parametric estimates were stable as verified by the stability analysis.

6.4.1   Non-Parametric Estimates

6.4.1.1   Active Controller Components

The frequency response function (FRF) of the active controller components shown in Figure 5-5A and 5-5B consisted of the neural dynamics and the sensorimotor time delay. The trend in the gain of the frequency response suggested neural dynamics consistent with proportional-derivative (PD) control [21], [22], [178]. The saturation in the phase of the frequency response implied the presence of a time delay in the active feedback loop. The fact that the phase in the active control component settled at approximately 110 degrees suggested a deviation from PD control, which indicated the presence of higher-order terms in the neural dynamics.

A previous study identifying the active feedback component for upright stance computed the open-loop FRF between the trunk segment angles and the weighted EMG signals of the hip and ankle muscles. The gain and phase of the frequency response were almost constant for lower frequencies. With increasing frequency, also the gain and phase increased. The phase reached a maximum of approximately 100 degrees at a frequency of 1.2 Hz, and fell for higher frequencies [22]. In another study from the same group that identified the postural control system, the open-loop FRF between the trunk segment angles and the weighted EMG signals of the hip and lower trunk muscles were computed. Similar trends in the gain and phase of the FRF were obtained as in the present study [42].

By comparing the non-parametric estimates of the active controller components between standing and sitting balance, it is possible to assess, and quantify, the similarities and differences in the active control strategy between the two postures. In both sitting and standing, the brain relies on the body's displacement and velocity information in the active feedback loop. Since this loop is affected by a time delay for both standing and seated posture, active feedback control is not an instantaneous mechanism, but one that takes time to execute. The presence of additional, higher-order terms in both standing and seated balance further supports the notion that commonalities exist between these two control applications.

6.4.1.2   Active-Passive Controller Components

The FRF of the active-passive controller components, obtained via the top-down and bottom-up joint torques are shown in Figure 5-5C to 5-5F. The active-passive controller components consisted of the neural dynamics, the mechanical dynamics, the muscular dynamics, and the

sensorimotor time delay. The trend in the gain of the frequency response of the active-passive control components suggested feedback control consistent with PD control. The saturation in the phase of the frequency response of the active-passive control components implied the presence of a time delay in the feedback loop. The higher gain, compared to the FRF of the active control component, suggests the presence of passive feedback control. The phase of the frequency response obtained from the top-down joint torque remained almost constant at 180 degrees, suggesting that the joint torque was consistently out of phase with the body sway. This result agrees with the fact that the joint torque is generated to counter the body sway movement [20]. The frequency response obtained from the bottom-up joint torque had an almost constant phase of 180 degrees for lower frequencies, agreeing with the frequency response results for the top-down joint torque. However, for higher frequencies, the phase of the frequency response for the bottom-up joint torque increased steadily, suggesting the presence of higher-order terms.

Based on the literature reviewed in this study, no previous study has reported the frequency response of the active-passive control components in seated and standing balance. As mentioned earlier, this may be due to errors associated with the estimation of joint torques [154]. The authors recommend more research into the estimation of joint torques, for the purpose of accurate quantification of the active-passive controller components.

6.4.2   Parametric Estimates

The high GOF and low AIC values suggest the identified parametric models of the active and active-passive control components fit the non-parametric estimates well. The high variance-accounted-for (VAF) for the active-passive control components indicate adequate prediction of the top-down joint torque from body sway. The VAF for the active controller components was not high, possibly due to the noise in the EMG data that cannot be accounted for by linear functions implemented in this study. Similarly, the VAF of the active-passive controller components calculated via the bottom-up joint torque is not high, possibly due to the noise in the center of pressure measurements that cannot be accounted for by linear functions implemented in this study. To account for noise, advanced model fitting techniques, e.g., stochastic or non-linear modelling, may be needed.

6.4.2.1 Neural Dynamics

The neural dynamics were identified as a PD controller with acceleration feedback. Previous work on standing and sitting balance has modelled the neural dynamics using a proportional-integrative-derivative (PID) or PD controller [17], [189]. The additional acceleration feedback and the absence of integral feedback in the neural dynamics have been reported by another study [8]. In line with past efforts, the use of a proportional and derivative term suggests that the body's displacement and velocity information is critical for maintaining balance. The use of acceleration feedback suggests a strong consideration of the body's inertia when humans maintain balance [192], [193].

Pasma et al. (2017) obtained mean values of 908.2 $\frac{N \cdot m}{rad}$, 591.7 $\frac{N \cdot m \cdot s}{rad}$, and 89.1 $\frac{N \cdot m \cdot s^2}{rad}$ for the proportional, derivative, and acceleration feedback constants, respectively [8]. Peterka et al. (2002) obtained proportional and derivative constants within the ranges of 859 to 1432 $\frac{N \cdot m}{rad}$ and 286 to 573 $\frac{N \cdot m \cdot s}{rad}$, respectively [21]. As such, the parameter values obtained in the present study were similar to the abovementioned results. However, the values obtained by Audu et al. (2015) were quite different than the present results [17], possibly due to the difference in model fitting procedure.

6.4.2.2 Sensorimotor Time Delay

The sensorimotor time delay was identified as an exponential decay function, which was in agreement with findings of previous studies [8], [17], [20], [22], [26]. The mean value of the sensorimotor delay obtained by Pasma et al. (2017) was 0.10 s [8]. The sensorimotor delay obtained by Peterka et al. (2002) was in the range of 0.10 to 0.25 s [21], whereas Audu et al. (2015) reported a range of 0.10 to 0.15 s [17]. As sitting balance requires shorter times than standing balance to transfer information from the sensory systems to the brain and from the brain to the muscles, it is reasonable that the delay obtained in this study was shorter (0.036 s).

6.4.2.3 Mechanical Dynamics

The mechanical dynamics were identified as a PD controller and a proportional controller using the top-down and bottom-up joint torques, respectively. In the subsequent stability analysis, it was found, however, that the PD controller produced an unstable system, which was further verified in the simulations. The proportional controller produced a stable system when combined with the

muscular dynamics reported in the literature (see below). This combination was used for further analyses.

The mean values for the proportional constant, as obtained by Pasma et al. (2017), Peterka et al. (2002), and Audu et al. (2015), were 94.4 $\frac{N \cdot m}{rad}$, 1.6 $\frac{N \cdot m}{rad}$, and 3.0 $\frac{N \cdot m}{rad}$, respectively [8], [17], [21]. The proportional constant reported in our study (164.5 $\frac{N \cdot m}{rad}$) was higher than the above values that were reported for the standing posture. This may be due to the difference in standing and sitting postures, considering that sitting posture is understood to be more stable and stiffer than standing posture [29]. The non-identification of the derivative term in the mechanical dynamics could be due to the low power in the lower frequency content (< 0.1 Hz) of the external perturbation signal that was not able to excite all the relevant characteristics of the mechanical dynamics. It should also be noted that past studies have reported a small value for the derivative constant (< 5 $\frac{N \cdot m \cdot s}{rad}$); hence, a similarly small value may have not been captured in the model fitting.

6.4.2.4 Muscular Dynamics

The muscular dynamics calculated from the active-passive controller estimates via the top-down and bottom-up joint torques had a second- and third-order transfer function, respectively. Similarly, past studies have identified the muscular dynamics as a second-order critically damped system [8], [240], [242]. In the stability analysis, the muscular dynamics obtained via both the top-down and bottom-up joint torques produced, however, an unstable system, which was further confirmed in the simulations. Therefore, in the subsequent analysis, a second-order critically damped system reported in the literature was used as the muscular dynamics.

Both the top-down and bottom-up joint torques were not able to yield stable muscular dynamics. In fact, the muscular dynamics may not have been identified correctly due to errors in the joint torque estimation (*see Section 6.3.3*). One solution may be to use better optimization techniques (as described in [154]) to obtain more correct estimates of the joint torque and, in turn, identify the active-passive controller components for better prediction of the muscular dynamics.

6.5   Robustness of the Obtained Parameters

The neural dynamics, the sensorimotor time delay, and the mechanical dynamics identified in this study, along with the muscular dynamics reported in the literature, were implemented in a closed-loop feedback model (Figure 4-13) in Simulink. The model produced, when used in simulations, a stable response for the estimated models of the neural dynamics, the sensorimotor time delay, and the mechanical dynamics. The high GOF and low AIC values suggest an excellent fit of the parametric equations to the non-parametric estimates of the simulated active and active-passive controller components. The low mean relative differences for K_A, D_A, TD, and K_{P2} suggest that the experimentally estimated parameters were robust. The high mean relative differences for A_A suggest the need for further work when estimating this parameter.

6.6   Limitations of the Thesis Research

The performed research had a number of limitations in the methodology and processing of the data. Human motion tracking when using marker-based motion capture is affected by variations in marker placement. Accuracy in locating the bony landmarks and placing the markers on the same location across participants required intense practicing. While the experimenters were well trained before placing the markers, perfect accuracy in placing the markers cannot be achieved. The EMG electrodes used in this study were surface electrodes that can register electrical activity from nearby muscles or other sources. More accurate measurements of muscle activity can be obtained via other types of electrodes, e.g., indwelling electrodes. However, these techniques are invasive and are accompanied by other limitations. Each participant's weight acquired by self-reporting may be affected by errors, which can be eliminated by measuring each participant's weight in the actual experiments (e.g., via a scale or the force plate).

The joint torque estimation using both top-down and bottom-up inverse dynamics was prone to errors. The top-down inverse dynamics approach was primarily affected by inaccuracies in the body segment parameters. However, there is no direct measure to identify body segment parameters in living humans. The bottom-up inverse dynamics approach was primarily affected by biases in the center of pressure estimation. The combination of the EMG measurements into a single muscle activity signal can lead to an underrepresentation of some muscles, which may

negatively impact the estimation of the neural dynamics. Single-input-multiple-output models can be adapted to ensure equal representation of each muscle in the neural dynamics estimation.

As mentioned above, the neuromusculoskeletal time series included errors that propagate within the estimations of the active and active-passive controller components. The uncertainty in the joint torque identification can lead to unreliable estimates of the muscular and mechanical dynamics. More reliable estimates of the muscular and mechanical dynamics can be obtained by including sensory noise in the identification process [20].

7 Conclusion

The ability to balance the upper body during sitting is required to perform activities of daily living and to counteract internal and external disturbances. Individuals affected by seated imbalance can benefit from therapies and targeted interventions. However, suggesting an optimal therapy or intervention that facilitates speedy recovery of affected individuals is challenging. Motivated by the need to optimize existing therapies and interventions based on a mechanistic understanding of the severity of seated imbalance, this work set out to quantify the control mechanisms of seated balance in non-disabled individuals. The obtained knowledge can shed light on the neuromechanical control structure and associated components used to stabilize the upper body during sitting. Furthermore, it can be used as a normative benchmark for assessing individuals with balance impairments, with the aim of optimizing therapies and targeted interventions.

In this study, the control mechanisms of seated balance were quantified using system identification. The active controller components provided estimates of the neural dynamics and the sensorimotor time delay, whereas the active-passive controller components provided estimates of the mechanical dynamics and muscular dynamics. The low across-participant variability of the non-parametric estimates of the active and active-passive control components implies reliability of the proposed method to quantify seated balance control. On the one hand, the non-parametric estimates of the active controller components suggest neural dynamics consistent with a proportional-derivative controller that are furthermore affected by a sensorimotor time delay. On the other hand, the non-parametric estimates of the active-passive controller components suggest a phase reversal between the body sway and joint torque, as well as the presence of passive feedback in the control loop.

The parametric, active control estimates indicate that the brain utilizes the body's displacement, velocity, and acceleration information to control seated balance, whereas the parametric, passive control estimates indicate that the body's mechanical contributions to the control goal are linked to the body's displacement. Furthermore, active control was found to be delayed, whereas passive control occurred instantaneously.

The models of the neural dynamics, the mechanical dynamics, and the sensorimotor time delay produce a stable response in the closed-loop system. In other words, using the identified models of the control mechanisms of seated balance, one can stabilize a single-link inverted pendulum subjected to gravity and external disturbances. Since upper body dynamics can be approximated by the dynamics of a single-link inverted pendulum, the identified control mechanisms can be thought to stabilize the upper body as well. However, further research is required to test the efficacy of the identified control mechanisms in stabilizing the human upper body.

Having obtained parametric estimates of the neural dynamics, the mechanical dynamics, and the sensorimotor time delay in non-disabled individuals, we will be able to quantify and, particularly characterize, the mechanisms of seated balance in impaired populations. It is expected that affected individuals will demonstrate deviations from the obtained parameters. Associated insights can be used to specifically target the identified mechanisms in the affected individuals. In this light, the presented work has made significant contributions toward a mechanistic understanding of the mechanisms of seated balance, such that the insights can be used in future, clinically relevant applications.

7.1 Recommendation for Future Work

In a fundamental context, one focus of future work could be on assessing the reliability of the obtained parameters using another, larger sample of non-disabled individuals. Also, our fundamental knowledge on seated balance control could be further advanced by estimating reliable estimates of the muscular dynamics, sensory dynamics, and human body dynamics in non-disabled individuals using the described system identification techniques.

In a more clinical context, the parameters obtained in this work should be characterized in comparison to those obtained in the elderly or a population affected by trunk instability (e.g., stroke survivors). Such comparison would provide us with more insights into the seated balance control mechanisms of both non-disabled and disabled individuals. It should also be noted that the control mechanisms obtained in this study are restricted to seated balance in the anterior-posterior direction. Seated balance in other directions (e.g., medio-lateral direction) could be assessed, for the purpose of assessing overall trunk stabilization. Finally, wearable technologies (e.g., inertial

measurement units or wireless electromyography) could be used instead of laboratory equipment to develop feasible out-of-lab assessment protocols for the clinical context.

In a third domain, the results obtained in this work could be used to develop assistive technologies, particularly closed-loop control schemes for delivering functional electrical stimulation (FES). The neural dynamics obtained in this research may provide controller gain estimates mimicking physiological behavior that could reduce fatigue in FES applications for trunk control. However, before applying the presented findings in an FES system, more experimental research involving FES is required.

References

[1]   D. Engelhart *et al.*, "Impaired Standing Balance in Elderly: A New Engineering Method Helps to Unravel Causes and Effects," *J. Am. Med. Dir. Assoc.*, vol. 15, no. 3, 2014.

[2]   A. S. Pollock, B. R. Durward, and P. J. Rowe, "What is balance?," vol. 14, no. October 1999, pp. 402–406, 1999.

[3]   G. B. Andersson and J. M. Winters, "Role of muscle in postural tasks: spinal loading and postural stability," *Mult. muscle Syst. Biomech. Mov. Organ.*, pp. 377–395, 1990.

[4]   H. A. M. M. Seelen, Y. J. M. M. Potten, A. Huson, F. Spaans, and J. P. H. H. Reulen, "Impaired balance control in paraplegic subjects," *J. Electromyogr. Kinesiol.*, vol. 7, no. 2, pp. 149–160, 1997.

[5]   I. A. F. Stokes, M. Gardner-Morse, S. M. Henry, and G. J. Badger, "Decrease in trunk muscular response to perturbation with preactivation of lumbar spinal musculature," *Spine (Phila. Pa. 1976).*, vol. 25, no. 15, pp. 1957–1964, 2000.

[6]   S. M. McGill, S. Grenier, N. Kavcic, and J. Cholewicki, "Coordination of muscle activity to assure stability of the lumbar spine," *J. Electromyogr. Kinesiol.*, vol. 13, pp. 353–359, 2003.

[7]   J. J. Crisco, M. M. Panjabi, I. Yamamoto, and T. R. Oxland, "Euler stability of the human ligamentous lumbar spine. Part II: Experiment," *Clin. Biomech.*, 1992.

[8]   J. H. Pasma, J. Van Kordelaar, D. De Kam, V. Weerdesteyn, A. C. Schouten, and H. Van Der Kooij, "Assessment of the underlying systems involved in standing balance: The additional value of electromyography in system identification and parameter estimation," *J. Neuroeng. Rehabil.*, vol. 14, no. 1, pp. 1–17, 2017.

[9]   F. B. Horak, C. L. Shupert, and A. Mirka, "Components of postural dyscontrol in the elderly: A review," *Neurobiology of Aging*, vol. 10, no. 6. pp. 727–738, 1989.

[10]   D. L. Sturnieks, R. St George, and S. R. Lord, "Balance disorders in the elderly," *Neurophysiologie Clinique*, vol. 38, no. 6. pp. 467–478, 2008.

[11]   D. Manchester, M. Woollacott, N. Zederbauer-Hylton, and O. Marin, "Visual, Vestibular and Somatosensory Contributions to Balance Control in the Older Adult," *J. Gerontol.*, vol.

44, no. 4, pp. M118–M127, 1989.

[12] L. Nyberg and Y. Gustafson, "Patient Falls in Stroke Rehabilitation," *Stroke*, vol. 26. pp. 838–842, 1995.

[13] K. D. Anderson, "Targeting Recovery: Priorities of the Spinal Cord-Injured Population," *J. Neurotrauma*, vol. 21, no. 10, pp. 1371–1383, 2004.

[14] N. Hart *et al.*, "Respiratory effects of combined truncal and abdominal support in patients with spinal cord injury," *Arch. Phys. Med. Rehabil.*, vol. 86, no. 7, pp. 1447–1451, 2005.

[15] M. Alm, E. Gutierrez, C. Hultling, and H. Saraste, "Clinical evaluation of seating in persons with complete thoracic spinal cord injury.," *Spinal Cord*, vol. 41, no. 10, pp. 563–571, 2003.

[16] M. L. Audu, L. M. Lombardo, J. R. Schnellenberger, K. M. Foglyano, M. E. Miller, and R. J. Triolo, "A neuroprosthesis for control of seated balance after spinal cord injury.," *J. Neuroeng. Rehabil.*, vol. 12, no. 1, p. 8, 2015.

[17] M. L. Audu and R. J. Triolo, "Intrinsic and extrinsic contributions to seated balance in the sagittal and coronal planes: Implications for trunk control after spinal cord injury," *J. Appl. Biomech.*, vol. 31, no. 4, pp. 221–228, 2015.

[18] N. Y. Harel, P. K. Asselin, D. B. Fineberg, T. J. Pisano, W. A. Bauman, and A. M. Spungen, "Adaptation of computerized posturography to assess seated balance in persons with spinal cord injury," *J. Spinal Cord Med.*, vol. 36, no. 2, pp. 127–133, 2013.

[19] R. J. Triolo, S. N. Bailey, M. E. Miller, L. M. Lombardo, and M. L. Audu, "Effects of stimulating hip and trunk muscles on seated stability, posture, and reach after spinal cord injury," *Arch. Phys. Med. Rehabil.*, vol. 94, no. 9, pp. 1766–1775, 2013.

[20] H. Van Der Kooij, E. Van Asseldonk, and F. C. T. Van Der Helm, "Comparison of different methods to identify and quantify balance control," *J. Neurosci. Methods*, vol. 145, no. 1–2, pp. 175–203, 2005.

[21] R. J. Peterka *et al.*, "Sensorimotor Integration in Human Postural Control," *J. Neurophysiol.*, vol. 88, no. 3, pp. 1097–1118, 2002.

[22] T. Kiemel, Y. Zhang, and J. J. Jeka, "Identification of neural feedback for upright stance in humans: stabilization rather than sway minimization.," *J. Neurosci.*, vol. 31, no. 42, pp. 15144–53, 2011.

[23] M. Freddolini, S. Strike, and R. Y. W. Lee, "The role of trunk muscles in sitting balance control in people with low back pain," *J. Electromyogr. Kinesiol.*, vol. 24, no. 6, pp. 947–

953, 2014.

[24] P. J. Lee, E. L. Rogers, and K. P. Granata, "Active trunk stiffness increases with co-contraction," *J. Electromyogr. Kinesiol.*, vol. 16, no. 1, pp. 51–57, 2006.

[25] R. A. Preuss, S. G. Grenier, and S. M. McGill, "Postural control of the lumbar spine in unstable sitting," *Arch. Phys. Med. Rehabil.*, vol. 86, no. 12, pp. 2309–2315, 2005.

[26] A. H. Vette, K. Masani, K. Nakazawa, M. R. Popovic, and S. S. S. S. Member, "Neural-Mechanical Feedback Control Scheme Fluctuation During Quiet Stance," *Rehabilitation*, vol. 18, no. 1, pp. 86–95, 2010.

[27] N. Genthon, N. Vuillerme, J. P. Monnet, C. Petit, and P. Rougier, "Biomechanical assessment of the sitting posture maintenance in patients with stroke," *Clin. Biomech.*, vol. 22, no. 9, pp. 1024–1029, 2007.

[28] S. Perlmutter, F. Lin, and M. Makhsous, "Quantitative analysis of static sitting posture in chronic stroke," *Gait Posture*, vol. 32, no. 1, pp. 53–56, 2010.

[29] A. H. Vette, K. Masani, V. Sin, and M. R. Popovic, "Posturographic measures in healthy young adults during quiet sitting in comparison with quiet standing," *Med. Eng. Phys.*, vol. 32, no. 1, pp. 32–38, 2010.

[30] D. Engelhart, T. A. Boonstra, R. G. K. M. Aarts, A. C. Schouten, and H. Van Der Kooij, "Comparison of closed-loop system identification techniques to quantify multi-joint human balance control," *Annu. Rev. Control*, vol. 41, pp. 58–70, 2016.

[31] L. Ljung, "System Identification," pp. 163–173, 1998.

[32] R. E. Kearney and I. W. Hunter, "System Identification of Human Joint Dynamics," *Crit. Rev. Biomed. Eng.*, vol. 18, no. 1, pp. 55–87, 1990.

[33] J. H. Pasma *et al.*, "Assessing Standing Balance using MIMO Closed Loop System Identification Techniques," *IFAC-PapersOnLine*, vol. 48–28, no. 28, pp. 1381–1385, 2015.

[34] T. Kiemel, A. J. Elahi, and J. J. Jeka, "Identification of the plant for upright stance in humans: multiple movement patterns from a single neural strategy.," *J. Neurophysiol.*, vol. 100, no. 6, pp. 3394–406, 2008.

[35] R. J. Peterka, P. J. Loughlin, R. J. Peterka, and P. J. Loughlin, "Dynamic Regulation of Sensorimotor Integration in Human Postural Control," pp. 410–423, 2010.

[36] A. D. Goodworth and R. J. Peterka, "Contribution of Sensorimotor Integration to Spinal Stabilization in Humans," *J. Neurophysiol.*, vol. 102, no. 1, pp. 496–512, 2009.

[37] H. Van Der Kooij and R. J. Peterka, "Non-linear stimulus-response behavior of the human stance control system is predicted by optimization of a system with sensory and motor noise," *J. Comput. Neurosci.*, vol. 30, no. 3, pp. 759–778, 2011.

[38] K. Masani, "Importance of Body Sway Velocity Information in Controlling Ankle Extensor Activities During Quiet Stance," *J. Neurophysiol.*, vol. 90, no. 6, pp. 3774–3782, 2003.

[39] T. A. Boonstra, A. C. Schouten, and H. van der Kooij, "Identification of the contribution of the ankle and hip joints to multi-segmental balance control," *J. Neuroeng. Rehabil.*, vol. 10, no. 1, p. 23, 2013.

[40] H. M. Schepers, E. H. F. Van Asseldonk, J. H. Buurke, B. F. J. M. Koopman, and P. H. Veltink, "Ambulatory assessment of balance," *Proc. 2nd Bienn. IEEE/RAS-EMBS Int. Conf. Biomed. Robot. Biomechatronics, BioRob 2008*, pp. 39–42, 2008.

[41] D. Engelhart, A. C. Schouten, R. G. K. M. K. M. Aarts, and H. Van Der Kooij, "Assessment of Multi-Joint Coordination and Adaptation in Standing Balance: A Novel Device and System Identification Technique," *IEEE Trans. Neural Syst. Rehabil. Eng.*, vol. 23, no. 6, pp. 973–982, 2015.

[42] S. Hwang, P. Agada, T. Kiemel, and J. J. Jeka, "Identification of the Unstable Human Postural Control System," *Front. Syst. Neurosci.*, vol. 10, 2016.

[43] "Chapter 5: Foundations of Methods for Computing Eigenvalues," in *Eigenvalues of Matrices*, Society for Industrial and Applied Mathematics, 2012, pp. 205–249.

[44] H. Akaike, "A new look at the statistical model identification," *IEEE Trans. Autom. Control*, vol. 19, no. 6, pp. 716–723, 1974.

[45] U. Forssell, *Closed-loop Identification: Methods , Theory , and Applications*, no. 566. 1999.

[46] A. Procházka, J. Uhlíř, P. J. W. Rayner, and N. G. Kingsbury, *Signal Analysis and Prediction*. 1998.

[47] L. Ljung, *System Identification: Theory for User*, vol. 11, no. 3. 1987.

[48] D. M. Kado, K. Prenovost, and C. Crandall, "Narrative review: Hyperkyphosis in older persons," *Annals of Internal Medicine*. 2007.

[49] T. S. Keller, D. E. Harrison, C. J. Colloca, D. D. Harrison, and T. J. Janik, "Prediction of osteoporotic spinal deformity," *Spine (Phila. Pa. 1976).*, 2003.

[50] L. E. Edsberg, J. M. Black, M. Goldberg, L. McNichol, L. Moore, and M. Sieggreen, "Revised National Pressure Ulcer Advisory Panel Pressure Injury Staging System," *J.*

Wound, Ostomy Cont. Nurs., 2016.

[51] C. Roussos and A. Koutsoukou, "Respiratory failure.," *Eur. Respir. J. Suppl.*, 2003.

[52] S. Bouisset and M. Zattara, "A sequence of postural movements precedes voluntary movement," *Neurosci. Lett.*, vol. 22, no. 3, pp. 263–270, 1981.

[53] J. Massion, "Movement, posture and equilibrium: Interaction and coordination," *Progress in Neurobiology*, vol. 38, no. 1. pp. 35–56, 1992.

[54] S.-H. Yeo, D. W. Franklin, and D. M. Wolpert, "When Optimal Feedback Control Is Not Enough: Feedforward Strategies Are Required for Optimal Control with Active Sensing," *PLOS Comput. Biol.*, vol. 12, no. 12, p. e1005190, 2016.

[55] S. Mohapatra, K. K. Kukkar, and A. S. Aruin, "Support surface related changes in feedforward and feedback control of standing posture," *J. Electromyogr. Kinesiol.*, vol. 24, no. 1, pp. 144–152, 2014.

[56] F. B. Horak, "Postural orientation and equilibrium: What do we need to know about neural control of balance to prevent falls?," in *Age and Ageing*, 2006, vol. 35, no. SUPPL.2.

[57] J. M. Macpherson, J. Fung, and R. Jacobs, "Postural orientation, equilibrium, and the spinal cord.," *Adv. Neurol.*, vol. 72, pp. 227–32, 1997.

[58] R. C. Miall and D. M. Wolpert, "Forward models for physiological motor control," *Neural Networks*. 1996.

[59] R. R. Flanagan, P. Vetter, R. S. Johansson, and D. M. Wolpert, "Prediction precedes control in motor learning," *Curr. Biol.*, 2003.

[60] M. Kawato, "Internal models for motor control and trajectory planning," *Current Opinion in Neurobiology*. 1999.

[61] A. H. Vette, E. Sanin, A. Bulsen, A. Morris, K. Masani, and M. R. Popovic, "A Portable and Automated Postural Perturbation System for Balance Assessment, Training, and Neuromuscular System Identification," *J. Med. Device.*, vol. 2, no. 4, p. 041007, 2008.

[62] H. Forssberg and H. Hirschfeld, "Postural adjustments in sitting humans following external perturbations: muscle activity and kinematics," *Exp. Brain Res.*, vol. 97, no. 3, pp. 515–527, 1994.

[63] T. Komura, Y. Shinagawa, and T. L. Kunii, "A muscle-based feed-forward controller of the human body," *Comput. Graph. Forum*, 1997.

[64] S. P. Silfies, R. Mehta, S. S. Smith, and A. R. Karduna, "Differences in Feedforward Trunk

Muscle Activity in Subgroups of Patients With Mechanical Low Back Pain," *Arch. Phys. Med. Rehabil.*, 2009.

[65] M. E. Tinetti, "Performance-Oriented Assessment of Mobility Problems in Elderly Patients," *J. Am. Geriatr. Soc.*, vol. 34, no. 2, pp. 119–126, 1986.

[66] K. O. Berg, S. L. Wood-Dauphinee, J. I. Williams, and B. Maki, "Measuring balance in the elderly: Validation of an instrument," in *Canadian Journal of Public Health*, 1992, vol. 83, no. SUPPL. 2.

[67] A. Nieuwboer, H. Feys, W. De Weerdt, G. Nuyens, and E. De Corte, "Developing a Clinical Tool to Measure Sitting Balance after Stroke: A reliability study," *Physiotherapy*, vol. 81, no. 8, pp. 439–445, 1995.

[68] S. E. Fife, L. A. Roxborough, R. W. Armstrong, S. R. Harris, J. L. Gregson, and D. Field, "Development of a clinical measure of postural control for assessment of adaptive seating in children with neuromotor disabilities," *Physical Therapy*, vol. 71, no. 12. pp. 981–993, 1991.

[69] U. Hohtari-Kivimäki, M. Salminen, T. Vahlberg, and S. L. Kivelä, "Short Berg Balance Scale, BBS-9, as a predictor of fall risk among the aged: A prospective 12-month follow-up study," *Aging Clin. Exp. Res.*, vol. 25, no. 6, pp. 645–650, 2013.

[70] K. M. Guskiewicz and D. H. Perrin, "Research and clinical applications of assessing balance," *J. Sport Rehabil.*, vol. 5, no. 51, pp. 45–63, 1996.

[71] J. E. Visser, M. G. Carpenter, H. van der Kooij, and B. R. Bloem, "The clinical utility of posturography," *Clinical Neurophysiology*, vol. 119, no. 11. pp. 2424–2436, 2008.

[72] D. A. Winter, *Biomechanics and Motor Control of Human Movement*, vol. 2nd. 2009.

[73] T. E. Prieto, J. B. Myklebust, R. G. Hoffmann, E. G. Lovett, and B. M. Myklebust, "Measures of postural steadiness: Differences between healthy young and elderly adults," *IEEE Trans. Biomed. Eng.*, vol. 43, no. 9, pp. 956–966, 1996.

[74] M. Duarte and S. M. Freitas, "Revision of posturography based on force plate for balance evaluation," *Rev. Bras. Fisioter.*, vol. 14, no. 3, pp. 183–192, 2010.

[75] H. Chaudhry, B. Bukiet, Z. Ji, and T. Findley, "Measurement of balance in computer posturography: Comparison of methods-A brief review," *J. Bodyw. Mov. Ther.*, vol. 15, no. 1, pp. 82–91, 2011.

[76] J. J. Collins and C. J. De Luca, "Open-loop and closed-loop control of posture: A random-

walk analysis of center-of-pressure trajectories," *Exp. Brain Res.*, vol. 95, no. 2, pp. 308–318, 1993.

[77] K. H. Sienko, M. D. Balkwill, L. I. E. Oddsson, and C. Wall, "Effects of multi-directional vibrotactile feedback on vestibular-deficient postural performance during continuous multi-directional support surface perturbations.," *J. Vestib. Res.*, vol. 18, pp. 273–285, 2008.

[78] D. G. Sayenko *et al.*, "Positive effect of balance training with visual feedback on standing balance abilities in people with incomplete spinal cord injury," *Spinal Cord*, vol. 48, no. 12, pp. 886–893, 2010.

[79] G. K. Hyun, J. B. Dingwell, H. G. Kang, and J. B. Dingwell, "A direct comparison of local dynamic stability during unperturbed standing and walking," *Exp. Brain Res.*, vol. 172, no. 1, pp. 35–48, 2006.

[80] M. Grangeon, D. Gagnon, C. Gauthier, G. Jacquemin, K. Masani, and M. R. Popovic, "Effects of upper limb positions and weight support roles on quasi-static seated postural stability in individuals with spinal cord injury," *Gait Posture*, vol. 36, no. 3, pp. 572–579, 2012.

[81] K. H. Sienko, V. V. Vichare, M. D. Balkwill, and C. Wall, "Assessment of vibrotactile feedback on postural stability during pseudorandom multidirectional platform motion," *IEEE Trans. Biomed. Eng.*, vol. 57, no. 4, pp. 944–952, 2010.

[82] S. Haggerty, L. T. Jiang, A. Galecki, and K. H. Sienko, "Effects of biofeedback on secondary-task response time and postural stability in older adults," *Gait Posture*, vol. 35, no. 4, pp. 523–528, 2012.

[83] C. Larivière, H. Mecheri, A. Shahvarpour, D. Gagnon, and A. Shirazi-Adl, "Criterion validity and between-day reliability of an inertial-sensor-based trunk postural stability test during unstable sitting," *J. Electromyogr. Kinesiol.*, vol. 23, no. 4, pp. 899–907, 2013.

[84] S. B. O'Sullivan and T. J. Schmitz, *Improving functional outcomes in physical rehabilitation*. FA Davis, 2016.

[85] N. Ibrahimi, S. Tufel, H. Singh, and M. Maurya, "Effect of sitting balance training under varied sensory input on balance and quality of life in stroke patients," *Indian J. Physiother. Occup. Ther.*, vol. 4, no. 3, pp. 40–45, 2010.

[86] C. M. Dean, E. F. Channon, and J. M. Hall, "Sitting training early after stroke improves sitting ability and quality and carries over to standing up but not to walking: A randomised

controlled trial," *Aust. J. Physiother.*, vol. 53, no. 2, pp. 97–102, 2007.

[87] C. M. Dean and R. B. Shepherd, "Task-related training improves performance of seated reaching tasks after stroke: A randomized controlled trial," *Stroke*, vol. 28, no. 4, pp. 722–728, 1997.

[88] M. De Sèze *et al.*, "Rehabilitation of postural disturbances of hemiplegic patients by using trunk control retraining during exploratory exercises," *Arch. Phys. Med. Rehabil.*, vol. 82, no. 6, pp. 793–800, 2001.

[89] M. H. Mudie, U. Winzeler-Mercay, S. Radwan, and L. Lee, "Training symmetry of weight distribution after stroke: A randomized controlled pilot study comparing task-related reach, Bobath and feedback training approaches," *Clin. Rehabil.*, vol. 16, no. 6, pp. 582–592, 2002.

[90] A. S. Pollock, B. R. Durward, P. J. Rowe, and J. P. Paul, "The effect of independent practice of motor tasks by stroke patients: A pilot randomized controlled trial," *Clin. Rehabil.*, vol. 16, no. 5, pp. 473–480, 2002.

[91] J. F. Bayouk, J. P. Boucher, and A. Leroux, "Balance training following stroke: Effects of task-oriented exercises with and without altered sensory input," *Int. J. Rehabil. Res.*, vol. 29, no. 1, pp. 51–59, 2006.

[92] A. L. Betker, A. Desai, C. Nett, N. Kapadia, and T. Szturm, "Game-based Exercises for Dynamic Short-Sitting Balance Rehabilitation of People With Chronic Spinal Cord and Traumatic Brain Injuries," *Phys. Ther.*, vol. 87, no. 10, pp. 1389–1398, 2007.

[93] P. W. Duncan *et al.*, "Body-Weight–Supported Treadmill Rehabilitation after Stroke," *N. Engl. J. Med.*, vol. 364, no. 21, pp. 2026–2036, 2011.

[94] R. W. Mechling, "Objective assessment of postural balance through use of the variable resistance balance board," *Phys. Ther.*, vol. 66, no. 5, pp. 685–688, 1986.

[95] R. Barclay-Goddard, T. Stevenson, W. Poluha, M. E. K. Moffatt, and S. P. Taback, "Force platform feedback for standing balance training after stroke," *Cochrane database Syst. Rev.*, no. 4, p. CD004129, 2004.

[96] S. Karthikbabu *et al.*, "Comparison of physio ball and plinth trunk exercises regimens on trunk control and functional balance in patients with acute stroke: a pilot randomized controlled trial," *Clin. Rehabil.*, vol. 25, no. 8, pp. 709–719, 2011.

[97] G. Verheyden *et al.*, "Additional exercises improve trunk performance after stroke: A pilot randomized controlled trial," *Neurorehabil. Neural Repair*, vol. 23, no. 3, pp. 281–286,

2009.

[98] S. W. Lee, D. C. Shin, and C. H. Song, "The Effects of Visual Feedback Training on Sitting Balance Ability and Visual Perception of Patients with Chronic Stroke," *J. Phys. Ther. Sci.*, vol. 25, no. 5, pp. 635–639, 2013.

[99] B. I. Han, H. S. Song, and J. S. Kim, "Vestibular rehabilitation therapy: Review of indications, mechanisms, and key exercises," *Journal of Clinical Neurology (Korea)*, vol. 7, no. 4. pp. 184–196, 2011.

[100] A. Martinez-Amat, F. Hita-Contreras, R. Lomas-Vega, I. Caballero Martinez, P. J. Alvarez, and E. Martínez-Lopez, "Effects of 12-week proprioception training program on postural stability, gait, and balance in older adults: A controlled clinical trial," *J. Strength Cond. Res.*, vol. 27, no. 8, pp. 2180–2188, 2013.

[101] X. Radvay, S. Duhoux, F. Koenig-Supiot, and F. Vital-Durand, "Balance training and visual rehabilitation of age-related macular degeneration patients.," *J. Vestib. Res.*, vol. 17, no. 2007, pp. 183–193, 2007.

[102] L. Wolfson, R. Whipple, J. Judge, P. Amerman, C. Derby, and M. King, "Training balance and strength in the elderly to improve function," *Journal of the American Geriatrics Society*, vol. 41, no. 3. pp. 341–343, 1993.

[103] J. O. Judge, C. Lindsey, M. Underwood, and D. Winsemius, "Balance improvements in older women: effects of exercise training.," *Phys. Ther.*, vol. 73, no. 4, pp. 254-262; discussion 263-265, 1993.

[104] S. K. Gatts and M. H. Woollacott, "Neural mechanisms underlying balance improvement with short term Tai Chi training.," *Aging Clin. Exp. Res.*, vol. 18, no. 1, pp. 7–19, 2006.

[105] A. Tözeren, *Human body dynamics : classical mechanics and human movement*. Springer, 2000.

[106] D. J. Pearsall, J. G. Reid, and R. Ross, "Inertial properties of the human trunk of males determined from magnetic resonance imaging," *Ann. Biomed. Eng.*, vol. 22, no. 6, pp. 692–706, 1994.

[107] G. Duval-Beaupère and G. Robain, "Visualization on full spine radiographs of the anatomical connections of the centres of the segmental body mass supported by each vertebra and measured in vivo," *Int. Orthop.*, vol. 11, no. 3, pp. 261–269, 1987.

[108] A. H. Vette, T. Yoshida, T. A. Thrasher, K. Masani, and M. R. Popovic, "A complete, non-

lumped, and verifiable set of upper body segment parameters for three-dimensional dynamic modeling," *Med. Eng. Phys.*, vol. 33, no. 1, pp. 70–79, 2011.

[109] Y. K. Liu and J. K. Wickstrom, "Estimation of the Inertial Property Distribution of the Human Torso from Segmented Cadaveric Data," in *Perspectives in Biomedical Engineering*, London: Palgrave Macmillan UK, 1973, pp. 203–213.

[110] R. K. Jensen, "Estimation of the biomechanical properties of three body types using a photogrammetric method," *J. Biomech.*, vol. 11, no. 8–9, pp. 349–358, 1978.

[111] R. K. Jensen, "Changes in segment inertia proportions between 4 and 20 years," *J. Biomech.*, vol. 22, no. 6–7, pp. 529–536, 1989.

[112] Y. K. Liu, J. M. Laborde, and W. C. Van Buskirk, "Inertial properties of a segmented cadaver trunk: their implications in acceleration injuries," *Aerosp. Med.*, vol. 42, no. 6, pp. 650–657, 1971.

[113] W. S. Erdmann, "Geometric and inertial data of the trunk in adult males," *J. Biomech.*, vol. 30, no. 7, pp. 679–688, 1997.

[114] V. Zatsiorsky and V. N. Seluyanov, *The mass and inertia characteristics of the main segment of human body*, vol. 4. 1982.

[115] J. Wicke and G. A. Dumas, "Estimating segment inertial parameters using fan-beam DXA," *J. Appl. Biomech.*, vol. 24, no. 2, pp. 180–184, 2008.

[116] J. Wicke, G. A. Dumas, and P. A. Costigan, "A comparison between a new model and current models for estimating trunk segment inertial parameters," *J. Biomech.*, vol. 42, no. 1, pp. 55–60, 2009.

[117] P. De Leva, "Adjustments to zatsiorsky-seluyanov's segment inertia parameters," *J. Biomech.*, vol. 29, no. 9, pp. 1223–1230, 1996.

[118] H. Zhou and H. Hu, "Human motion tracking for rehabilitation-A survey," *Biomedical Signal Processing and Control*, vol. 3, no. 1. pp. 1–18, 2008.

[119] A. Cappozzo, U. Della Croce, A. Leardini, and L. Chiari, "Human movement analysis using stereophotogrammetry. Part 1: Theoretical background," *Gait and Posture*, vol. 21, no. 2. pp. 186–196, 2005.

[120] A. Leardini, F. Biagi, C. Belvedere, and M. G. Benedetti, "Quantitative comparison of current models for trunk motion in human movement analysis," *Clin. Biomech.*, vol. 24, no. 7, pp. 542–550, 2009.

[121] W. P. Stevens, "Reconstruction of three-dimensional anatomical landmark coordinates using video-based stereophotogrammetry," *J. Anat.*, vol. 191, no. 2, pp. 277–284, 1997.

[122] G. Selvik, P. Alberius, and A. S. Aronson, "A roentgen stereophotogrammetric system. Construction, calibration and technical accuracy.," *Acta Radiol. Diagn. (Stockh).*, vol. 24, no. 4, pp. 343–52, 1983.

[123] L. Chiari, U. Della Croce, A. Leardini, and A. Cappozzo, "Human movement analysis using stereophotogrammetry. Part 2: Instrumental errors," *Gait and Posture*, vol. 21, no. 2. pp. 197–211, 2005.

[124] A. Schmitz, M. Ye, R. Shapiro, R. Yang, and B. Noehren, "Accuracy and repeatability of joint angles measured using a single camera markerless motion capture system," *J. Biomech.*, vol. 47, no. 2, pp. 587–591, 2014.

[125] A. Schmitz, M. Ye, G. Boggess, R. Shapiro, R. Yang, and B. Noehren, "The measurement of in vivo joint angles during a squat using a single camera markerless motion capture system as compared to a marker based system," *Gait Posture*, vol. 41, no. 2, pp. 694–698, 2015.

[126] S. Corazza, L. Mündermann, A. M. Chaudhari, T. Demattio, C. Cobelli, and T. P. Andriacchi, "A markerless motion capture system to study musculoskeletal biomechanics: Visual hull and simulated annealing approach," *Ann. Biomed. Eng.*, vol. 34, no. 6, pp. 1019–1029, 2006.

[127] A. Seminar, "An Introduction to Virtual Reality," *Virtual Real.*, pp. 1–19, 2002.

[128] Y. Tao, H. Hu, W. Park, and U. Kingdom, "Building A Visual Tracking System for Home-Based," *Proc. 9th Chinese Autom. Comput. Soc. Conf. UK, Luton, Engl.*, vol. 9, no. September, pp. 443–448, 2003.

[129] R. Finley and P. V Karpovich, "ELECTROGONIOMETRIC ANALYSIS OF NORMAL AND PATHOLOGICAL GAITS," 1961.

[130] N. Ahmad, R. A. R. Ghazilla, N. M. Khairi, and V. Kasi, "Reviews on Various Inertial Measurement Unit (IMU) Sensor Applications," *Int. J. Signal Process. Syst.*, pp. 256–262, 2013.

[131] P. B. Shull, W. Jirattigalachote, M. A. Hunt, M. R. Cutkosky, and S. L. Delp, "Quantified self and human movement: A review on the clinical impact of wearable sensing and feedback for gait analysis and intervention," *Gait and Posture*, vol. 40, no. 1. pp. 11–19,

2014.

[132] A. M. Sabatini, "Quaternion-based strap-down integration method for applications of inertial sensing to gait analysis," *Med. Biol. Eng. Comput.*, vol. 43, no. 1, pp. 94–101, 2005.

[133] J. K. Lee and E. J. Park, "3D spinal motion analysis during staircase walking using an ambulatory inertial and magnetic sensing system," *Med. Biol. Eng. Comput.*, vol. 49, no. 7, pp. 755–764, 2011.

[134] H. Dejnabadi, B. M. Jolles, E. Casanova, P. Fua, and K. Aminian, "Estimation and visualization of sagittal kinematics of lower limbs orientation using body-fixed sensors," *IEEE Trans. Biomed. Eng.*, vol. 53, no. 7, pp. 1385–1393, 2006.

[135] C. Malleson, A. Gilbert, M. Trumble, J. Collomosse, and A. Hilton, "Real-time Full-Body Motion Capture from Video and {IMUs}," *Int. Conf. 3D Vis.*, 2017.

[136] A. Maximilian, W. Kilian, S. Franz, and D. Sebastian, "Implementation and validation of human kinematics measured using IMUs for musculoskeletal simulations by the evaluation of joint reaction forces," in *IFMBE Proceedings*, 2017, vol. 62, pp. 205–211.

[137] T. A. Thrasher, V. W. Sin, K. Masani, A. H. Vette, B. C. Craven, and M. R. Popovic, "Response of the trunk to multidirectional perturbation during unsupported sitting," *J. Appl. Biomech.*, vol. 26, pp. 332–340, 2010.

[138] M. Ferrarin, M. Rizzone, L. Lopiano, M. Recalcati, and A. Pedotti, "Effects of subthalamic nucleus stimulation and L-dopa in trunk kinematics of patients with Parkinson's disease," *Gait Posture*, vol. 19, no. 2, pp. 164–171, 2004.

[139] M. Ferrarin *et al.*, "Quantitative analysis of gait in Parkinson's disease: a pilot study on the effects of bilateral sub-thalamic stimulation," *Gait Posture*, vol. 16, pp. 135–148, 2002.

[140] G. Wu *et al.*, "ISB recommendation on definitions of joint coordinate systems of various joints for the reporting of human joint motion - Part II: Shoulder, elbow, wrist and hand," *J. Biomech.*, vol. 38, no. 5, pp. 981–992, 2005.

[141] C. Frigo, R. Carabalona, M. Dalla Mura, and S. Negrini, "The upper body segmental movements during walking by young females," *Clin. Biomech.*, vol. 18, no. 5, pp. 419–425, 2003.

[142] F. C. Silvia Fantozzi, Maria Grazia Benedetti, Alberto Leardini, Scott Arthur Banks, Angelo Cappello, Doretta Assirelli, "Fluroscopic and gait analysis of the functional performance in stair ascent of total knee replacement designs," *Gait Posture*, vol. 17, pp. 225–234, 2003.

[143] J. J. Craig, "Introduction to Robotics: Mechanics and Control 3rd," *Prentice Hall*, vol. 1, no. 3. p. 408, 2004.

[144] G. K. Cole, B. M. Nigg, J. L. Ronsky, and M. R. Yeadon, "Application of the Joint Coordinate System to Three-Dimensional Joint Attitude and Movement Representation: A Standardization Proposal," *J. Biomech. Eng.*, vol. 115, no. 4A, p. 344, 1993.

[145] S. Wardoyo, P. T. Hutajulu, and O. Togibasa, "A Development of Force Plate for Biomechanics Analysis of Standing and Walking," in *Journal of Physics: Conference Series*, 2016, vol. 739, no. 1.

[146] M. Lord, "Foot Pressure Measurement: a Review of Methodology," *J. Biomed. Engng.*, vol. 3, pp. 91–99, 1981.

[147] S. Crea, M. Donati, S. M. M. De Rossi, C. Maria Oddo, and N. Vitiello, "A wireless flexible sensorized insole for gait analysis," *Sensors (Switzerland)*, vol. 14, no. 1, pp. 1073–1093, 2014.

[148] A. H. Vette, K. Masani, N. Wu, and M. R. Popovic, "Multidirectional quantification of trunk stiffness and damping during unloaded natural sitting," *Med. Eng. Phys.*, vol. 36, no. 1, pp. 102–109, 2014.

[149] P. van Drunen, F. C. T. van der Helm, J. H. van Dieën, and R. Happee, "Trunk stabilization during sagittal pelvic tilt: from trunk-on-pelvis to trunk-in-space due to vestibular and visual feedback," *J. Neurophysiol.*, vol. 115, no. 3, pp. 1381–1388, 2016.

[150] J. H. Pasma *et al.*, "Reliability of system identification techniques to assess standing balance in healthy elderly," *PLoS One*, vol. 11, no. 3, 2016.

[151] A. Kot and A. Nawrocka, "Modeling of human balance as an inverted pendulum," *Proc. 2014 15th Int. Carpathian Control Conf. ICCC 2014*, pp. 254–257, 2014.

[152] A. H. Vette, T. Yoshida, T. A. Thrasher, K. Masani, and M. R. Popovic, "A comprehensive three-dimensional dynamic model of the human head and trunk for estimating lumbar and cervical joint torques and forces from upper body kinematics," *Med. Eng. Phys.*, vol. 34, no. 5, pp. 640–649, 2012.

[153] C. Fortin, S. Nadeau, and H. Labelle, "Inter-trial and test-retest reliability of kinematic and kinetic gait parameters among subjects with adolescent idiopathic scoliosis," *Eur. Spine J.*, vol. 17, no. 2, pp. 204–216, 2008.

[154] H. R. Alireza Noamani, Albert Vette, Richard Preuss, Milos R Popovic, "Optimal

Estimation of Anthropometric Parameters for Quantifying Multi-Segment Trunk Kinetics," *J. Biomech. Eng.*, no. 10.1115/1.4040247, 2017.

[155] A. Noamani, A. H. Vette, R. Preuss, M. R. Popovic, and H. Rouhani, "Quantification of multi-segment trunk kinetics during multi-directional trunk bending," *Gait Posture*, vol. 64, pp. 205–212, Jul. 2018.

[156] J. Jeka, K. S. Oie, and T. Kiemel, "Multisensory information for human postural control: Integrating touch and vision," *Exp. Brain Res.*, vol. 134, no. 1, pp. 107–125, 2000.

[157] K. S. Oie, T. Kiemel, and J. J. Jeka, "Multisensory fusion: Simultaneous re-weighting of vision and touch for the control of human posture," *Cogn. Brain Res.*, vol. 14, no. 1, pp. 164–176, 2002.

[158] "How does our sense of balance work?," Sep. 2017.

[159] Hubbel, "Eye, Brain and Vision," *J. Chem. Inf. Model.*, vol. 53, no. 1, pp. 1689–1699, 2013.

[160] A. Ksendzovsky, I. J. Pomeraniec, K. A. Zaghloul, J. J. Provencio, and I. Provencio, "Clinical implications of the melanopsin-based non-image-forming visual system," *Neurology*, vol. 88, no. 13. pp. 1282–1290, 2017.

[161] S. P. Silfies, J. Cholewicki, and A. Radebold, "The effects of visual input on postural control of the lumbar spine in unstable sitting," *Hum. Mov. Sci.*, vol. 22, no. 3, pp. 237–252, Aug. 2003.

[162] E. E. Hansson, A. Beckman, and A. Håkansson, "Effect of vision, proprioception, and the position of the vestibular organ on postural sway," *Acta Otolaryngol.*, vol. 130, no. 12, pp. 1358–1363, 2010.

[163] M. G. Wade and G. Jones, "The role of vision and spatial orientation in the maintenance of posture," *Physical Therapy*, vol. 77, no. 6. pp. 619–628, 1997.

[164] N. Teasdale, G. E. Stelmach, and A. Breunig, "Postural Sway Characteristics of the Elderly Under Normal and Altered Visual and Support Surface Conditions," *J. Gerontol. Biol. Sci.*, vol. 46, no. 6, pp. 238–244, 1991.

[165] S. Schwartz, O. Segal, Y. Barkana, R. Schwesig, I. Avni, and Y. Morad, "The effect of cataract surgery on postural control," *Investig. Ophthalmol. Vis. Sci.*, vol. 46, no. 3, pp. 920–924, 2005.

[166] L. R. Wade, W. H. Weimar, and J. Davis, "Effect of personal protective eyewear on postural stability.," *Ergonomics*, vol. 47, no. 15, pp. 1614–23, 2004.

[167] F. B. Shumway-Cook, A. and Horak, "Assessing the influence of sensory integration on balance. Suggestions from the field.," *Phys. Ther.*, no. 66, pp. 1548–1549, 1986.

[168] R. J. Cherng, J. J. Chen, and F. C. Su, "Vestibular System in Performance of Standing Balance of Children and Young Adults under Altered Sensory Conditions," *Percept. Mot. Skills*, vol. 92, no. 3_suppl, pp. 1167–1179, 2001.

[169] R. C. Fitzpatrick, "Probing the human vestibular system with galvanic stimulation," *J. Appl. Physiol.*, vol. 96, no. 6, pp. 2301–2316, 2004.

[170] Y. Agrawal, J. P. Carey, C. C. Della Santina, M. C. Schubert, and L. B. Minor, "Disorders of balance and vestibular function in US adults: data from the National Health and Nutrition Examination Survey, 2001-2004," *Arch Intern Med*, vol. 169, no. 10, pp. 938–944, 2009.

[171] W. F. Boron and E. L. Boulpaep, *Medical physiology: a cellular and molecular approach*. 2009.

[172] M. Dieterich and T. Brandt, "Vestibulo-ocular reflex," *Curr Opin Neurol*, vol. 8, no. 1, pp. 83–88, 1995.

[173] J. F. Iles, R. Baderin, R. Tanner, and A. Simon, "Human standing and walking: Comparison of the effects of stimulation of the vestibular system," *Exp. Brain Res.*, vol. 178, no. 2, pp. 151–166, 2007.

[174] J. Dickinson, "Proprioceptive Control of Human Movement. The Human Movement Series." Lepus Books, Henry Kimpton Ltd., London, England (#3.50 English Pounds), 1974.

[175] J. C. Moore, "The Golgi tendon organ: a review and update.," *The American journal of occupational therapy. : official publication of the American Occupational Therapy Association*, vol. 38, no. 4. pp. 227–236, 1984.

[176] J. H. J. Allum, "Organization of stabilizing reflex responses in tibialis anterior muscles following ankle flexion perturbations of standing man," *Brain Res.*, vol. 264, no. 2, pp. 297–301, 1983.

[177] J. J. Jeka, G. Schöner, T. Dijkstra, P. Ribeiro, and J. R. Lackner, "Coupling of fingertip somatosensory information to head and body sway," *Exp. Brain Res.*, vol. 113, no. 3, pp. 475–483, 1997.

[178] R. Johansson, M. Magnusson, and M. Akesson, "Identification of human postural dynamics," *IEEE Trans. Biomed. Eng.*, vol. 35, no. 10, pp. 858–869, 1988.

[179] A. Kavounoudias, J. C. Gilhodes, R. Roll, and J. P. Roll, "From balance regulation to body orientation: Two goals for muscle proprioceptive information processing?," *Exp. Brain Res.*, vol. 124, no. 1, pp. 80–88, 1999.

[180] P. van Drunen, Y. Koumans, F. C. T. van der Helm, J. H. van Dieën, and R. Happee, "Modulation of intrinsic and reflexive contributions to low-back stabilization due to vision, task instruction, and perturbation bandwidth," *Exp. Brain Res.*, vol. 233, no. 3, pp. 735–749, 2015.

[181] L. M. Nashner and P. Wolfson, "Influence of head position and proprioceptive cues on short latency postural reflexes evoked by galvanic stimulation of the human labyrinth," *Brain Res.*, vol. 67, no. 2, pp. 255–268, 1974.

[182] H. C. Diener, J. Dichgans, F. Bootz, and M. Bacher, "Early stabilization of human posture after a sudden disturbance: influence of rate and amplitude of displacement," *Exp. Brain Res.*, vol. 56, no. 1, pp. 126–134, 1984.

[183] L. M. Nashner, "Fixed patterns of rapid postural responses among leg muscles during stance," *Exp. Brain Res.*, vol. 30, no. 1, pp. 13–24, 1977.

[184] E. R. Kandel, J. H. Schwartz, T. M. Jessell, S. A. Siegelbaum, and A. J. Hudspeth, *Principles of Neural Science, Fifth Edition*, vol. 3. 2014.

[185] A. Conta and D. Stelzner, "The Spinal Cord: A Christopher and Dana Reeve Foundation Text and Atlas," in *The Spinal Cord: A Christopher and Dana Reeve Foundation Text and Atlas*, 2008, p. 387.

[186] M. A. Watson and F. O. Black, "The Human Balance System: A Complex Coordination of Central and Peripheral System," *Vestib. Disord. Assoc.*, no. S-7, pp. 1–4, 2008.

[187] J. Jeka, T. Kiemel, R. Creath, F. Horak, and R. Peterka, "Controlling human upright posture: velocity information is more accurate than position or acceleration.," *J. Neurophysiol.*, vol. 92, no. 4, pp. 2368–79, 2004.

[188] S. Machado *et al.*, "Sensorimotor integration: basic concepts, abnormalities related to movement disorders and sensorimotor training-induced cortical reorganization.," *Rev. Neurol.*, vol. 51, no. 7, pp. 427–436, 2010.

[189] A. D. Goodworth and R. J. Peterka, "Identifying mechanisms of stance control: A single stimulus multiple output model-fit approach," *J. Neurosci. Methods*, vol. 296, pp. 44–56, 2018.

[190] H. van der Kooij and E. de Vlugt, "Postural Responses Evoked by Platform Pertubations Are Dominated by Continuous Feedback," *J. Neurophysiol.*, vol. 98, no. 2, pp. 730–743, 2007.

[191] M. Hasan, C. Saha, M. Mostafizur Rahman, M. Rabiual Islam Sarker, and S. K. Aditya, "Balancing of an Inverted Pendulum Using PD Controller," *J. Sci*, vol. 60, no. 1, pp. 115–120, 2012.

[192] A. C. Schouten, E. De Vlugt, J. J. Van Hilten, and F. C. T. Van Der Helm, "Quantifying proprioceptive reflexes during position control of the human arm," *IEEE Trans. Biomed. Eng.*, vol. 55, no. 1, pp. 311–321, 2008.

[193] T. D. J. Welch and L. H. Ting, "A feedback model reproduces muscle activity during human postural responses to support-surface translations," *J. Neurophysiol.*, vol. 99, no. December 2007, pp. 1032–1038, 2008.

[194] S. D. Hanwate and Y. V. Hote, "Design of PID controller for inverted pendulum using stability boundary locus," in *11th IEEE India Conference: Emerging Trends and Innovation in Technology, INDICON 2014*, 2015.

[195] a N. K. Nasir, R. M. T. R. Ismail, and M. a Ahmad, "Performance Comparison between Sliding Mode Control (SMC) and PD-PID Controllers for a Nonlinear Inverted Pendulum System," *World Acad. Sci. Eng. Technol.*, vol. 4, no. 10, pp. 400–405, 2010.

[196] C. W. C. W. Anderson, "Learning to Control an Inverted Pendulum Using Neural Networks," *IEEE Control Syst. Mag.*, vol. 9, no. 3, pp. 31–37, 1989.

[197] M. W. Spong, P. Corke, and R. Lozano, "Nonlinear control of the Reaction Wheel Pendulum," *Automatica*, vol. 37, no. 11, pp. 1845–1851, 2001.

[198] M. A. Lee and H. Takagi, "Integrating design stage of fuzzy systems using genetic algorithms," in *[Proceedings 1993] Second IEEE International Conference on Fuzzy Systems*, 1993, pp. 612–617.

[199] B. Feinstein, B. Lindegård, E. Nyman, and G. Wohlfart, "MORPHOLOGIC STUDIES OF MOTOR UNITS IN NORMAL HUMAN MUSCLES," *Cells Tissues Organs*, vol. 23, no. 2, pp. 127–142, 1955.

[200] C. Watson and G. Kayalioglu, "The Organization of the Spinal Cord," in *The Spinal Cord*, 2009, pp. 1–7.

[201] Z. Erim, C. J. De Luca, K. Mineo, and T. Aoki, "Rank-ordered regulation of motor units,"

Muscle and Nerve, vol. 19, no. 5, pp. 563–573, 1996.

[202] S. M. McGill, "Electromyographic activity of the abdominal and low back musculature during the generation of isometric and dynamic axial trunk torque: Implications for lumbar mechanics," *J. Orthop. Res.*, vol. 9, no. 1, pp. 91–103, 1991.

[203] J. K.-F. K. F. Ng, V. Kippers, M. Parnianpour, and C. A. Richardson, "EMG activity normalization for trunk muscles in subjects with and without back pain," *Med. Sci. Sports Exerc.*, vol. 34, no. 7, pp. 1082–1086, 2002.

[204] P. B. O'Sullivan, K. M. Grahamslaw, M. Kendell, S. C. Lapenskie, N. E. Möller, and K. V. Richards, "The effect of different standing and sitting postures on trunk muscle activity in a pain-free population.," *Spine (Phila. Pa. 1976).*, vol. 27, no. 11, pp. 1238–1244, 2002.

[205] G. J. Lehman and S. M. McGill, "Spinal manipulation causes variable spine kinematic and trunk muscle electromyographic responses," *Clin. Biomech.*, vol. 16, no. 4, pp. 293–299, 2001.

[206] F. J. Vera-garcia, S. H. M. M. Brown, J. R. Gray, and S. M. McGill, "Effects of different levels of torso coactivation on trunk muscular and kinematic responses to posteriorly applied sudden loads," *Clin. Biomech.*, vol. 21, no. 5, pp. 443–455, 2006.

[207] J. Cholewicki and S. M. Mcgill Pm, "Mechanical stability of the in viva lumbar spine: implications for injury and chronic low back pain," *Clin. Biomech.*, vol. 11, no. 1, pp. 1–15, 1996.

[208] K. Florence P, P. Patricia G, M. Rodgers, and R. William, *Muscles: Testing and Function, with Posture and Pain*, vol. 53, no. 9. 2013.

[209] M. Zedka, S. Kumar, and Y. Narayan, "Electromyographic response of the trunk muscles to postural perturbation in sitting subjects," *J. Electromyogr. Kinesiol.*, vol. 8, no. 1, pp. 3–10, 1998.

[210] K. Masani *et al.*, "Postural reactions of the trunk muscles to multi-directional perturbations in sitting," *Clin. Biomech.*, vol. 24, no. 2, pp. 176–182, 2009.

[211] R. Preuss and J. Fung, "Musculature and biomechanics of the trunk in the maintenance of upright posture," *J. Electromyogr. Kinesiol.*, vol. 18, no. 5, pp. 815–828, 2008.

[212] N. Farahpour, S. Ghasemi, P. Allard, and M. S. Saba, "Electromyographic responses of erector spinae and lower limb's muscles to dynamic postural perturbations in patients with adolescent idiopathic scoliosis," *J. Electromyogr. Kinesiol.*, vol. 24, no. 5, pp. 645–651,

2014.

[213] M.-C. Kim, S. Han, and S. Kim, "Changes in the Range of Motion of the Hip Joint and the Muscle Activity of the Rectus Femoris and Biceps Femoris of Stroke Patients during Obstacles Crossing on the Ground and Underwater.," *J. Phys. Ther. Sci.*, vol. 26, no. 8, pp. 1143–1146, 2014.

[214] C. Song, H. Huang, S. Chen, J. Lin, and A. H. Chang, "Effects of femoral rotational taping on pain, lower extremity kinematics, and muscle activation in female patients with patellofemoral pain," *J. Sci. Med. Sport*, pp. 12–14, 2014.

[215] H. R. Kuhnen *et al.*, "Stroke-related effects on maximal dynamic hip flexor fatigability and functional implications," *Muscle and Nerve*, vol. 51, no. 3, pp. 446–448, 2015.

[216] T. Jiroumaru, T. Kurihara, and T. Isaka, "Measurement of muscle length-related electromyography activity of the hip flexor muscles to determine individual muscle contributions to the hip flexion torque," *Springerplus*, vol. 3, no. 1, p. 624, 2014.

[217] M. P. Kadaba, M. E. Wootten, J. Gainey, and G. V. B. Cochran, "Repeatability of phasic muscle activity: Performance of surface and intramuscular wire electrodes in gait analysis," *J. Orthop. Res.*, vol. 3, no. 3, pp. 350–359, 1985.

[218] J. Kilby, K. Prasad, and G. Mawston, "Multi-channel surface electromyography electrodes: A review," *IEEE Sensors Journal*, vol. 16, no. 14. pp. 5510–5519, 2016.

[219] F. BUCHTHAL, C. GULD, and P. ROSENFALCK, "Propagation Velocity in Electrically Activated Muscle Fibres in Man," *Acta Physiol. Scand.*, vol. 34, no. 1, pp. 75–89, 1955.

[220] A. J. Fuglevand, D. A. Winter, A. E. Patla, and D. Stashuk, "Detection of motor unit action potentials with surface electrodes: influence of electrode size and spacing," *Biol. Cybern.*, vol. 67, no. 2, pp. 143–153, 1992.

[221] B. S. Day, "Important Factors in Surface EMG Measurement," *Measurement*, pp. 1–17, 2002.

[222] G. Kamen and G. E. Caldwell, "Physiology and interpretation of the electromyogram," *Journal of Clinical Neurophysiology*, vol. 13, no. 5. pp. 366–384, 1996.

[223] E. A. Clancy, E. L. Morin, and R. Merletti, "Sampling, noise-reduction and amplitude estimation issues in surface electromyography," in *Journal of Electromyography and Kinesiology*, 2002, vol. 12, no. 1, pp. 1–16.

[224] C. Larivière, D. Gagnon, and P. Loisel, "The comparison of trunk muscles EMG activation

between subjects with and without chronic low back pain during flexion-extension and lateral bending tasks," *Journal of Electromyography and Kinesiology*, vol. 10, no. 2. pp. 79–91, 2000.

[225] S. M. McGill, N. S. Kavcic, and E. Harvey, "Sitting on a chair or an exercise ball: Various perspectives to guide decision making," *Clin. Biomech.*, vol. 21, no. 4, pp. 353–360, 2006.

[226] J. R. Potvin, R. W. Norman, and S. M. McGill, "Mechanically corrected EMG for the continuous estimation of erector spinae muscle loading during repetitive lifting," *Eur. J. Appl. Physiol. Occup. Physiol.*, vol. 74, no. 1–2, pp. 119–132, 1996.

[227] R. Merletti, M. Aventaggiato, A. Botter, A. Holobar, H. Marateb, and T. M. M. Vieira, "Advances in surface EMG: recent progress in detection and processing techniques.," *Crit. Rev. Biomed. Eng.*, vol. 38, no. 4, pp. 305–45, 2010.

[228] W. Dankaerts *et al.*, "Reliability of EMG measurements for trunk muscles during maximal and sub-maximal voluntary isometric contractions in healthy controls and CLBP patients," *J. Electromyogr. Kinesiol.*, vol. 14, no. 3, pp. 333–342, 2004.

[229] A. Burden and R. Bartlett, "Normalisation of EMG amplitude: An evaluation and comparison of old and new methods," *Med. Eng. Phys.*, vol. 21, no. 4, pp. 247–257, 1999.

[230] D. Staudenmann, K. Roeleveld, D. F. Stegeman, and J. H. van Dieen, "Methodological aspects of SEMG recordings for force estimation - A tutorial and review," *Journal of Electromyography and Kinesiology*, vol. 20, no. 3. pp. 375–387, 2010.

[231] G. L. Soderberg and L. M. Knutson, "A guide for use and interpretation of kinesiologic electromyographic data.," *Phys. Ther.*, vol. 80, no. 5, pp. 485–98, 2000.

[232] J. Cholewicki *et al.*, "A comparison of a maximum exertion method and a model-based, sub-maximum exertion method for normalizing trunk EMG," *J. Electromyogr. Kinesiol.*, vol. 21, no. 5, pp. 767–773, 2011.

[233] J. P. A. Dewald, P. S. Pope, J. D. Given, T. S. Buchanan, and W. Z. Rymer, "Abnormal muscle coactivation patterns during isometric torque generation at the elbow and shoulder in hemiparetic subjects," *Brain*, vol. 118, no. 2, pp. 495–510, 1995.

[234] J. K. F. Ng, M. Parnianpour, C. A. Richardson, and V. Kippers, "Functional roles of abdominal and back muscles during isometric axial rotation of the trunk," *J. Orthop. Res.*, vol. 19, no. 3, pp. 0–8, 2001.

[235] J. S. Thomas, S. A. Lavender, D. M. Corcos, and G. B. J. Andersson, "Trunk kinematics

and trunk muscle activity during a rapidly applied load," *J. Electromyogr. Kinesiol.*, vol. 8, no. 4, pp. 215–225, 1998.

[236] J. K. F. Ng, C. A. Richardson, M. Parnianpour, and V. Kippers, "EMG activity of trunk muscles and torque output during isometric axial rotation exertion: A comparison between back pain patients and matched controls," *J. Orthop. Res.*, vol. 20, no. 1, pp. 112–121, 2002.

[237] A. Burden, "How should we normalize electromyograms obtained from healthy participants? What we have learned from over 25years of research," *Journal of Electromyography and Kinesiology*, vol. 20, no. 6. pp. 1023–1035, 2010.

[238] J. S. Dufour, W. S. Marras, and G. G. Knapik, "An EMG-assisted model calibration technique that does not require MVCs," *J. Electromyogr. Kinesiol.*, vol. 23, no. 3, pp. 608–613, 2013.

[239] G. T. Allison, P. Godfrey, and G. Robinson, "EMG signal amplitude assessment during abdominal bracing and hollowing," *J. Electromyogr. Kinesiol.*, vol. 8, no. 1, pp. 51–57, 1998.

[240] H. Rouhani, M. R. Popovic, M. Same, Y. Q. Li, and K. Masani, "Identification of ankle plantar-flexors dynamics in response to electrical stimulation," *Med. Eng. Phys.*, vol. 38, no. 11, pp. 1166–1171, 2016.

[241] T. S. Buchanan, D. G. Lloyd, K. Manal, and T. F. Besier, "Neuromusculoskeletal modeling: Estimation of muscle forces and joint moments and movements from measurements of neural command," *J. Appl. Biomech.*, vol. 20, no. 4, pp. 367–395, 2004.

[242] H. Rouhani, M. Same, K. Masani, Y. Q. Li, and M. R. Popovic, "PID controller design for FES applied to ankle muscles in neuroprosthesis for standing balance," *Front. Neurosci.*, vol. 11, no. JUN, pp. 1–14, 2017.

[243] C. L. Lynch, M. R. Popovic, and D. Rushton, "Functional Electrical Stimulation," *IEEE Control Syst. Mag.*, vol. 28, no. 2, pp. 40–50, 2008.

[244] S. N. Kukke and R. J. Triolo, "The effects of trunk stimulation on bimanual seated workspace," *IEEE Trans. Neural Syst. Rehabil. Eng.*, vol. 12, no. 2, pp. 177–185, 2004.

[245] A. Dutta, R. Kobetic, and R. Triolo, "Development of an implanted intramuscular EMG-triggered FES system for ambulation after incomplete spinal cord injury," in *Proceedings of the 31st Annual International Conference of the IEEE Engineering in Medicine and Biology Society: Engineering the Future of Biomedicine, EMBC 2009*, 2009.

[246] F. E. Zajac, "Muscle and tendon: properties, models, scaling, and application to biomechanics and motor control.," *Crit. Rev. Biomed. Eng.*, vol. 17, no. 4, pp. 359–411, 1989.

[247] H. S. Milner-Brown, R. B. Stein, and R. Yemm, "Changes in firing rate of human motor units during linearly changing voluntary contractions," *J. Physiol.*, vol. 230, no. 2, pp. 371–390, 1973.

[248] C. W. Heckathorne and D. S. Childress, "Relationships of the surface electromyogram to the force, length, velocity, and contraction rate of the cineplastic human biceps," *American Journal of Physical Medicine*, vol. 60, no. 1. pp. 1–19, 1981.

[249] J. J. Woods and B. Bigland-Ritchie, "Linear and non-linear surface EMG/force relationships in human muscles. An anatomical/functional argument for the existence of both.," *Am. J. Phys. Med.*, vol. 62, no. 6, pp. 287–99, 1983.

[250] E. N. Zuniga and E. G. Simons, "Nonlinear relationship between averaged electromyogram potential and muscle tension in normal subjects.," *Arch. Phys. Med. Rehabil.*, vol. 50, no. 11, pp. 613–20, Nov. 1969.

[251] K. Manal and T. S. Buchanan, "A one-parameter neural activation to muscle activation model: Estimating isometric joint moments from electromyograms," *J. Biomech.*, vol. 36, no. 8, pp. 1197–1202, 2003.

[252] D. G. Lloyd and T. F. Besier, "An EMG-driven musculoskeletal model to estimate muscle forces and knee joint moments in vivo," *J. Biomech.*, vol. 36, no. 6, pp. 765–776, 2003.

[253] K. Manal, R. V. Gonzalez, D. G. Lloyd, and T. S. Buchanan, "A real-time EMG-driven virtual arm," *Comput. Biol. Med.*, vol. 32, no. 1, pp. 25–36, 2002.

[254] D. F. B. Haeufle, M. Günther, A. Bayer, and S. Schmitt, "Hill-type muscle model with serial damping and eccentric force-velocity relation," *J. Biomech.*, vol. 47, no. 6, pp. 1531–1536, 2014.

[255] P. Pigeon, L. Yahia, and A. G. Feldman, "Moment arms and lengths of human upper limb muscles as functions of joint angles," *J. Biomech.*, vol. 29, no. 10, pp. 1365–1370, 1996.

[256] J. J. Visser, J. E. Hoogkamer, M. F. Bobbert, and P. A. Huijing, "Length and moment arm of human leg muscles as a function of knee and hip-joint angles," *Eur. J. Appl. Physiol. Occup. Physiol.*, vol. 61, no. 5–6, pp. 453–460, 1990.

[257] S. L. Delp and J. P. Loan, "A graphics-based software system to develop and analyze models

of musculoskeletal structures," *Comput. Biol. Med.*, vol. 25, no. 1, pp. 21–34, 1995.

[258] K. N. An, K. Takahashi, T. P. Harrigan, and E. Y. Chao, "Determination of Muscle Orientations and Moment Arms," *J. Biomech. Eng.*, vol. 106, no. 3, p. 280, 1984.

[259] H. Der Van Kooij, S. Donker, M. De Vrijer, and F. Van Der Helm, "Identification of human balance control in standing," in *Conference Proceedings - IEEE International Conference on Systems, Man and Cybernetics*, 2004, vol. 3, pp. 2535–2541.

[260] R. Fitzpatrick, D. Burke, and S. C. Gandevia, "Loop gain of reflexes controlling human standing measured with the use of postural and vestibular disturbances.," *J. Neurophysiol.*, vol. 76, no. 6, pp. 3994–4008, 1996.

[261] J. H. Pasma, D. Engelhart, A. C. Schouten, H. van der Kooij, A. B. Maier, and C. G. M. Meskers, "Impaired standing balance: The clinical need for closing the loop," *Neuroscience*, vol. 267, pp. 157–165, 2014.

[262] J. P. Callaghan, J. L. Gunning, and S. M. McGill, "The Relationship Between Lumbar Spine Load and Muscle Activity During Extensor Exercises," *Phys. Ther.*, vol. 78, no. 1, pp. 8–18, 1998.

[263] M. W. Olson, "Trunk extensor fatigue influences trunk muscle activities during walking gait," *J. Electromyogr. Kinesiol.*, vol. 20, no. 1, pp. 17–24, 2010.

[264] R. L. Cromwell, T. K. Aadland-Monahan, A. T. Nelson, S. M. Stern-Sylvestre, and B. Seder, "Sagittal plane analysis of head, neck, and trunk kinematics and electromyographic activity during locomotion.," *J. Orthop. Sports Phys. Ther.*, vol. 31, no. 5, pp. 255–62, 2001.

[265] T. Eason, C. R. Gavel, K. A. Hawley, S. S. Galen, and M. H. Malek, "Reliability of the log-transformed EMG amplitude-power output relationship for incremental knee-extensor ergometry," *Muscle and Nerve*, vol. 52, no. 3, pp. 428–434, 2015.

[266] C. Giroux, G. Guilhem, A. Couturier, D. Chollet, and G. Rabita, "Is muscle coordination affected by loading condition in ballistic movements?," *J. Electromyogr. Kinesiol.*, vol. 25, no. 1, pp. 69–76, 2015.

[267] R. van den Tillaar, V. Andersen, and A. H. Saeterbakken, "Comparison of Muscle Activation and Performance During 6 Rm, Two- Legged Free-Weight Squats," *Kinesiol. Slov.*, vol. 20, no. 2, pp. 5–16, 2014.

[268] A. Saito, K. Watanabe, and H. Akima, "Coordination among thigh muscles including the vastus intermedius and adductor magnus at different cycling intensities," *Hum. Mov. Sci.*,

vol. 40, pp. 14–23, 2015.

[269] A. Rainoldi, G. Melchiorri, and I. Caruso, "A method for positioning electrodes during surface EMG recordings in lower limb muscles," *J. Neurosci. Methods*, 2004.

[270] S. H. M. Brown, M. L. Haumann, and J. R. Potvin, "The responses of leg and trunk muscles to sudden unloading of the hands: Implications for balance and spine stability," *Clin. Biomech.*, vol. 18, no. 9, pp. 812–820, 2003.

[271] S. J. Atkins, I. Bentley, D. Brooks, M. P. Burrows, H. T. Hurst, and J. K. Sinclair, "Electromyographic response of global abdominal stabilizers in response to stable-and unstable-base isometric exercise," *J. Strength Cond. Res.*, vol. 29, no. 6, pp. 1609–1615, 2015.

[272] D. Czaprowski *et al.*, "Abdominal muscle EMG-activity during bridge exercises on stable and unstable surfaces," *Phys. Ther. Sport*, vol. 15, no. 3, pp. 162–168, 2014.

[273] S. McGill, J. Andersen, and J. Cannon, "Muscle activity and spine load during anterior chain whole body linkage exercises: the body saw, hanging leg raise and walkout from a push-up," *J. Sports Sci.*, vol. 33, no. 4, pp. 419–426, 2015.

[274] L. R. Frost, M. E. Gerling, J. L. Markic, and S. H. M. Brown, "Exploring the effect of repeated-day familiarization on the ability to generate reliable maximum voluntary muscle activation," *J. Electromyogr. Kinesiol.*, vol. 22, no. 6, pp. 886–892, 2012.

[275] F. J. Vera-garcia, J. M. Moreside, and S. M. McGill, "MVC techniques to normalize trunk muscle EMG in healthy women," *J. Electromyogr. Kinesiol.*, vol. 20, no. 1, pp. 10–16, 2010.

[276] E. Bressel, D. G. Dolny, and M. Gibbons, "Trunk muscle activity during exercises performed on land and in water," *Med. Sci. Sports Exerc.*, vol. 43, no. 10, pp. 1927–1932, 2011.

[277] G. Paz, M. Maia, F. Santiago, V. Lima, and H. Miranda, "Muscle activity of the erector spinae during Pilates isometric exercises on and off Swiss Ball," *J. Sports Med. Phys. Fitness*, vol. 54, no. 5, pp. 575–580, 2014.

[278] N. Cordeiro, N. Cortes, O. Fernandes, A. Diniz, and P. Pezarat-Correia, "Dynamic knee stability and ballistic knee movement after ACL reconstruction: an application on instep soccer kick," *Knee Surgery, Sport. Traumatol. Arthrosc.*, vol. 23, no. 4, pp. 1100–1106, Apr. 2015.

[279] S. P. Gombatto, D. R. Collins, S. A. Sahrmann, J. R. Engsberg, and L. R. Van Dillen, "Patterns of lumbar region movement during trunk lateral bending in 2 subgroups of people with low back pain.," *Phys. Ther.*, vol. 87, no. 4, pp. 441–454, 2007.

[280] H. Goldstein, C. Poole, and J. Safko, "Classical Mechanics," *Book*. pp. 1–646, 2007.

[281] P. D. Welch, "The Use of Fast Fourier Transform for the Estimation of Power Spectra: A Method Based on Time Averaging Over Short, Modified Periodograms," *IEEE Trans. Audio Electroacoust.*, vol. 15, no. 2, pp. 70–73, 1967.

[282] P. Hall, "Theoretical comparison of Bootstrap Confidence Intervals," *Ann. Stat.*, vol. 16, no. 3, pp. 927–953, 1988.

[283] G. Towler and R. Sinnott, "Instrumentation and Process Control," in *Chemical Engineering Design*, 2013, pp. 251–277.

[284] J. C. Lagarias, J. A. Reeds, M. H. Wright, and P. E. Wright, "Convergence Properties of the Nelder--Mead Simplex Method in Low Dimensions," *SIAM J. Optim.*, 1998.

[285] M. A. Rousseau, D. S. Bradford, T. M. Hadi, K. L. Pedersen, and J. C. Lotz, "The instant axis of rotation influences facet forces at L5/S1 during flexion/extension and lateral bending," *Eur. Spine J.*, 2006.

[286] M. Vanoncini, W. Holderbaum, and B. J. Andrews, "Development of closed loop FES controllers for trunk stabilization in paraplegia," *13th Int. FES Soc. Conf.*, vol. 11, no. 4, pp. 365–367, 2008.

[287] J. Cholewicki and S. M. McGill, "Mechanical stability of the in vivo lumbar spine: Implications for injury and chronic low back pain," *Clin. Biomech.*, vol. 11, no. 1, pp. 1–15, 1996.

Appendices

Appendix I – Health screening form

SUBJECT DATA SHEET

Assessment of Dynamic Balance and Fall Risk in Sitting

This questionnaire asks some questions about your health status. This information is used to guide us with your entry into the study. Specific medical conditions that will not allow you to participate in this study include any neurological or musculoskeletal conditions, or any injury/pain that makes the participation uncomfortable.

Participant ID: _____   Collector Initials: _____

Date: _____

DEMOGRAPHIC INFORMATION (self-report / direct measurement):

Age: _____ years   Weight: _____ kg

Sex: _____   Handedness: _____

Height: _____ cm

For Females: Pregnant _____

SELF REPORT CHECKLIST:

Past Health Problems:

[ ] Stroke
[ ] Traumatic Brain Injury
[ ] Concussion
[ ] Brain Tumor
[ ] Amyotrophic Lateral
   Sclerosis
[ ] Cerebral Palsy
[ ] Multiple Sclerosis
[ ] Parkinson's Disease
[ ] Peripheral Nerve
   Injuries
[ ] Spina Bifida
[ ] Spinal Cord Injuries
[ ] Loss of Consciousness
[ ] Bleeding Disorders

[ ] Migraine/Frequent
   Headaches
[ ] Seizures or Epilepsy
[ ] Chronic Joint Pain
[ ] Chronic Muscle Pain
[ ] Back Injuries
[ ] Low Back Pain
[ ] Swollen/Stiff Joints
[ ] Bone Disease
[ ] Osteoarthritis
[ ] Rheumatoid Arthritis
[ ] Repetitive Strain
   Injury
[ ] Fibromyalgia
[ ] Heart Attack

[ ] Heart Murmur
[ ] High/Low Blood
   Pressure
[ ] High Cholesterol
[ ] Congenital Heart
   Disease
[ ] Disease of the Arteries
[ ] Rheumatic Fever
[ ] Emphysema,
   Pneumonia, Asthma,
   Bronchitis
[ ] Diabetes
[ ] Ulcers
[ ] Kidney or Liver
   Disease

Present Health:

List current problems:

1.

2.

3.

4.

List medications taken now or in last 3 months:

1.

2.

3.

4.

List Symptoms:

[ ] Fatigue
[ ] Numbness/tingling of arms/legs/face
[ ] Loss of / trouble understanding speech
[ ] Loss of / double vision
[ ] Dizziness
[ ] Loss of coordination/balance
[ ] Severe/unusual headache
[ ] Memory problems
[ ] Vertigo

[ ] Shortness of breath
[ ] Joint/muscle pain
[ ] Back pain/injury
[ ] Leg pain/injury
[ ] Irregular heart beat
[ ] Chest pain/pressure
[ ] Persistent cough
[ ] Wheezing

Appendix II – Consent form

Title of Study:
Assessment of Dynamic Balance and Fall Risk in Sitting

Principal Investigator:
Dr. Albert Vette

Co-Investigators:
Dr. Hossein Rouhani
Kshitij Agarwal
Alireza Noamani

Why am I being asked to take part in this research study?

You are being invited to take part in a research study. Before you make a decision, one of the researchers will go over this form with you. You are encouraged to ask questions if you feel anything needs to be made clearer. You will be given a copy of this form for your records.

Seated balance problems are common in many clinical populations using wheelchairs. Neuromuscular impairments such as stroke, spinal cord injury, or traumatic brain injury, but also aging may lead to difficulties in controlling seated balance. As a result, these individuals have an increased risk of falling and may struggle with essential activities of daily living. Even in the absence of actual falling, fear of falling limits their activity and poor posture may lead to secondary health complications.

The first step towards our goal of understanding seated balance mechanisms is to gather data from healthy subjects in conditions that challenge their seated balance. You are being asked to participate in this study as part of a healthy control group. The control strategy that you use to maintain your balance will help understand how people maintain and lose balance during sitting.

157

What is the reason for doing the study?

We would like to identify, mathematically, the control system used by the human body to prevent falls. This will be done by measuring the body's response to balance challenges. At the same time, we will search for indicators of fall risk and test the accuracy of wearable technologies in measuring these fall risk indicators.

What will I be asked to do?

You will be asked to take part in one session of experimental data collection lasting 2-3 hours. You will receive a cash reimbursement for parking at the rate of $10.00 per hour for three hours, for a total value of $30.00. You will be asked to bring minimalistic, tightly fitted clothing to wear during the experiment. You will also be asked to remove your shoes. A change room will be provided.

The first hour will be used to prepare the various types of data collection. You will be fitted with over-skin electromyography electrodes that measure the muscle activity levels. The electrodes will be placed on specific body locations (back, abdomen, and thighs) after the skin has been shaved and cleaned using alcohol wipes. We will then place small reflective markers on your body (hips and back) to record their motion using cameras. Motion sensors boxes (similar to the ones inside the smart phone or watch) will be placed on your upper and lower back to measure their motion. These markers and sensors boxes will be fixed to your clothes or skin using non-allergenic medically approved tape. As part of the experimental set-up, you will be asked to perform a series of exercises that elicit maximum strength of the muscles to be measured via electrodes. An example of these exercises is a resisted abdomen crunch.

After set-up, you will be seated on a custom-made sitting apparatus fixed to the CAREN system. The sitting apparatus is equipped with an adjustable backrest and no arm rests. The CAREN system is a piece of rehabilitation technology housed within the Glenrose Rehabilitation Hospital. CAREN is an acronym for "Computer-Assisted Rehabilitation Environment." The system includes virtual reality, a robotic platform, and motion capture capability. It is currently used for clinical treatment of patients with mobility and balance problems.

First, you will be asked to maintain a natural seated posture while the CAREN cameras record your motion. Second, you will be asked to test your voluntary limits of seated balance by leaning as far as you can in eight directions. Third, the robotic platform will apply safe motions to challenge your seated balance (The seat will be moved around similar to riding on a bus or train on the public transportation system). Fourth, the the large screen in front of your eyes will show moving images to challenge your seated balance (similar to watching a film on a large theater screen). Finally, a combination of platform and screen will together challenge your seated balance. The challenges applied by of the platform and screen will remain within the limits of those used in clinical practice. You will be allowed to take breaks or even withdraw from the measurements at any time.

158

What are the risks and discomforts?

Participants may feel generally tired from the testing session.

Some participants may experience dizziness and/or disorientation during trials because of the motion on the platform and screen. Although it is not likely for healthy participants, there is a risk of falling when being perturbed or when the visual environment is altered. Therefore, participants will always wear a safety harness to completely prevent falls. In addition, participants will always be closely watched by an experimenter.

Some participants may feel anxious about leaning to their personal limits of falling. Note that you will be given ample practice time to get familiar with the task. Again, all participants will wear a safety harness to prevent falls on the testing systems that eliminates the risk of falling. In addition, participants will always be closely watched by an experimenter.

It is not possible to know all of the risks that may be present during a study. However, the researchers have taken all reasonable safeguards to minimize any known risks to a study participant.

What are the benefits to me?

You may benefit by learning about experimental procedures and new technology used in gait and posture research and treatment. However, you may not directly benefit from being in this research study. This study may help to better assess and treat people with balance problems in the future.

Do I have to take part in the study?

Being in this study is your choice. If you decide to be in the study, you can change your mind and stop being in the study at any time. This decision will in no way affect your relationship to the University of Alberta or the Glenrose Rehabilitation Hospital.

We will ask you to complete a medical history form. Please note that you do not have to answer any questions that you are not comfortable with.

In case you decide to withdraw your participation, experimental testing will stop immediately. Note that the data recorded up to that point will be discarded and not used in subsequent analyses.

Data can be withdrawn from the study as long as obtained results have not been published.

Will my information be kept private?

During the study, we will be collecting data about you. We will do everything we can to make sure that this data is kept private. No data obtained in this study, including your name, will be released outside of the researcher's office or published by the researchers. Sometimes, by

law, we may have to release your information with your name; as such, we cannot guarantee absolute privacy. However, we will make every legal effort to make sure that your information is kept private.

After the study is completed, we will still need to securely store your data that was collected as part of the study. At the University of Alberta, we keep data stored for a minimum of 5 years after the end of the study.

What if I have questions?

If you have any questions about the research now or later, please contact Dr. Albert Vette at 780-492-1534 or by email at albert.vette@ualberta.ca. You can also contact Dr. Hossein Rouhani at 780-492-8344 or by email at hrouhani@ualberta.ca.

If you have any questions regarding your rights as a research participant, you may contact the Health Research Ethics Board at 780-492-2615. This office has no affiliation with the study investigators.

There are no conflicts of interest associated with this study.

CONSENT

Title of Study: Assessment of Dynamic Balance and Fall Risk in Sitting

Principal Investigator: Albert Vette, Ph.D.   **Phone Number:** 780-492-1534
Co-Investigator: Hossein Rouhani, Ph.D.   780-492-8344

	Yes	No
Do you understand that you have been asked to be in a research study?	☐	☐
Have you read and received a copy of the attached Information Sheet?	☐	☐
Do you understand the benefits and risks involved in taking part in this research study?	☐	☐
Have you had an opportunity to ask questions and discuss this study?	☐	☐
Do you understand that you are free to leave the study at any time, without having to give a reason and without affecting your relationship with the University of Alberta and the Glenrose Rehabilitation Hospital	☐	☐
Has the issue of confidentiality been explained to you?	☐	☐
Do you understand who will have access to your study records, including personally identifiable information?	☐	☐

Who explained this study to you? _____

I agree to take part in this study:

     Signature of Research Participant _____

             (Printed Name) _____

                    Date_____

Signature of Researcher Obtaining Consent_____

             (Printed Name) _____

                    Date_____

Appendix III – Force plate characterization

The accuracy in the force plate center of pressure (COP) measurements and the force measurements in perpendicular direction were assessed before the study. A self-made grid was placed on top of the force plate with the grid size of 1 cm × 1 cm. Each intersections of the grid was pushed with a manual force of more than 100 N and computed the COP from the force plate measurements as shown in Table III-1. Discrete weights in the range of 4 to 132 kg were placed on top of the force plate and measured the weight from the force plate as shown in Table III.2. The mean error (standard deviation, SD) in x- and y-direction component of the COP was 0.23 (0.11) and 0.12 (0.08) cm, respectively. The mean perpendicular force (SD) as a percentage of applied load was 1.31 (1.19) %.

Table III-1. Accuracy of center of pressure measured from the force plate.

Actual x (cm)	Actual y (cm)	Measured x (cm)	Measured y (cm)	Error x (cm)	Error y (cm)
4	4	4.34	4.05	0.34	0.05
8	8	8.28	8.21	0.28	0.21
12	12	12.15	12.25	0.15	0.25
16	16	16.05	16.05	0.05	0.05
20	20	19.73	19.97	0.27	0.03
-4	-4	-3.72	-4.12	0.28	0.12
-8	-8	-7.80	-8.25	0.20	0.25
-12	-12	-11.75	-12.16	0.25	0.16
-16	-16	-15.60	-16.08	0.40	0.08
-20	-20	-19.51	-19.94	0.49	0.06
4	-4	4.22	-4.02	0.22	0.02
8	-8	8.30	-8.16	0.30	0.16
12	-12	12.21	-12.10	0.21	0.10
16	-16	16.17	-15.85	0.17	0.15
20	-20	19.98	-19.88	0.02	0.12
-4	4	-3.74	3.99	0.26	0.01
-8	8	-7.82	7.98	0.18	0.02
-12	12	-11.87	11.90	0.13	0.10
-16	16	-15.71	15.85	0.29	0.15
-20	20	-19.76	19.72	0.24	0.28

Table III-2. Accuracy of the perpendicular direction force measured from the force plate.

Actual weight (kg)	Actual weight (N)	Measured weight (N)	Error (N)	Error %
4.9	48.07	46.10	1.97	4.10
10.1	99.08	99.19	0.11	0.11
15.0	147.15	145.98	1.17	0.79
10.1	99.08	99.20	0.12	0.12
20.2	198.16	198.42	0.26	0.13
22.7	222.69	225.25	2.57	1.15
23.5	230.54	234.41	3.88	1.68
65.4	641.57	652.68	11.11	1.73
70.1	687.68	699.17	11.49	1.67
131.8	1292.96	1314.00	21.04	1.63

Appendix IV – Identifying the inertial parameters of the customized force plate in the anterior-posterior direction

Force plate under motion causes erroneous measurements of the forces and moments. It is desirable to remove the inertial components from the force plate measurements. Force plate can be considered to be a rigid body and Newton laws of motion are applicable to it. Consider a case where the force plate is accelerated in the positive y-direction. This causes a pseudo-force (F_y) acting at the center of mass (COM) of customized force plate in negative y-direction as shown in Figure IV-1. In addition, the pseudo-force produce a moment (τ_x) in the negative x direction with the axis of rotation at force plate geometric center. As a result of acceleration of the customized force plate, the pseudo-force and the moment measured by the sensors of the force plate in the anterior-posterior (A-P) direction and medio-lateral (M-L) direction, respectively can be described by the Equations (93-94), where $mass$ is the mass of the force plate and stool; and d is the distance between force plate geometric center and COM.

$$F_y = mass * acceleration \qquad \text{Eq. (93)}$$

$$\tau_x = F_y * d \qquad \text{Eq. (94)}$$
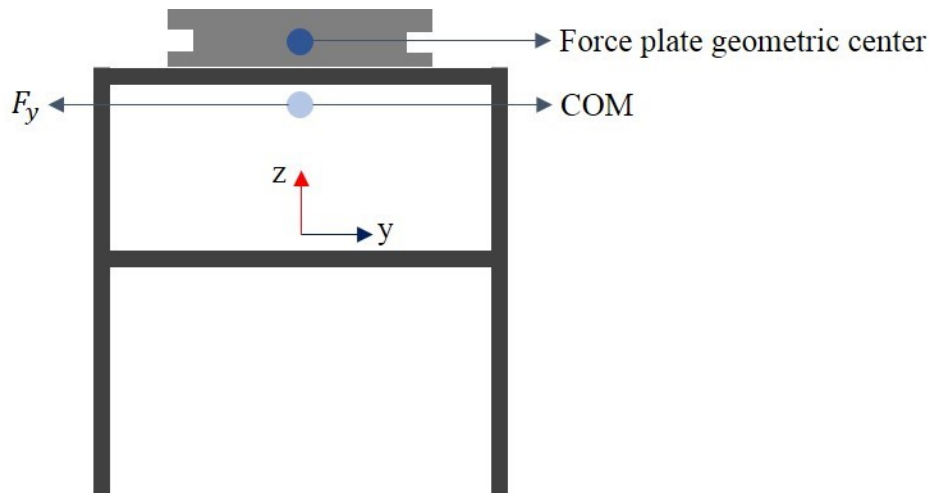
Figure IV-1. Force plate setup with its center of mass (COM) location. F_y is the pseudo force acting at the COM of force plate and stool.

The force plate was placed on the Computer-Assisted Rehabilitation Environment (CAREN) platform as shown in Figure 4-11A. The A-P perturbations were applied to the customized force plate similar to those applied in our study on human participants. The force plate had no weight on top of it. The forces and moments readings were measured from the force plate. The acceleration of the force plate was calculated from the motion capture markers placed on top of the force plate. Three trials of 240 s each were conducted, with independent perturbation signals according to the procedure mentioned by Preuss et al. (2004).

The external perturbation's frequency content was in the range of 0.1 to 5 Hz (designed by us) and considering the force plate to be an LTI system, similar frequencies were expected to be present in the force plate data. The force plate data was filtered by an 8th order Butterworth filter with a cut-off frequency of 10 Hz. A 1st order Autoregressive Exogenous (ARX) model is implemented to fit the data. The model implements least square estimation to calculate the polynomials A and B. The transfer function for ARX model is shown in Equation (95).

$$Ay_t = Bx_t + e_t$$

Eq. (95)

For calculating the mass of the customized force plate as mentioned in Equation (93), the input (x_t) was considered to be the acceleration of the force plate and output (y_t) was the y-direction component of the force measured from the force plate. For calculating the moment arm (d) as mentioned in Equation (94), input (x_t) was considered to be the acceleration of the force plate and output (y_t) was the x-direction component of the moment measured from the force plate. B was considered to be a first order polynomial and A was considered to be a zeroth order polynomial for both mass and moment arm calculations. The first two trial data were utilized to estimate the values of the variables, while the third trial was used to validate the values.

Table IV-1 presents the inertial parameters values obtained from the experiment. The value of mass of the customized force plate was predicted to be 49.77 Kg and the moment arm was predicted to be 0.12 m. The model fitting percentages for calculation of mass and moment arm were 95.9 % and 88.9 %, respectively.

The high model fitting percentages suggest a good fit of the ARX model on the data. This also supports that ARX model could be used to predict the pseudo-force and moment from the

acceleration of the force plate. Therefore, enabling the removal of inertial components from the force plate under motion.

Table IV-1. Inertial parameters of the customized FP.

Parameter	Value	Model Fitting Percentage
Mass (m)	49.77 ± 0.10 Kg	95.92 %
Moment arm (d)	0.12 ± 0.01 m	88.90 %